POLITECNICO
MILANO 1863

SCUOLA DI INGEGNERIA INDUSTRIALE
E DELL'INFORMAZIONE

Numerical simulation of in-flight icing effect on aerodynamic characteristics of airfoils

TESI DI LAUREA MAGISTRALE IN
AERONAUTICAL ENGINEERING - INGEGNERIA AERONAUTICA

Author:	**Chen Liu**
Student ID:	**10726559**
Advisor:	**Prof. Federico Piscaglia**
Co-advisor:	**Prof. Akira Rinoshika**
Academic year:	**2021 - 2022**

Department of Aerospace Science and Technology

Politecnico di Milano

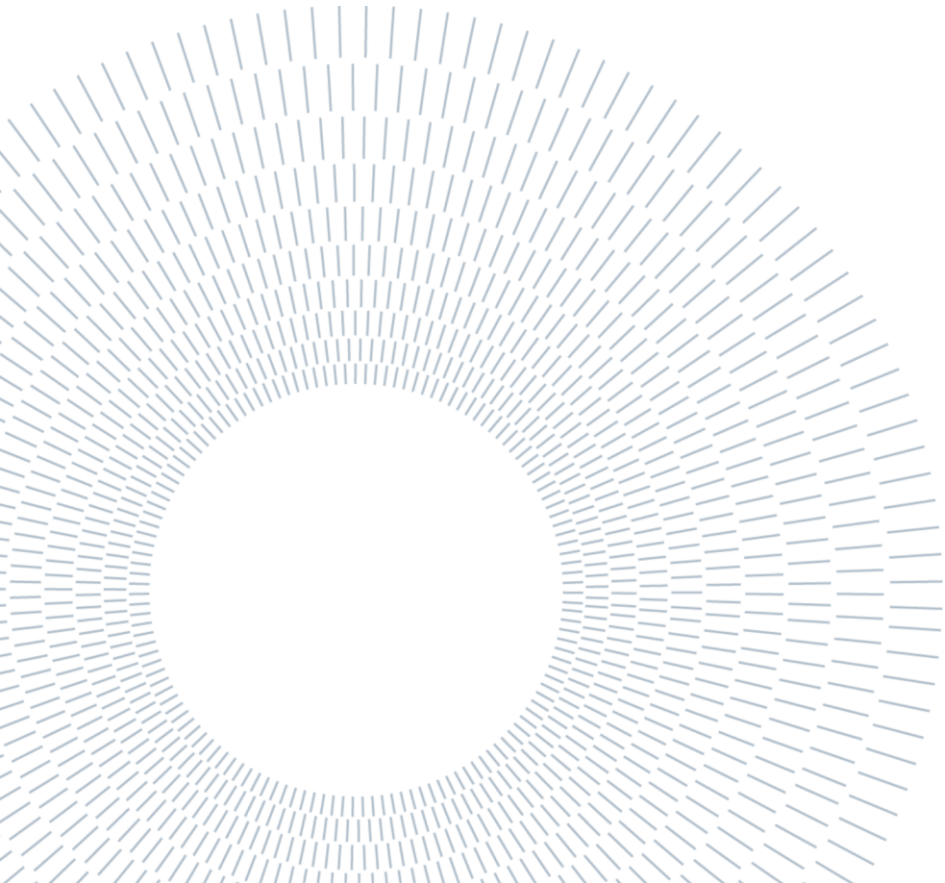

Abstract

During the flight of aircraft, due to special weather and flight conditions, ice accretion is prone to occur. This problem is a major hidden danger affecting flight safety, and it is easy to cause serious accidents. Therefore, the problem of ice accretion is a hot issue for researchers.

The main work of this paper includes: the research background of icing problem were discussed, the theories and numerical methods related to airfoil icing process were introduced; afterwards, ANSYS icing platform was built to solve the airfoil icing, and under specific conditions, the numerical results were compared with reference data to make validation; under different tests conditions, the ice shapes, surface pressure coefficients, lift and drag coefficients, etc. were analyzed to judge aerodynamic losses.

Numerical results showed that freestream temperature mainly affects ice shape, and higher temperature is easy to produce clear ice; clouds liquid water concentration and flight speed mainly affect icing rate, the higher the water concentration, the faster the flight speed, the faster the icing rate, and the more serious the lift loss and drag growth. Median volume diameter of droplets significantly affects airfoil icing range, the larger the median volume diameter, the larger the icing range. The icing at a small angle of attack has little effect on the airfoils aerodynamic characteristics, instead the icing airfoils at a large angle of attack is prone to stall, resulting in a sharp drop in lift and a huge increase in drag.

Key words: airfoil icing, CFD, ANSYS simulation, aerodynamic characteristics, in-flight icing effect.

Abstract in lingua italiana

Durante il volo dell'aereo, a causa di particolari condizioni meteorologiche e di volo, è probabile che si verifichi l'accumulo di ghiaccio. Questo problema è un grave pericolo nascosto che incide sulla sicurezza del volo ed è facile causare gravi incidenti. Pertanto, il problema dell'accrescimento del ghiaccio è una questione calda per i ricercatori.

Il lavoro principale di questo documento include: sono stati discussi i retroscena della ricerca sul problema della formazione di ghiaccio, sono state introdotte le teorie ei metodi numerici relativi al processo di formazione di ghiaccio sui profili aerodinamici; successivamente, è stata costruita la piattaforma di glassa ANSYS per risolvere la formazione di ghiaccio sul profilo alare e, in condizioni specifiche, i risultati numerici sono stati confrontati con i dati di riferimento per effettuare la convalida; in diverse condizioni di prova, sono state analizzate le forme del ghiaccio, i coefficienti di pressione superficiale, i coefficienti di portanza e resistenza, ecc. per giudicare le perdite aerodinamiche.

I risultati numerici hanno mostrato che la temperatura del flusso libero influisce principalmente sulla forma del ghiaccio e che una temperatura più elevata è facile da produrre ghiaccio trasparente; la concentrazione di acqua liquida delle nuvole e la velocità di volo influiscono principalmente sulla velocità di formazione di ghiaccio, maggiore è la concentrazione di acqua, maggiore è la velocità di volo, maggiore è la velocità di formazione di ghiaccio e più grave è la perdita di portanza e la crescita della resistenza. Il diametro del volume medio delle goccioline influisce in modo significativo sull'intervallo di glassa del profilo aerodinamico, maggiore è il diametro del volume mediano, maggiore è l'intervallo di glassa. La glassa con un piccolo angolo di attacco ha scarso effetto sulle caratteristiche aerodinamiche dei profili alari, invece i profili alari con ghiaccio con un ampio angolo di attacco tendono allo stallo, con conseguente forte calo della portanza e un enorme aumento della resistenza.

Parole chiave: glassa di profili alari, CFD, Simulazione ANSYS, caratteristiche aerodinamiche, effetto glassa in volo.

Contents

List of Figures

List of Tables

List of Symbols

English character

a_{ij}	Anisotropy term for Reynolds stress	$[N/m^2]$
A_w	Water drop projected area	$[m^2]$
c	Airfoil chord	$[m]$
C	Cost function	
C_D	Drag coefficient	
C_L	Lift coefficient	
Cp	Constant pressure specific heat; Airfoil pressure coefficient	$[J/(kg \cdot K)]$; []
C_v	Constant volume specific heat	$[J/(kg \cdot K)]$
d	Water droplet equivalent diameter	$[m]$
ds	Unit spread area on the airfoil	$[m^2]$
dS	The unit area of the control body	$[m^2]$
dy_0	The unit extension area through which the incoming water droplets pass	$[m^2]$
$\vec{d}$,$\vec{r}$	Distance vector between two points	$[m]$
e	Internal energy per unit mass	$[J/kg]$
e_f	The enthalpy of a unit mass of water film	$[J/kg]$
E	Total droplet collection efficiency	
E_f	Enthalpy value of water membrane system per unit area	$[J/m^2]$
E^t	Total energy per unit volume	$[J/m^3]$
F_f	Mass flux at boundary surface f	$[kg/s]$

$\overrightarrow{F_b}$	Air buoyancy on water droplets	$[N]$
$\overrightarrow{F_d}$	Air resistance to water droplets	$[N]$
$\overrightarrow{F_g}$	Water droplet gravity	$[N]$
$\vec{F}, \vec{G}$	Generalized Flux Vectors	
$\vec{g}$	Gravitational acceleration	$[m/s^2]$
h_c	Convective heat transfer coefficient	$[W/(m^2 \cdot K)]$
h_f	Water film height	$[m]$
H	Forward projected height of the airfoil	$[m]$
k	Thermal conductivity; turbulent kinetic energy	$[W/(m^2 \cdot K)]$; $[m^2/s^2]$
k_s	Wall roughness	$[m]$
K	Stiffness matrix	
LWC	Liquid water concentration	$[g/m^3]$
m	Mass	$[kg]$
$\dot{m}$	Mass Flow	$[kg/s]$
Ma	Mach number	
MVD	Median volume diameter	$[m]$
$\vec{n}$	Normal at the airfoil or control body interface	
N_{tot}	Total number of control bodies	
p	Pressure	$[Pa]$
Pr	Prandtl number	
$\dot{Q}$	Heat flow	$[W/m^2]$
Q^{ϕ}	Generalized source/sink terms	
R	Air gas constant	$[J/(kg \cdot K)]$
Re	Reynolds number	
S_u, S_l	The impact limit of water droplets on the upper and lower airfoils	$[m]$
S_μ	Sutherland constant	
$\vec{S}$	Area vector	$[m2]$

t	Time	$[s]$
T	Temperature in Kelvin	$[K]$
T_0	Reference temperature	$[K]$
$\tilde{T}$	Temperature in Celsius	[°C]
u	The velocity component in the x direction	$[m/s]$
U	Speed size	$[m/s]$
U_{wn}	The normal velocity of the water droplet hitting the surface	$[m/s]$
v	The velocity component in the y direction	$[m/s]$
$\vec{v}$	Velocity vector	$[m/s]$
$\overrightarrow{v_{ws}}$	Velocity vector of water droplets hitting the surface	$[m/s]$
V	Control volume	$[m3]$
∂V	Control body interface	
W_i	Weight factor	
x, y	Positions in Cartesian coordinates	$[m]$

Greek character

ρ	Density	$[kg/m^3]$
τ	Shear stress	$[N/m^2]$
$\overrightarrow{\Psi}$	Vector of conserved variables	
λ	Second viscosity coefficient	$[Pa \cdot s]$
Γ^{ϕ}	Generalized Diffusion Coefficients	
φ	Gradient limiter, trial function	
δ_{ij}	Kronecker function	
ν	Kinematic viscosity coefficient	$[m^2/s]$
ν_t	Turbulent viscosity coefficient	$[m^2/s]$

ν_e	Effective viscosity coefficient	$[m^2/s]$
ω	Turbulence frequency	$[s^{-1}]$
μ	Dynamic viscosity coefficient	$[Pa \cdot s]$
γ	Specific heat ratio	
μ_0	Reference viscosity coefficient	$[Pa \cdot s]$
ϕ	General physical quantity	
ε	Turbulent kinetic energy dissipation rate	$[m^2/s^3]$
β	Local droplet collection efficiency	
α	Flight angle of attack, volume fraction	
α_w	Water droplet volume fraction	
ψ	Basis function	
$\vec{\Gamma}$	Generalized Flux of Water Droplet Flow Field	
τ_w	Wall shear force	$[N/m^2]$

Subscript

$base$	Benchmark
es	Evaporation and Sublimation
eva	Evaporation
f	Control body boundary surface, water film
fus	Fusion
i	*i-th* control volume, equation, calculation node
ice	Ice
imp	Collision with airfoil

L	Latent heat
min	Minimum
mix	Mixture
N	Center point of adjacent control body
P	Main control body center point
r	Heat radiation
s	Airfoil icing surface
$subl$	Sublimation
w	Water droplets
x	x Directional component
y	y Directional component
∞	Freestream flow

Chapter 1 Introduction

1.1 Research Background

1.1.1 Overview of Aircraft Ice Accumulation and Related Physical Mechanisms

When an aircraft flies in clouds containing supercooled water droplets, or encounters rain such as freezing rain, ice accretion may occur on some key parts of the airframe, such as: aircraft wings, helicopter rotors, control surfaces, and engines Intake port, pitot tube, etc. Ice accumulation at these parts will have a serious or even devastating impact on the flight performance and flight safety of the aircraft. For this reason, aviation researchers in many countries in the world have always paid close attention to the problem of aircraft icing, and have launched a wide variety of ice accretion studies.

In fact, the problem of icing has plagued aeronautical engineers since the early stages of flight in the last century. In order to judge the icing strength, in the 1940s and 1950s, the US Weather Bureau and the US Air Force developed and used the icing strength scale comparison table, in which the liquid water concentration (LWC) of the cloud was regarded as an important parameter index to determine the intensity of ice accretion[1]; in addition, before and after World War II, National Advisory Committee for Aeronautics (NACA) (now replaced by NASA) embarked on some icing research projects, in order to develop thermal anti-icing systems for military aircraft; and an icing research wind tunnel was designed by Lewis Rodert et al., which was the predecessor of the current NASA Glenn IRT icing wind tunnel. Before the 1960s, while the experimental technology was relatively backward, some important experiments and flight test projects were completed one after another, laying a solid foundation for alleviating the negative impact of aircraft icing and designing anti-icing systems[2]; During this period, some scientists also developed basic theories related to ice accretion, for example, Langmuir and Blodgett et al.[3] analyzed the trajectory of water droplets in clouds in 1946, and Messinger[4] proposed the classical ice accretion model in 1953. Although these early works were key milestones in the study of ice accretion theory, the theoretical results obtained were only used to solve ice accretion problems on simple geometric surfaces, such as plates or cylinders, due to the limitations of the computational resource at that time. Until the advent of the computer age in the late 1970s, computing power developed rapidly, and researchers gradually focused on theoretical and numerical studies of ice with complex geometric surface areas, such as airfoils.

With the continuous development of related research, people have a more in-depth understanding of the ice accretion problems encountered by aircraft during flight. Generally speaking, aircraft icing is thought to be the phenomenon that occurs when supercooled water droplets hit and freeze on unprotected surfaces when the aircraft is flying in clouds with temperature below or equal to freezing. The rate and amount of ice accretion on an aircraft depends on the following factors: icing surface configuration, aircraft flight conditions and surrounding weather environment. Among them, the icing surface configuration includes: surface size (such as airfoil chord length) and geometry (such as the selection of different airfoils); aircraft flight conditions include: flight speed V_∞ and flight angle of attack α; ambient weather environment include: ambient temperature T_∞, cloud cover area(related to icing time), cloud liquid water concentration (LWC), and water droplet size, etc. When the above parameters are changed, the ice type on the surface where the ice accretion occurs will also change. To date, ice types formed on aircraft wings or helicopter rotor blades have been classified into the following categories[5]:

1） Rime ice

Rime ice is a kind of white, opaque ice accretion, which has a relatively streamlined shape, but in general the roughness is significantly greater than that of the airfoil it is attached to. It is often formed when the flight airspeed, the ambient temperature and the liquid water concentration are under lower conditions, as shown in Figure 1.1(a);

2） Clear ice

Clear ice, also known as "glaze ice", is a transparent and smooth ice type. This ice type has a local shape like a “corner”, since clear ice generally forms at higher airspeeds, warmer temperatures (above -10 °C), and higher liquid water concentration, not all of the water droplets that collide with the leading edge of the airfoil can be frozen on the impacting surface in time, and some water droplets that have not been frozen will continue to move along the impacting surface, and will be gradually frozen during the motion. Therefore, this "corner" ice pattern appears on the upper and lower surfaces of the wing, as shown in Figure 1.1(b);

3） Mixed ice

Mixed ice is the third ice type between rime ice and clear ice. It is often formed under the conditions of intermediate temperature and the coexistence of large and small water droplets in the cloud. The surface is relatively rough and the ice color is whitish. Once formed, it is firmly attached to the airfoil, as shown in Figure 1.1(c);

4） Beak ice

As flight speed or ambient temperature continues to increase, a kind of ice that is shaped

like a bird's beak will appear on the airfoil upper surface, as shown in Figure 1.1(d).

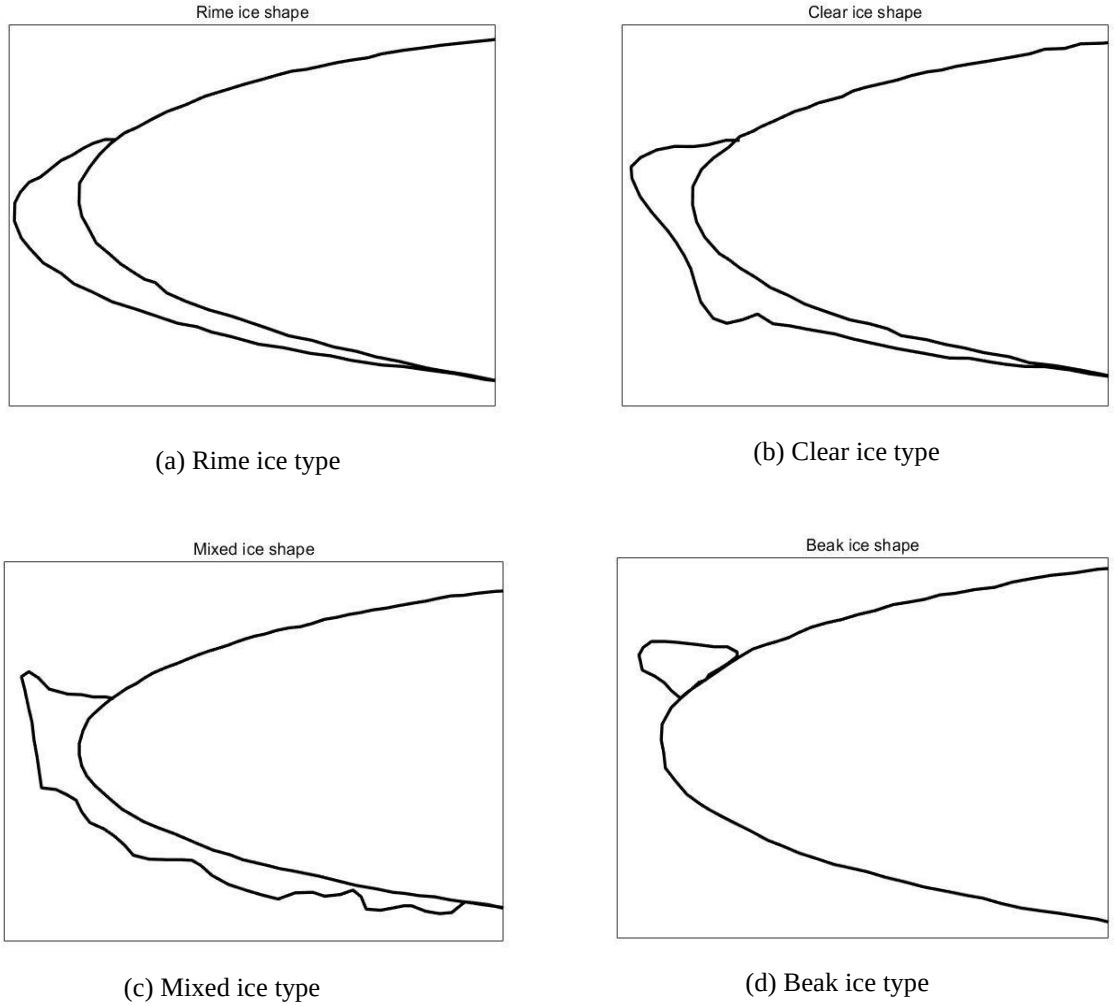

(a) Rime ice type

(b) Clear ice type

(c) Mixed ice type

(d) Beak ice type

Figure 1.1 Main ice types of wing icing surface

The physical mechanism behind the formation of the above-mentioned main ice types includes two main parts: 1) liquid water droplets hit the airfoil and are intercepted; 2) the intercepted water droplets freeze to make ice accretion. For the first part, the rate at which water droplets are intercepted by the airfoil per unit time can be viewed as the product of the local droplet collection efficiency β, the cloud liquid water concentration(LWC), and the speed of the aircraft passing through the cloud. Among them, the water droplet collection efficiency β of the airfoil is mainly controlled by the size and shape of the airfoil, as well as the median volume diameter (MVD) of the water droplets; in addition, the liquid water concentration and flight speed also play an important role in the interception rate. For the second part, the rate at which the droplets freeze is primarily controlled by the heat transfer from the airfoil. The heat transfer includes the energy conversion of the kinetic energy and thermal energy of the water droplet itself, aerodynamic heating, convective cooling,

evaporative cooling, and the release of freezing latent heat, etc. When an aircraft passes through a cloud layer containing supercooled water droplets, the water droplets hitting the airfoil will try to release their latent heat to freeze to form ice. By controlling the mass and energy conservation condition, the freezing amount of water droplets on the surface can be determined. Generally speaking, if the water droplets can be completely frozen at the impacting position, rime ice with better streamlines will be formed; if the water droplets are not completely frozen, some of the water that remains liquid will continue to flow along the impinging surface, then gradually freeze to form the other ice types mentioned above.

1.1.2 The Harm and Research Significance of Aircraft Ice Accretion

When the icing phenomenon of the aircraft occurs, the pilot needs to take effective measures in time to remove the ice on the aircraft to ensure flight safety, otherwise it will easily lead to fatal consequences. According to the National Transportation Safety Board (NTSB) report on the investigation of aircraft accidents from 2000 to 2011[6], the number of accidents related to weather factors accounted for 29% of the total number of accidents, which is equivalent to 435 out of 1500 accidents on average; among the accidents caused by bad weather, the accidents caused by the icing of the airframe structure and the carburetor accounted for 9%. In addition, NTSB also investigated the icing accidents in America from 2010 to 2014, with 52 icing accidents and a total of 78 fatalities. The above-mentioned investigations fully demonstrate that aircraft icing is an important cause of aircraft crashes and must be paid enough attention to.

Ice accretion on the airframe can form during different flight phases, including take-off and climb, cruise, descent, approach and landing. When the icing on the ground occurs, it will not only increase the weight of the aircraft, but also reduce the lift and increase the drag, which will prolong the distance and time required for take-off, and even make the aircraft fail to take off normally. Compared with the rest of the flight envelope, the stall margin of the aircraft during the takeoff phase is usually the smallest. If the ice accretion on the ground is not removed in time, the stall margin will be offset by the aerodynamic losses caused by icing, put the aircraft at risk of stalling. Relevant studies have shown that frost of about 2 mm can cause the lift coefficient of the aircraft to drop by about 15% and the stall speed to increase by about 20%. When the icing during flight occurs, On the one hand, due to the deterioration of aerodynamic characteristics, the required thrust of the aircraft increases, and the fuel consumption increases; on the other hand, due to the deterioration of the handling characteristics, the control efficiency, the maximum lift coefficient and the stall angle of attack of the aircraft are significantly reduced, which make it prone to stall and crash.

Ice accretion on the aircraft can form on different parts, including wing and rotor

surfaces, rudders, elevators, engine intakes and compressor blades, sensors, etc. When ice accretion occurs on the surface of the wing or the rotor, or other key aerodynamic surfaces, it will change the geometries of spanwise airfoil sections, no matter in the initial stage of ice accretion or in the process of ice accretion, resulting in a loss of lift, a reduction in the stall angle of attack, and an increase in parasitic drag. Lynch and Khodadoust et al.[7] had discussed in detail the results of icing wind tunnel tests for different NACA airfoils, under different Reynolds number conditions, different flight conditions and atmospheric conditions, and analyzed the effects of different types of icing on the aircraft lifting surfaces. Under specific experimental conditions, wind tunnel testing results of different airfoils show that even about 2-3 mils of ice accretion can lead to a significant reduction in the maximum lift capacity and stall angle of attack: for some airfoils, the maximum lift reduction of a single-component lifting surface (i.e., without slats, flaps and other aerodynamic components) may be as high as 40%; for airfoils with common thickness ratios(9%-15%), the stall angle of attack can be reduced by about 6°; in addition, for some airfoils with thickness ratios below 15%, drag increases under low-speed flight conditions range from slightly more than 50% to about 120%.

Ice accretion not only causes the deterioration of the aerodynamic performance of the lifting surface, but also changes the weight distribution on the aircraft, reduces the static stability margin, and damages the stability of the aircraft. When ice accretion occurs on the tail, the control efficiency will be affected, and even worse, the movable surface will be blocked, which causes the controllability of the aircraft fails completely.

When ice accumulates on the engine intake, the direction and flow rate of the air flowing into the intake will change; if ice forms on the compressor blades, the blades will suffer from unsteady aerodynamic and structural loads, which can make vibration and fatigue damage, so that the life of the engine and propulsion efficiency will be severely affected; not only that, the ice accretion on the rotating blades may cause dangerous ice shedding behavior, which will eventually cause serious mechanical damage to the engine.

When ice accretion occurs on pitot tubes or other sensors, inaccurate airspeed indication, pressure, power and other data are likely to be generated, which may lead to misjudgment and improper operation by pilots. The most typical relevant case is the crash of Air France Flight 447 in 2009, which killed 228 people, and it was considered the worst air disaster since Air France was founded. Although the pilot of the aircraft at that time, Pierre Cedric Bonin, always kept the wrong operation of the lever, which made the angle of attack of the aircraft was too large and the aircraft was in a stall state, which eventually led to an air accident, the initial reason was that the

pitot tube was icing and failed to detect the flight speed of the aircraft, causing the autopilot mode to be turned off, and the pilot had to manually control the aircraft, which led to the improper operation of the pilot. It can be seen that the accumulation of ice in any part of the aircraft may bring disaster.

To sum up, aircraft icing directly affects the flight safety of the aircraft and the life safety of passengers, and is one of the major hidden dangers that requires people to be vigilant. In order to ensure that passengers can take the plane safely in most weather conditions, improve the power and control efficiency of the aircraft, and reduce the operation and maintenance costs, relevant researchers need to accurately predict ice accretion and assess its associated performance losses when designing the aircraft including the anti-icing system.

For this reason, it is necessary to carry out corresponding analysis and research work on the airfoil icing problem during flight to provide support for the design of the anti-icing system, so as to better meet the safety and economic requirements of aircraft design.

1.1.3 Common Anti-icing Systems

After understanding the physical mechanism, formation location and possible impact of ice accretion, the design of the anti-icing system becomes a necessary part of the aircraft design process. According to the development and application history, the anti-icing system can be divided into two categories: traditional form and new form[8]. Traditional form includes: mechanical de-icing, liquid de-icing, thermal de-icing; new form includes: memory metal de-icing, electromagnetic repulsion de-icing, low-frequency piezoelectric de-icing, etc. Although the new form of anti-icing system continues to be experimentally researched, due to its insufficient technological maturity, most anti-icing systems used on contemporary aircrafts are in previous traditional form, among which, the hot gas method and the electrothermal method under the form of thermal de-icing have been theoretically analyzed. The following is only a brief introduction to the traditional form of anti-icing system:

1） Mechanical de-icing form. Mechanical de-icing is to take mechanical means to break the ice, and then use airflow or vibration to remove the ice. Mechanical de-icing includes: deicing boot, electric pulse de-icing, etc. Deicing boot can be said to be one of the earliest forms on the aircraft, invented around the 1930s. They are generally installed at the leading edge of the wing or tail where ice is likely to accumulate, and are composed of many thick rubber films. When the ice accretion forms on the aerodynamic surfaces, the pneumatic system will deliver compressed air to inflate the deicing boot, make it expand and break the ice accretion, and then the air flow will blow away the broken ice; afterwards the deicing boot will be deflated to restore the geometric shape of the surfaces. Besides, the air bag installed on the surfaces is controlled by bleed air to make it periodically vibrate with small amplitude and

high frequency, which can also achieve the purpose of deicing. This kind of form is lighter in weight and lower in energy consumption, and can be used on small, low-speed aircraft; however, it may not be sufficient to handle more severe icing conditions, and it may change the aerodynamic shape of the airfoil during de-icing process, so it is rarely used on the high-speed aircraft.

Electric pulse de-icing consists of power supply device, capacitor, thyristor, induction coil, etc. The main principle is: the power supply device first provides direct current voltage to charge the capacitor, then the thyristor is turned on, and the capacitor discharges to the induction coil, which is arranged on the inner side of the wing skin. Under the action of electric pulse, the coil generates a high-frequency changing magnetic field, and induces eddy currents on the metal skin, forming a pulse force that elastically deforms the skin. The pulse force is small in amplitude, fast in speed and very short in duration, which can effectively crush and remove the ice on the airfoil. Experiments have confirmed that this method has high deicing efficiency and relatively energy saving. Although there are some technical difficulties that need to be overcome, it is still a promising deicing method.

2） Liquid anti-icing form. The liquid anti-icing system sprays anti-icing liquid on the surface to make it mix with the water droplets collected on the surface, in order to lower the freezing point of the mixed liquid to prevent icing. Common anti-icing fluids include ethylene, ethylene glycol, etc., all of which have relatively low freezing points. The advantage of liquid anti-icing is that the effective time is longer, and the anti-icing can last for a period of time after the supply of anti-icing liquid is stopped; the disadvantage is that the aircraft needs to be loaded with a certain amount of anti-icing liquid, which increases the weight of the aircraft.

3） Thermal de-icing form. Modern large airplanes widely use thermal anti-icing systems, which can be divided into gas-thermal anti-icing and electro-thermal anti-icing according to different heat sources. Thermal de-icing mainly uses thermal energy to heat critical surfaces, so that the surface temperature exceeds 0°C, so as to meet the needs of de-icing. Air-heat deicing is to use the high-temperature compressed air generated by the engine compressor as a heat source, and lead it to the surface to be protected, and transfer heat to the surface through hot air to remove ice. Compared with electric heat, the thermal efficiency of gas heat is lower, and the deicing method of continuous heating is generally adopted; in addition, the current aircraft design is developing towards the direction of multi-electric and all-electric, so that the traditional engine bleed air is gradually replaced by electric heat.

Electro-thermal anti-icing is to arrange resistance heating elements on the leading edge of the wing surface and other positions. After power-on, the electric energy is converted into the

thermal energy of the electric heating elements, and then the surface is heated to remove ice. Due to the large amount of power consumption caused by continuous heating, large components such as modern aircraft wings, tails, helicopter rotors, etc., are usually de-iced by periodic heating. This method provides high thermal efficiency and stable working performance, and is also suitable for windshields, sensors and other parts.

1.1.4 The Main Research Methods of Ice Accretion

The main research methods of icing accretion problems include: theoretical analysis, flight test, icing wind tunnel test, and numerical simulation. These research methods complement each other and jointly ensure the success of the research work on the problem of aircraft icing.

1) Theoretical analysis. As a basic research method, theoretical analysis can help researchers clarify some essential characteristics related to ice accretion hidden in experimental phenomena and simulation results. Generally speaking, theoretical analysis will put forward assumptions on practical and complex engineering problems to simplify the analysis. Secondly, by studying some key physical behaviors under the background of the simplified problem, a corresponding mathematical model is established for the problem, then some appropriate boundary conditions are applied to solve the problem. In most cases, due to the complexity of practical problems and the nonlinearity of mathematical models, analytical solutions are difficult to obtain. Therefore, researchers often pursue the numerical solutions, which can be realized by some numerical calculation methods.

The relevant theories of ice accretion are discussed in three main topics: airflow field, water droplet trajectory, and icing behavior. First of all, it is necessary to analyze and model the airflow field to solve the motion of the air and the force applied on the object. The theoretical research on the airflow field has been very mature. Take the flow field around the airfoil as an example: the Euler equation under the inviscid assumption and the Navier-Stokes equation under the viscous condition have long been proposed; for airfoils with complex geometric shapes, The conformal transformation theory can be used; in order to solve the lift force on the airfoil under certain assumptions, the Kutta-Joukowski theorem, the surface vortices method, the lift line method and other theories are introduced; after considering the viscous boundary layer, the Prandtl equation is proposed to deal with the flow in the boundary layer; considering the unsteady flow condition, Theodorsen theory and the subsequent thick airfoil correction theory have been developed successively; the treatment of wake vortices can take advantage of the vortex lattice method or the surface elements method, as well as some related viscosity corrections; turbulence modeling can consider the RANS equations or the LES equations, etc.

Secondly, it is necessary to theoretically analyze the trajectory of water droplets to

determine the amount of water droplets that hit the airfoil and are collected by the airfoil. The most classic theoretical model was proposed by Langmuir and Blodgett, using the Lagrangian method to track the trajectory of supercooled water droplets in the flow field; in addition, the Euler method was also proposed to analyze the collection efficiency of water droplets on the airfoil. After obtaining the amount of water droplets collected by the airfoil, the mass and energy conversion during the ice accretion process can be analyzed to determine the amount of ice accretion within a certain period of time. The classical theory of ice accretion prediction was proposed by Messinger in 1953, and it laid the foundation for most of the subsequent icing prediction code development. In addition, Myers et al. have successively proposed extended theoretical models to deal with the behavior of water films and ice accretion on complex surfaces.

⑵ Flight test. Compared with the other three research methods, the biggest advantage of flight test is that it can use real and natural weather and flight conditions to test and verify the aircraft icing phenomenon and the working state of the anti-icing system, providing the most intuitive and reliable icing data; of course, the disadvantages are also more prominent: high risk of flying with ice, high weather requirements, and high consumption of human and financial resources. In order to relax the weather requirements, reduce the time and cost, and make a controllable assessment of the performance deterioration of the icing parts, the artificial ice shape obtained by the icing wind tunnel experiment can be used in the flight test in some cases. The Federal Aviation Regulations (FAR) in the United States require that, in order to be certified against ice, an aircraft must be certified to operate safely under continuous and intermittent maximum icing conditions specified by the icing envelope. Flight test is an important part of the aircraft certification process due to limited ground simulation capabilities, so it will be very useful in natural or simulated icing conditions.

NASA published a flight test report in 1999[9], which took 51 test flights over four years for the DHC-6 Twin Otter icing research aircraft to demonstrate the effect of the simulated ice accretion on the flight characteristics of the horizontal stabilizer leading edge. Between 2011 and 2021, the German Aerospace Center DLR conducted different flight tests using VFW 614 and Phenom 300 prototypes for supercooled large droplets icing[10]. It can be seen that flight test has always played an indispensable role in ice accretion research.

⑶ Icing wind tunnel experiment. The icing wind tunnel experiment is the most commonly used research method by relevant experimenters. Compared with the flight test, the wind tunnel experiment can create an icing environment more conveniently by controlling the experimental conditions, which is safer and saves costs. The obtained icing experimental data

can not only provide evidence for theoretical analysis and judge the scope of application of the theory; it can also be used in flight tests to help create simulated ice shape and reduce dependence on natural weather; besides, it can also be used with numerical simulation results to compare and verify the correctness of numerical simulation results. Therefore, icing wind tunnel experiment and the design of icing wind tunnels are very important for the study of icing problems. The early icing research in the last century mainly focused on related experiment.

At present, there are not many icing wind tunnels in the world. The representative icing wind tunnels include: the NASA Glenn IRT icing research wind tunnel in the United States, the icing research wind tunnel of the Italian Aerospace Center (CIRA), and the icing wind tunnel of Canadian National Research Council(NRC), etc. Although China started relatively late in icing wind tunnel experiment and icing wind tunnel construction, breakthroughs have been made after many years of research. At present, the China Aerodynamics Research and Development Center(CARDC) has already built the 3m×2m, closed, high subsonic, recirculation type large-scale icing wind tunnel, the key systems of the wind tunnel include: the refrigeration system, the spray system, the anti-icing system, etc., all of these systems work properly to accurately simulate the supercooled cloud environment and ensure the quality of the flow field.

④ Numerical simulation. Numerical simulation for icing problems is considered to be a fast and efficient research method. As mentioned above, the mathematical models obtained by theoretical analysis are often highly nonlinear, and people have to resort to numerical simulation to obtain numerical solutions. Especially with the continuous development of computer technology, the cost of resources required for calculation is continuously reduced, so that many complex engineering problems including ice accretion can obtain satisfactory results through numerical simulation. The numerical simulation of ice accretion generally includes the following steps: 1) Meshing the flow domain, and using open source or commercial CFD software to discretize the airflow field; Carrying out numerical calculation on the flow field to obtain the amount of water droplets collected on the airfoil; 3) According to the thermodynamic model of ice accretion, calculating the mass and heat transfer within each control volume, solving the freezing amount of ice accretion, and determining the ice shape within a certain period of time; 4) Updating the calculation mesh to adapt to the solid airfoil boundary and flow domain after the icing deformation, and re-iteratively solving the airflow field until the predetermined icing time is reached.

1.2 Overview of Previous Research

Regarding the problem of aircraft icing, various research activities have been carried out at different countries from different perspectives and using different research methods. Since this paper studied the icing phenomenon of airfoil and its influence on aerodynamic performance, the previous research progress and research status related to it were mainly discussed and analyzed.

1.2.1 Overview of International Research

International research on the icing of aircraft wings has progressed since the 1960s. As early as the mid-18th century, British Joseph Black proposed the key concept of solid-liquid phase transition problem: latent heat; in 1889, Stefan proposed the classic Stefan problem on the moving boundary of two-phase flow on the basis of earlier research, aiming at discussing the change of boundary position such as gas-liquid, liquid-solid two-phase flow boundary. Wing surface icing generally appears in the cloud with supercooled water droplets, so some scholars have carried out research on cloud physics and the motion trajectory of water droplets: Langmuir and Blodgett published an article in 1946 to describe the basic mathematical formula used to calculate the trajectory of water droplets; Bergrun and Norman[11] in 1947 studied a numerical calculation method of water droplet trajectory to calculate the area and distribution of water droplets impinging on the leading edge of the airfoil, and simulated the water droplet trajectory of the NACA0012 airfoil section; meteorologist Mason, B. J.[12] published the first and second editions of The Physics of Clouds in 1957 and 1971, in which the physical mechanisms associated with clouds were explored in detail, and under certain laboratory conditions, supercooled water droplets were found to exist at temperatures as low as −40°C. At the same time, some scientists worked on establishing the thermodynamic model of ice accretion: Messinger in 1953 revolved around mass balance and energy balance, innovatively proposed the concept of "freezing coefficient", and created the well-known Messinger model. Within the frame of this model, some parameters under flight conditions were combined, such as free stream velocity, altitude, relative heat coefficient, etc., to analyze the change of icing surface equilibrium temperature and the change of ice shape.

After the 1960s, due to the breakthrough of computer technology, Computational Fluid Dynamics (CFD) gradually emerged, and successively developed mesh division technology, numerical simulation technology, etc., which made the simulation of air flow field possible, and also made CFD as one of the main means to study fluid mechanics. There are now many commonly used CFD solvers, including: commercial software, such as Fluent[13], CFX; and open

source software, such as OpenFOAM, SU2[14].

Regarding the trajectory of water droplets, foreign scientists have successively carried out some related researches: in 1984, Gent considered the assumption that small water droplets remain spherical, and Hansman[15] considered the influence of large non-spherical water droplets on ice accretion, respectively gave the formula for calculating the drag coefficient of water droplets related to its Reynolds number, in order to evaluate the aerodynamic drag of water droplets when they move in the flow field; in addition, since the 1980s, the calculation codes of water droplet trajectories in two-dimensional and three-dimensional flow conditions have been successively developed, including: the 2D water droplet trajectory calculation codes written by Meijer in 1987, Gent in 1994, Wright in 1995, Habashi in 1998, Mingione in 1999; and 3D ones written by Bidwell and Potapczuk in 1993, Hedde and Guffond in 1993, Caruso in 1994, and Dart in 1995.

At present, the two mainstream methods for calculating the trajectory of water droplets are the Lagrangian method and the Euler method. The Lagrangian method tracks the trajectory of each single droplet; while the Euler method treats the droplet as another phase, the volume fraction of the droplet and the collection efficiency of the droplet are obtained by solving the governing equations of the droplet phase in the computational mesh, which is suitable for three-dimensional complex surface. In 1997, Yves Bourgault[16] et al. studied the finite element method of the water droplet collision model related to Euler method, and proposed an Euler model for the air flow containing the water droplet phase to calculate the impact of the water droplet on the airfoil.

For the thermodynamic model of ice accretion, most foreign scientists continue to revise and improve it based on the Messinger model, and explore some key parameters contained in the heat balance equation, such as: convective heat transfer coefficient h_c. Smith and Spalding in 1958 proposed the calculation equation of convective heat transfer coefficient in laminar flow condition; Kays and Crawford[17] in 1981 described the calculation method of convective heat transfer coefficient in turbulent flow condition.

Myers et al.[18, 19] proposed the Myers ice accretion models in 2001 and 2004 respectively, which were based on the Messinger model. Compared with the original Messinger model, the Myers models additionally considered the following points: 1) The temperature profile within the ice layer and the water layer was no longer regarded as isothermal, a certain temperature profile was followed instead, and the heat conduction in the layers needs to be considered; 2) The driving force of the water film flow includes not only airflow shear force, but also the own gravity of the water film, surface tension, and pressure

gradient along the airfoil surface.

Based on the Messinger model, NASA developed LEWICE, GlennICE ice accretion calculation software; McGill University in Canada developed the FENSAP-ICE three-dimensional ice accretion solver[20, 21, 22]; based on the Myers model, Politecnico di Milano developed the PoliMIce icing simulation software[23]. This paper mainly used the FENSAP-ICE solver as the calculation tool, which will be described in subsequent chapters.

In recent years, foreign countries have also carried out some latest research work on ice accretion. Giulio Gori, Gianluca Parma et al.[24] proposed a new ice accretion model during flight for rime and clear ice conditions. This model was developed from the Myers ice accretion model and includes an unsteady description of the heat diffusion problem within the ice layer; in addition, local values of air temperature outside the boundary layer were used to calculate convective heat flow, replacing the constant free-flow temperature value considered by the Myers model; Morelli, Bellosta et al.[25] in 2019 based on the Lagrangian method, proposed a new technology for water droplet particle tracking in a deformed slip grid, which was suitable for the flow field solution when the rotor was icing.

Due to the vigorous development of artificial intelligence, machine learning and neural network technology, in 2020, Zhou, Gauger et al.[26] combined computational aeroacoustics and Bayesian neural network technology, and proposed an innovative approach for developing real-time in-flight ice detection system. In this approach, SU2 software was used to calculate the aerodynamic forces experienced by the airfoil at different icing levels, as well as the corresponding far-field noise levels; the resulting data set was then used to construct a Bayesian neural network that provided: a mapping of far-field broadband noise levels to prediction of aerodynamic performance, and uncertainty information to characterize the quality and confidence of those predictions. This work was the first to use high-fidelity acoustic simulations to explore the correlation between airfoil aerodynamic performance and far-field noise levels through machine learning techniques.

1.2.2 Overview of Chinese Research

In China, researchers began to carry out related scientific research work in the 1980s. Han Fenghua of Beihang University and Qiu Xiegang of Nanjing University of Aeronautics and Astronautics edited "Aircraft Anti-Icing System" in 1985[27], in which the anti-icing method, icing calculation and anti-icing system tests were introduced in detail; after that, in 1997 and 1999, Han Fenghua, Chang Shinan et al. conducted research on the icing condition of aircraft radome and the performance verification of anti-icing device. Relevant data showed that before 2000, there was no icing wind tunnel in China that could be used for aircraft anti-icing research.

At that time, the construction of icing wind tunnel still required a long development time.

Aiming at solving the trajectory of water droplets, Yang Shenghua, Lin Guiping, and Shen Xiaobin of Beihang University[29] studied the calculation of the impact characteristics of water droplets on three-dimensional complex surfaces in 2010, and proposed a method to solve the collection efficiency of water droplets based on the Euler two-phase flow model.

In 2011, Yang Shenghua and Lin Guiping[30] established a method for numerical simulation of the icing process based on the time-stepping method(also known as the time multi-stepping method), in order to predict the ice shape of aircraft wing, and built up a software frame for icing; In 2014, Bai junqiang et al.[31] from Northwestern Polytechnical University explored the application of the Euler two-phase flow method in airfoil icing.

Aiming at developing the thermodynamic model of ice accretion, Lei Menglong, Chang Shinan, Yang Bo[32] improved the criterion of clear ice based on the Myers model in 2018, and carried out a three-dimensional icing numerical simulation; Yang Jun, Zhang Bing, and Lu Guofu[33] studied mesh reconstruction and multi-physics coupling methods in numerical simulation of aircraft icing in 2019, and proposed a multi-physics coupling solving platform developed by their research group: EasyCouple.

In addition, some Chinese scholars also discussed aircraft anti-icing/de-icing technology and related issues. In 2013, Wang Chao, Chang Shinan et al.[34] adopted numerical calculation method to study the formation of ice ridges and their influence on the aerodynamic characteristics of the wing during the anti-icing process; in 2015, Hu Qi, Huang Anping and others[35] used Fluent software to analyze the aerodynamic characteristics of NACA23012 and NACA0012 airfoils before and after icing, and pointed out the influence of icing on the lift coefficient. Besides, they also analyzed the existing anti-icing technology and relevant principles of the wing, as well as the advantages and disadvantages; in 2018, Cao Yihua et al.[36] combined with the aviation accident report given by the NTSB, emphasized the continuous impact of aircraft icing on flight safety.

At present, a large-scale icing wind tunnel has been built in China, located in Mianyang, Sichuan, which is convenient for future scientific researchers to conduct more detailed and accurate icing experiments. Some researchers at the wind tunnel laboratory have been working on experimental and numerical simulation studies related to aircraft icing in recent years: in 2010, Yi Xian, Gui Yewei, Zhu Guolin[37] proposed a three-dimensional ice accretion calculation model that considered the backflow effect of liquid water, and based on the criterion of local air velocity direction, established a distribution scheme for the mass of backflow water within the surface elements, and developed a set of calculation methods that can iteratively

solve the icing process in all surface elements at the same time. In 2020, Guo Long, Yi Xian et al.[38] carried out experiments, using high-speed cameras to record the movement and deformation process of water droplets under the action of aerodynamic forces, and divided the deformation of water droplets under acceleration condition into 4 typical shapes: spherical, ellipsoidal, hemispherical and disc, which expanded the research scope of water droplets deformation and corresponding drag characteristics, aimed to explore the occurrence mechanism and essential characteristics of water droplets deformation behavior, and improve the accuracy of icing simulation.

1.3 The Work Done in This Paper

Since the icing problem is a relatively complex engineering problem, considering the time and research cost constraints, this paper focused on the airfoils of aircraft wing, and used numerical simulation as the main research method. According to different airfoils selection, flight conditions and meteorological conditions, combined with qualitative and quantitative analysis, the effect of icing on the aerodynamic characteristics of the airfoils was evaluated, and some reasonable suggestions were put forward.

As mentioned above, the main parameters affecting airfoil icing include: airfoil shapes, free flow velocity, flight angle of attack, ambient temperature, clouds liquid water concentration, median volume diameter of water droplets, etc. If these parameters were considered together, the complexity of the research will increase substantially, and it will be not easy to distinguish the scope and degree of influence of each parameter. Therefore, in this paper, the control variates method was adopted, i.e. each of the above parameters was changed separately under the condition that other parameters were kept unchanged, and the effects of each parameter on the water droplets collection efficiency, ice shape, airfoil surface pressure coefficient and aerodynamic characteristics were analyzed and studied, and then some evaluation conclusion was obtained.

The specific work done in this paper includes the following parts:

（1） Summarize previous research results on ice accretion, and provide reference for this paper;

（2） Introduce the relevant theories, mathematical models and numerical calculation methods of the flow field around the airfoil, the trajectory and collection amount of water droplets, the thermodynamics of ice accretion, and mesh update;

（3） Use Fluent, FENSAP-ICE to build a numerical simulation platform for the airfoil icing problem, design the verification cases and test cases for the numerical simulation, and

make preprocessing; Compare the numerical results of verification cases with reference ice shape given by the existing data to judge the correctness of platform and preprocessing;

（4） Through the established platform, the test cases are simulated in turn, and relevant results are obtained, including: water droplets collection efficiency, ice shape, airfoil surface pressure coefficient, lift-drag coefficient and other data, as well as the pressure and speed cloud map;

（5） Use own post-processing module of Fluent, MATLAB and other tools to analyze and study the airfoil icing results, mainly to study the influence of the above parameters on the icing process and the deterioration of airfoil aerodynamic characteristics;

（6） Summarize the research work done in this paper, give relevant conclusions, and point out possible directions and expectations for further research.

Chapter 2 Analysis of Flow Field Around Airfoil

2.1 Foreword

The primary entry point to study the airfoil icing problem is the analysis and calculation of the flow field around the airfoil, because the water droplets will be subjected to the force from the air flow when they move in the flow field, and the velocity vector distribution of the air flow needs to be known in advance before the water droplets can be affected. The motion trajectory is judged to determine the amount of water droplets that can be intercepted by the airfoil. Therefore, this chapter mainly focuses on the airflow field, analyzing the governing equations and related numerical solutions.

During the actual flight of the aircraft, there is a thin boundary layer on the airfoil, in which a strong viscous shear and heat exchange will occur; in addition, due to the icing of the airfoil studied in this paper, the airfoil shape may have significant changes after a period of time, which can result in airflow separation. Therefore, in the analysis of the flow field around the airfoil, it is necessary to consider the airflow viscosity, which is shown in the Navier-Stokes governing equation.

Considering the actual airfoil shape and when the ice “horn” formed by ice accretion separates the airflow, turbulence often exists, and an appropriate turbulence model needs to be selected for solving problem. At present, there are three main ways to deal with turbulence: 1) Direct Numerical Simulation(DNS); 2) Large Eddy Simulation(LES); 3) Reynolds-Averaged N-S Equations(RANS). Because the first two methods require large computing resources and take a long time, this paper chooses the RANS method to calculate the time-averaged flow field, which is also the most mature method for engineering applications at present. To close the governing equations, the RANS turbulence model chooses the *SST* k-ω two-equations model.

2.2 Governing Equations of Airflow Field

Airflow governing equations include: continuity equation, momentum equation and energy equation. According to the different forms of Lagrangian method and Euler method to describe the equation system, it can be divided into conservative form and non-conservation form; in addition, according to the range of the control body, it can be divided into integral form and differential form. The field of computational fluid dynamics generally favors the governing equations in the conservative form. The following two expressions of the two-dimensional N-S equations in the form of the conservative differential and the conservative integral will be given

in the Cartesian coordinate system.

2.2.1 Conservative Differential 2D N-S Equations

Conservative Differential form(ignoring air gravity term):

$$\frac{\partial \rho}{\partial t}+\frac{\partial(\rho u)}{\partial x}+\frac{\partial(\rho v)}{\partial y}=0 \tag{2.1}$$

$$\frac{\partial(\rho u)}{\partial t}+\frac{\partial(\rho u^2+p)}{\partial x}+\frac{\partial(\rho uv)}{\partial y}=\frac{\partial \tau_{xx}}{\partial x}+\frac{\partial \tau_{yx}}{\partial y} \tag{2.2}$$

$$\frac{\partial(\rho v)}{\partial t}+\frac{\partial(\rho uv)}{\partial x}+\frac{\partial(\rho v^2+p)}{\partial y}=\frac{\partial \tau_{xy}}{\partial x}+\frac{\partial \tau_{yy}}{\partial y} \tag{2.3}$$

$$\begin{aligned}&\frac{\partial[\rho\left(e+\frac{U^2}{2}\right)]}{\partial t}+\frac{\partial[\rho\left(e+\frac{U^2}{2}\right)u+pu]}{\partial x}+\frac{\partial[\rho\left(e+\frac{U^2}{2}\right)v+pv]}{\partial y}\\&=\frac{\partial(k\frac{\partial T}{\partial x}+u\tau_{xx}+v\tau_{xy})}{\partial x}+\frac{\partial(k\frac{\partial T}{\partial y}+u\tau_{yx}+v\tau_{yy})}{\partial y}\end{aligned} \tag{2.4}$$

Equation (2.1) represents the continuity equation, where ρ represents air density, t represents time, u and v represent the velocity components of the airflow along the directions x and y of the Cartesian coordinate system, respectively; Equations (2.2) and (2.3) represent the momentum equations , where p represents the air pressure, τ_{xx}, τ_{yx}, τ_{xy}, τ_{yy} represent the viscous shear stress components; Equation (2.4) represents the energy equation, where e represents the internal energy per unit mass of fluid, U represents the airflow velocity magnitude, k represents the thermal conductivity, T represents the temperature.

In addition, the above equations can be expressed in the following form[39]:

$$\frac{\partial \vec{\Psi}}{\partial t}+\frac{\partial \vec{F}}{\partial x}+\frac{\partial \vec{G}}{\partial y}=0 \tag{2.5}$$

In formula (2.5), $\vec{\Psi}$ represents the conserved variable vector, and $\vec{F}$ and $\vec{G}$ represent the corresponding flux vectors:

$$\vec{\Psi} = \begin{bmatrix} \rho \\ \rho u \\ \rho v \\ \rho\left(e + \frac{U^2}{2}\right) \end{bmatrix} \tag{2.6}$$

$$\vec{F} = \begin{bmatrix} \rho u \\ \rho u^2 + p - \tau_{xx} \\ \rho uv - \tau_{xy} \\ \rho\left(e + \frac{U^2}{2}\right)u + pu - k\frac{\partial T}{\partial x} - u\tau_{xx} - v\tau_{xy} \end{bmatrix} \tag{2.7}$$

$$\vec{G} = \begin{bmatrix} \rho v \\ \rho uv - \tau_{yx} \\ \rho v^2 + p - \tau_{yy} \\ \rho\left(e + \frac{U^2}{2}\right)v + pv - k\frac{\partial T}{\partial y} - u\tau_{yx} - v\tau_{yy} \end{bmatrix} \tag{2.8}$$

The viscous shear stress components in the above expressions can form a shear stress matrix $\tilde{\tau}$:

$$\tilde{\tau} = \begin{bmatrix} \tau_{xx} & \tau_{xy} \\ \tau_{yx} & \tau_{yy} \end{bmatrix} \tag{2.9}$$

The above components can be further expressed by the constitutive relationship between stress and strain as:

$$\begin{aligned} \tau_{xx} &= \lambda\left(\frac{\partial u}{\partial x} + \frac{\partial v}{\partial y} + \frac{\partial w}{\partial z}\right) + 2\mu\frac{\partial u}{\partial x} & \tau_{xy} &= \mu\left(\frac{\partial u}{\partial y} + \frac{\partial v}{\partial x}\right) \\ \tau_{yx} &= \tau_{xy} & \tau_{yy} &= \lambda\left(\frac{\partial u}{\partial x} + \frac{\partial v}{\partial y} + \frac{\partial w}{\partial z}\right) + 2\mu\frac{\partial v}{\partial y} \end{aligned} \tag{2.10}$$

μ represents the air dynamic viscosity coefficient, and λ represents the second viscosity coefficient (also known as the bulk viscosity coefficient); for the general airfoil flow field, it can be obtained from the Stokes relationship:

$$\lambda = -\frac{2}{3}\mu \tag{2.11}$$

It is not difficult to find by observing the system of equations: the unknown quantities include not only the vector $\vec{\Psi}$, but also the air pressure p and temperature T, the number of equations is less than the number of unknowns, so for compressible flow, it is necessary to introduce the gas state equation and the relationship between pressure and internal energy to close the equations. Treating air as an ideal gas, using the ideal gas assumption:

$$p = \rho RT, \qquad p = (\gamma - 1)\rho e \tag{2.12}$$

R represents the gas constant of air, and its value is 287 $\mathrm{J/(kg \cdot K)}$; γ represents the specific heat ratio, in practice γ is the ratio of constant pressure specific heat C_p to constant volume specific heat C_v. If it is assumed that C_p and C_v do not change with temperature T, then γ can take 1.4 as its value. This assumption is applicable in this study.

Since the maximum flight speed selected in this study is 105m/s, the Mach number is about 0.3, and the air density ρ can be approximately regarded as a constant, the continuity equation and momentum equation of the above equations can be solved by decoupling from the energy equation. At this time, the unknowns include ρu, ρv, p, T, and the system of equations is closed.

It is still necessary to pay attention to the dynamic viscosity coefficient μ and the thermal conductivity k. Generally speaking, the higher the temperature of air, the larger the value of μ. Therefore, there are some formulas between μ and temperature T. This research will adopt Sutherland law, which is the most commonly used formula in numerical simulations at present:

$$\frac{\mu}{\mu_0} = (\frac{T}{T_0})^{\frac{3}{2}} \frac{T_0 + S_\mu}{T + S_\mu} \tag{2.13}$$

In the expression (2.13), μ_0 is the reference viscosity coefficient with a value of $1.716 \cdot 10^{-5} Pa \cdot s$; T_0 is the reference temperature with a value of 273K; S_μ is the effective temperature (also known as the Sutherland constant) with a value of 111K.

For the thermal conductivity k, it can be related to the constant pressure specific heat C_p and the dynamic viscosity coefficient μ by the Prandtl number P_r:

$$Pr = \frac{\mu/\rho}{k/(C_p\rho)} = \frac{C_p\mu}{k} \tag{2.14}$$

The Prandtl number actually reflects the ratio of the fluid momentum diffusivity to the heat diffusivity. The Prandtl number P_r of air is generally around 0.7; the constant pressure specific heat C_p of air is about 1006.43 $\mathrm{J/(kg \cdot K)}$.

Through the above analysis, the two-dimensional N-S equations in the conservative differential form have been constructed; however, when there are some discontinuities in the flow field (such as shock waves), the above differential form equations cannot accurately describe those discontinuities; in addition, the finite volume method commonly used in CFD needs to consider the physical variables and interface fluxes for each control volume, so the N-S equations in the form of conservative integral need to be given.

2.2.2 Conservative Integral Form 2D N-S Equations

For the obtained conservative differential equations, the volume integral of them within the finite control volume can be performed, and the Gaussian divergence theorem can be used to convert the volume integral of the convection term, diffusion term and pressure gradient term into the directed surface integral around the boundaries of the control volume, finally the corresponding conservative integral equations can be obtained:

$$\frac{\partial}{\partial t}\int_V \rho \, dV + \oint_{\partial V} \rho \vec{v} \cdot \vec{n} dS = 0 \tag{2.15}$$

$$\frac{\partial}{\partial t}\int_V \rho \vec{v} \, dV + \oint_{\partial V} \rho \vec{v}(\vec{v} \cdot \vec{n}) dS = -\oint_{\partial V} p\vec{n} dS + \oint_{\partial V} (\tilde{\tau} \cdot \vec{n}) dS \tag{2.16}$$

$$\begin{aligned} \frac{\partial}{\partial t}\int_V E^t \, dV + \oint_{\partial V} E^t(\vec{v} \cdot \vec{n}) dS \\ = -\oint_{\partial V} (p\vec{v}) \cdot \vec{n} dS + \oint_{\partial V} (\vec{v} \cdot \tilde{\tau}) \cdot \vec{n} dS + \oint_{\partial V} k\vec{\nabla} T \cdot \vec{n} dS \end{aligned} \tag{2.17}$$

The above expressions solve the volume integral within the control volume V, and solve the surface integral along the control volume boundaries ∂V; $\vec{n}$ represents the normal vector of the boundaries that is directed outward and is perpendicular to the surface; $\vec{v}$ represents the flow velocity vector; E^t represents the total energy per unit volume, which is:

$$E^t = \rho(e + \frac{U^2}{2}) \tag{2.18}$$

2.3 Numerical Calculation Method

In order to solve the actual flow field problem, numerical calculation methods are widely used at present, dividing the flow domain to be solved into a sufficient number of computational grids, and solving the discrete problem under the finite volume. The field of computational mechanics often adopts the following three methods: 1) Finite Element Method (FEM); 2) Finite Difference Method (FDM); 3) Finite Volume Method (FVM). FEM first constructs and uses trial functions to weakly formalize the original equations, then discretely represents the continuous physical quantities in the solution domain with basis functions and physical quantities at the computational nodes, and finally solves numerically; FDM is based on Taylor series expansion, using the difference quotient of the physical quantities on the adjacent grid nodes to replace the partial derivatives of the above-mentioned differential form governing equations, and an algebraic equation system is established to solve the physical quantities of the nodes; however, most CFD solvers currently use FVM, so this section focuses on the finite volume method.

2.3.1 Discrete Solving Domain and Equations

The above conservative integral N-S equations need to be discretized first in order to solve the governing equations for each finite volume. The finite volume after meshing is shown in Figure 2.1:

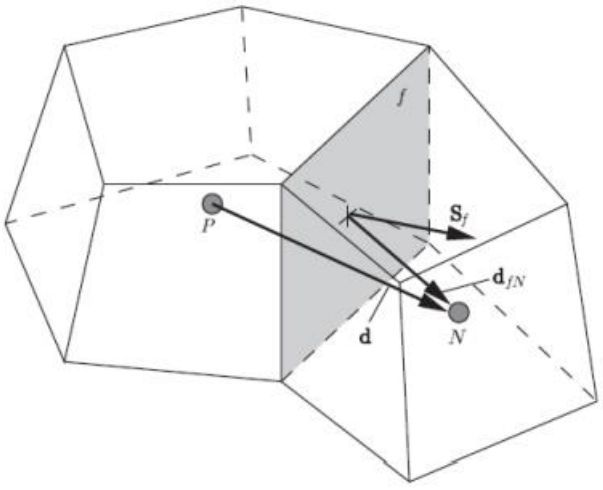

Figure 2.1 The schematic diagram of the finite volume

The figure above shows two finite control volumes, in which point P and point N are the center points of each control volume, all physical quantities are defined at the center point, and *f*

is the interface between the two control volumes. If the individual control volume is denoted as V_i, and the total number of control volumes after meshing is denoted as N_{tot}, then the entire flow field V can be expressed as:

$$V = \bigcup_{i=1}^{N_{tot}} V_i, \qquad \text{and } V_i \cap V_j = 0 \ \ \forall i \neq j \tag{2.19}$$

That is, the entire flow field is completely divided by N_{tot} control volumes without volume overlap. According to the different selection of the center point of the control volume, it can be divided into the cell-centered control volume and the node-centered control volume. The Fluent solver adopts the first form; while the SU2 solver takes the second form.

The semi-discrete N-S equation for each control volume is as follows:

$$\frac{d}{dt}\int_{V_i} \rho\phi dV + \oint_{\partial V_i} \rho\phi(\vec{v}\cdot\vec{n})dS = \oint_{\partial V_i} \Gamma^{\phi}\,\vec{\nabla}\phi\cdot\vec{n}dS + \int_{V_i} Q^{\phi}dV \tag{2.20}$$

ϕ in the above equation is a generalized physical quantity, which can represent any field, such as velocity field $\vec{v}$, temperature field T, etc.; Γ^{ϕ} represents the generalized diffusion coefficient corresponding to ϕ, and Q^{ϕ} represents the generalized source/sink term of ϕ, such as the pressure gradient term. Therefore, the above equations consist of unsteady term, convection term, diffusion term, and source/sink term, each of which can be discretely interpolated to realize a system of equations for numerical calculation.

The discrete N-S equation is expressed as:

$$|V_i|\frac{d(\rho\phi)_P}{dt} + \sum_{f\in\partial V_i}(\rho\phi)_f\left(\vec{v}_f\cdot\overrightarrow{S_f}\right) = \sum_{f\in\partial V_i}\Gamma_f^{\phi}(\vec{\nabla}\phi_f\cdot\overrightarrow{S_f}) + |V_i|Q_P^{\phi} \tag{2.21}$$

The unsteady term and source/sink term in equation (2.21) are represented by physical quantities at the center point P of the control volume; while the convection and diffusion terms are represented by physical quantities on each interface. The interface physical quantities are often obtained by interpolating between the physical quantities of center points. The following will analyze the specific discrete schemes such as convection terms and diffusion terms, and the corresponding calculation method.

2.3.2 Discrete Schemes

Common discrete schemes for CFD[40] include first-order upwind scheme, power scheme, central difference scheme, second-order upwind scheme, and QUICK scheme. In this study, the convection term in the above equation is discretized by the second-order upwind scheme, and the diffusion term is discretized by the central difference scheme.

First, the second-order upwind scheme adopted by the convection term is analyzed. Compared with the first-order upwind scheme, the second-order upwind scheme has second-order accuracy, the truncation error is relatively smaller, but sometimes oscillation may occur. Therefore, gradient limiters can be used to ensure the stability of the simulation. At present, the CFD numerical simulation basically adopts the second-order or higher precision scheme to calculate the convection term; the first-order precision scheme can ensure the convergence of the simulation for the possible instability of the initial flow field calculation, and the result can be taken as the initial solution for the subsequent calculation using the second-order upwind scheme, to ensure the accuracy of final solution.

Take Figure 2.1 as an example to illustrate the principle of the second-order upwind scheme. Assume that the generalized physical quantities at the center point P of the master control volume and those at the center point N of the adjacent control volume are known, and they are denoted as ϕ_P and ϕ_N; if the physical quantity ϕ_f at the center of the interface f needs to be solved, the interpolation for it should be given. The interpolation under the upwind scheme depends on the direction of the mass flux at the center of the interface f, and this mass flux F_f is expressed as:

$$F_f = \rho_f \vec{v}_f \cdot \overrightarrow{S_f} \tag{2.22}$$

If $F_f > 0$, it means that the mass flows out from the master control volume and enters the adjacent control volume; if $F_f < 0$, it means that the mass flows out from the adjacent control volume and enters the master control volume. Depending on the directionality of F_f, ϕ_f can be defined as:

$$\phi_f = \begin{cases} \phi_P + (\vec{\nabla}\phi)_P \cdot \overrightarrow{d_{Pf}} & F_f > 0 \\ \phi_N + (\vec{\nabla}\phi)_N \cdot \overrightarrow{d_{Nf}} & F_f < 0 \end{cases} \tag{2.23}$$

$\overrightarrow{d_{Pf}}$, $\overrightarrow{d_{Nf}}$ represent the distance vectors from the center points P and N to the interface f.

Here ϕ_f is always judged and calculated according to the stored information of upstream center point, hence the name of the upwind scheme. This scheme not only includes the physical quantities of the nearest upstream center point, but the introduction of the gradient term also includes the physical quantities of other upstream center points. Since the change between the physical quantities at the center point and the physical quantities at the interface is linear, this scheme has second-order accuracy. However, if the calculated gradient is too steep, ϕ_f will be larger than ϕ_P and ϕ_N, and the solution will oscillate and affect convergence. So the gradient limiter function φ can be used to control the gradient (assuming the upstream center point is P):

$$\phi_f = \phi_P + \varphi(\vec{\nabla}\phi)_P \cdot \vec{r} \quad 0 \le \varphi \le 1 \tag{2.24}$$

If the value of φ in the above formula is 1, the limiter does not work, and the second-order upwind scheme is still used; if the value of φ in the above formula is 0, the physical quantity ϕ_f at the interface f is directly determined by the nearest upstream center point, at this time the formula degenerates into a first-order upwind scheme. Due to scope limitation, this paper will not discuss the selection of φ in detail.

Secondly, the central difference scheme adopted by the diffusion term and the calculation method of the physical quantity gradient are analyzed. Diffusion term contains the diffusion coefficient Γ^{ϕ}, usually the Γ_f^{ϕ} at the interface f is obtained by linear interpolation of the diffusion coefficient Γ_P^{ϕ} at the center point P of the master control volume and the diffusion coefficient Γ_N^{ϕ} at the center point N of the adjacent control volume:

$$\Gamma_f^{\phi} = \Gamma_P^{\phi} + \frac{\overrightarrow{d_{Pf}}}{\vec{d}}(\Gamma_N^{\phi} - \Gamma_P^{\phi}) \tag{2.25}$$

$\vec{d}$ represents the distance vector between the center point P and the center point N.

For non-orthogonal surfaces (that is, $\overrightarrow{S_f}$ is not parallel to $\vec{d}$), the $\vec{\nabla}\phi_f \cdot \overrightarrow{S_f}$ at the interface f can be divided into orthogonal term and non-orthogonal term. The orthogonal term is represented by the central difference between the value ϕ_P at the center point P of the master control volume and the value ϕ_N at the center point N of the adjacent control volume, while the non-orthogonal term is still represented by $\vec{\nabla}\phi_f$:

$$\vec{\nabla}\phi_f \cdot \overrightarrow{S_f} = A(\phi_N - \phi_P) + \vec{a} \cdot \vec{\nabla}\phi_f \tag{2.26}$$

The first term in the formula is the orthogonal term, which represents the component of the gradient at the interface f along the direction of $\vec{d}$; and the second term is non-orthogonal term, which means that the gradient at the interface f is perpendicular to the direction of $\vec{d}$ or is at a certain angle, and needs to be further dealt with.

A and $\vec{a}$ can be written as:

$$A = \frac{|S_f|^2}{\overrightarrow{S_f} \cdot \vec{d}} \qquad \vec{a} = \overrightarrow{S_f} - A\vec{d} \tag{2.27}$$

The gradient $\vec{\nabla}\phi_f$ at the interface that still exists in the non-orthogonal term can be obtained by interpolating the gradients at the center points of the control volumes:

$$\vec{\nabla}\phi_f = \vec{\nabla}\phi_P + \frac{\overrightarrow{d_{Pf}}}{\vec{d}}(\vec{\nabla}\phi_N - \vec{\nabla}\phi_P) \tag{2.28}$$

Finally the formula about $\vec{\nabla}\phi_f \cdot \overrightarrow{S_f}$ can be written as:

$$\vec{\nabla}\phi_f \cdot \overrightarrow{S_f} = A(\phi_N - \phi_P) + \vec{a} \cdot \vec{\nabla}\phi_P + \frac{\overrightarrow{d_{Pf}}}{\vec{d}}(\vec{\nabla}\phi_N - \vec{\nabla}\phi_P) \tag{2.29}$$

The above formula performs interpolation on orthogonal term and non-orthogonal term respectively, mainly considering the saving of computing resource and the accuracy of calculation: the computing resource required for the central difference calculation of orthogonal term is small, and the separate calculation can make the obtained results more accurate.

The central difference scheme makes the change between the center points of the control volumes linear, this scheme satisfies the second-order accuracy, and a relatively accurate solution can be obtained; however, this scheme is also regarded as unbounded and non-directional, and the numerical solution may oscillate. Therefore, the central difference scheme is generally used for the discretization of the diffusion term, but not for the discretization of the convection term.

Since the above calculation analysis includes the gradient terms at the center points, it is

also necessary to calculate the gradient of each physical field at the center point of each control volume. In this study, the weighted least squares cell-based gradient method is used to solve the gradient at the center point, including velocity gradient $\vec{\nabla}\vec{v}$, pressure gradient $\vec{\nabla}p$, temperature gradient $\vec{\nabla}T$, etc. Compared with the Green-Gauss method, this method does not need to use the physical quantities on the interface, but takes advantage of the physical quantities stored at the center points to find their gradient. Figure 2.1 is still used as an example to illustrate the calculation method of the temperature gradient $\vec{\nabla}T$, and the gradients of other physical fields can be obtained in the same way.

Denote the temperature at the central point P of the master control volume as T_P, and the temperature at the central point N of the adjacent control volume as T_N, and the two can be related by the gradient $(\vec{\nabla}T)_P$ at point P:

$$T_N = T_P + \vec{d} \cdot (\vec{\nabla}T)_P \tag{2.30}$$

Both T_P and T_N in this formula are known quantities, and the quantity to be determined is the gradient $(\vec{\nabla}T)_P$. The above formula is only for the master control volume and one of the adjacent control volumes, if all adjacent control volumes are considered (the number is set as t), then a set of equations related to the gradient of point P will be obtained, in which the unknowns are all the same, namely $(\vec{\nabla}T)_P$. The general form of this system of equations can be expressed as:

$$T_{N_i} - T_P = \vec{d}_{PN_i} \cdot \left(\vec{\nabla}T\right)_P \quad i = 1, 2, \dots, t \tag{2.31}$$

The above equations are expressed in matrix form as:

$$\left[\vec{d}\right]\left[\left(\vec{\nabla}T\right)_P\right] = [T_N - T_P] \tag{2.32}$$

Observing the above formula, it can be seen that the number of equations is controlled by the number of adjacent control volumes. In the two-dimensional case, if triangular mesh is used, the number of equations is 3; if quadrilateral mesh is used, the number of equations is 4. The number of unknowns is determined by the two directional components of the temperature

gradient, namely $(\frac{\partial T}{\partial x})_P$ and $(\frac{\partial T}{\partial y})_P$. In fact, the coefficient matrix $[\vec{d}]$ of this system of equations is not a square matrix, and the number of equations is greater than or equal to the number of unknowns. At this time, the calculation idea of the problem is to construct the cost function C, and use the weighted least squares method to obtain an approximate solution of the temperature gradient $(\vec{\nabla}T)_P$, so that the sum of squared errors of the above equations is minimized. The error e_i for each equation is expressed as:

$$e_i = (T_{N_i} - T_P) - \left[\vec{d}_{PN_i} \cdot (\vec{\nabla}T)_P\right] \quad i = 1, 2, \dots, t \tag{2.33}$$

The cost function C and the corresponding solution objective C_{min} are expressed as:

$$C = \sum_{i=1}^{t} (W_i e_i)^2 \quad C_{min} = \min(C) \tag{2.34}$$

The W_i in the formula is the weight coefficient constructed for the error e_i of each equation. The basic idea is to judge the distance between the center points of adjacent control volumes. If the distance $|\vec{d_i}|$ between the two points is smaller, then assign e_i larger weight W_i. It can be expressed as the inverse of the distance:

$$W_i = \frac{1}{|\vec{d_i}|} \tag{2.35}$$

Finally, the expression of the gradient at the center point $(\vec{\nabla}T)_P$ can be obtained:

$$(\vec{\nabla}T)_P = (\tilde{d}^T \widetilde{W}^T \widetilde{W} \tilde{d})^{-1} \tilde{d}^T \widetilde{W}^T \widetilde{W} (\widetilde{T_N} - \widetilde{T_P}) \tag{2.36}$$

The above formula uses "~" to represent the matrices, where the $\tilde{d}$ matrix is composed of the distance vector between the master control volume and each adjacent control volume. In the two-dimensional case, its dimension is $t \times 2$; the $\widetilde{W}$ matrix is a diagonal matrix composed of weight coefficients W_i, and it is a square matrix of order $t \times t$; $\widetilde{T_N} - \widetilde{T_P}$ is the difference vector between the values at the center points, which is a column vector of $t \times 1$. Finally, the gradient

value at the center point *P* of the master control volume can be obtained by this formula.

After dealing with the discrete schemes of the convection term, the diffusion term and the gradient term, it is necessary to discuss the processing of the pressure gradient term, and explain the calculation method of pressure and velocity in the flow field.

The pressure gradient term, which drives the flow around the airfoil, is important in the momentum equation, so it needs to be dealt with separately. The volume integral of the pressure gradient in the control volume can be transformed into the following form:

$$\int_{V_i} -\vec{\nabla} p dV = \oint_{\partial V_i} -p\vec{n}dS = -\sum_{f\in\partial V_i} p_f \overrightarrow{S_f} \tag{2.37}$$

Now we need to solve the pressure value p_f on each interface. This study uses the second-order scheme to interpolate the pressure on the interface. The specific expression is as follows:

$$p_f = \frac{1}{2}(p_P + p_N) + \frac{1}{2}[(\vec{\nabla} p)_P \cdot \overrightarrow{d_{Pf}} + (\vec{\nabla} p)_N \cdot \overrightarrow{d_{Nf}}] \tag{2.38}$$

This expression actually uses the central difference scheme to construct the interface pressure p_f, and the pressure and pressure gradient on the right-hand side of the expression are stored at the center point of the control volume.

The above analysis assumes that the physical quantities stored at each center point are known, and then a discrete equation system for the physical quantities at the center points is constructed. In order to solve the equation system, it is necessary to impose certain definite conditions, and use the iterative method to deal with nonlinear and coupling problems. The calculation method is explained below:

For flows with relatively low velocities, Fluent and other solvers are generally based on pressure, and can use two different calculation methods: one is to decouple pressure p from velocity $\vec{v}$, express the pressure by using a separate Poisson equation, and then the unknown variables in the governing equations are solved in sequence, and the iterative steps are repeated until the numerical solution converges. This algorithm is called the separation algorithm, represented by the SIMPLE algorithm and the later modified SIMPLEC algorithm[41]. The idea of the SIMPLE algorithm includes: 1) Use the initial guessed pressure to numerically solve the momentum equation to obtain the initial velocity field, which may

not satisfy the continuity equation; 2) Use the velocity field to numerically solve the Poisson equation about the pressure p, for the pressure correction; 3) Use the new decomposition form of the pressure field and the momentum equation to correct the velocity field to satisfy the continuity equation, and it is judged whether this new velocity field satisfies the momentum equation; 4) In the loop, use the new pressure field and velocity field, numerically solve the energy equation and turbulence transport equations; 5) Repeat the loop, and finally make each physical quantities satisfy the governing equations. In order to solve the possible discrete problem of the pressure gradient in the iterative steps, the algorithm generally adopts the staggered grid technology to ensure the correct calculation, which will not be discussed too much here.

Another method is to directly couple pressure and velocity, corresponding to the so-called coupled algorithm. The difference between the coupled algorithm and the SIMPLE algorithm above is that the coupled algorithm solves the momentum equation and the continuity equation based on the pressure representation simultaneously, instead of calculating unknowns sequentially based on the above steps. It can be seen that the memory resources consumed by the coupled algorithm are relatively large, but the convergence speed is relatively fast. In this study, the coupled algorithm is used to calculate discrete equations.

2.4 Selection of Turbulence Model

According to the processing approach of Reynolds stress in RANS equations, turbulence models can be divided into two categories: the first category is based on Boussinesq assumption, and the Reynolds stress is represented by the construction of turbulence viscosity. At present, about 95% of RANS models belong to this category; The second category is the direct modeling of the Reynolds stress tensor. This category is developed relatively late, and only about 5% of the RANS models belong to this category. In this study, the possible effects of turbulence after airfoil icing are considered, and the $SST\ k$-ω turbulence model is selected, which is included in the first-class RANS model.

In reality, many irregular flows can be regarded as turbulence. The RANS equations deal with turbulence by performing Reynolds decomposition on the physical quantities in the flow, which are expressed as time-averaged quantities and fluctuating quantities. For example, the velocity component u in the direction of x can be decomposed into time-averaged velocity $\bar{u}$ and fluctuating velocity u':

$$u = \bar{u} + u' \tag{2.39}$$

Among them, $\bar{u}$ is a time-averaged quantity, independent of time; and u' is a fluctuating quantity, and its time-averaged result is 0. Through the above decomposition, the constructed incompressible flow RANS equations are as follows:

$$\vec{\nabla} \cdot \bar{\vec{u}} = 0 \tag{2.40}$$

$$\vec{\nabla} \cdot \left(\rho \bar{\vec{u}} \bar{\vec{u}}\right) + \vec{\nabla} \cdot \left(\rho \overline{\vec{u}' \vec{u}'}\right) = -\vec{\nabla} \bar{p} + \mu \vec{\nabla}^2 \bar{\vec{u}} \tag{2.41}$$

Observing the above equations, it can be found that the convection term, diffusion term and pressure gradient term in the original N-S equations still exist in RANS equations, but the system of RANS equations has an extra term: $\vec{\nabla} \cdot \left(\overline{\vec{u}' \vec{u}'}\right)$, which causes the system to be unclosed. Generally, $-\rho \overline{\vec{u}' \vec{u}'}$ is called the Reynolds stress tensor, which can be expressed in the matrix form:

$$-\rho \overline{\vec{u}' \vec{u}'} = \begin{bmatrix} -\rho \overline{u'u'} & -\rho \overline{u'v'} \\ -\rho \overline{v'u'} & -\rho \overline{v'v'} \end{bmatrix} \tag{2.42}$$

u' and v' in the above matrix represent the fluctuating components of the velocity along the directions of x and y, respectively. Reynolds stress reflects the effect of turbulent fluctuation on time-averaged motion, which can be decomposed into isotropic and anisotropic terms:

$$-\rho \overline{u'u'} = -\frac{2}{3} \rho k + a_{xx} \tag{2.43}$$

$$-\rho \overline{u'v'} = a_{xy} \tag{2.44}$$

$$-\rho \overline{v'v'} = -\frac{2}{3} \rho k + a_{yy} \tag{2.45}$$

k in the isotropic term represents the turbulent kinetic energy, and the terms a_{xx}, a_{xy}, a_{yy}, etc., as the anisotropic terms, can be expressed through the Boussinesq hypothesis:

$$a_{xx} = 2\rho\nu_t(\vec{x})\frac{\partial\bar{u}}{\partial x} \tag{2.46}$$

$$a_{xy} = \rho\nu_t(\vec{x})(\frac{\partial\bar{u}}{\partial y} + \frac{\partial\bar{v}}{\partial x}) \tag{2.47}$$

$$a_{yy} = 2\rho\nu_t(\vec{x})\frac{\partial\bar{v}}{\partial y} \tag{2.48}$$

$\nu_t(\vec{x})$ is called turbulent viscosity or eddy viscosity, and it is related to the spatial location of the flow. Define effective viscosity $\nu_e(\vec{x})$:

$$\nu_e(\vec{x}) = \nu + \nu_t(\vec{x}) \tag{2.49}$$

where ν represents the kinematic viscosity of air. With the above construction, the momentum equation can be re-expressed as:

$$\vec{\nabla}\cdot\left(\rho\bar{\vec{u}}\bar{\vec{u}}\right) = -\vec{\nabla}\bar{p} + \vec{\nabla}\cdot[\rho\nu_e(\vec{x})\vec{\nabla}\bar{\vec{u}}] \tag{2.50}$$

If an expression of $\nu_t(\vec{x})$ is given, then the momentum equation in this form, combined with the continuity equation, etc., will reconstitute a closed system. Therefore, the RANS turbulence model based on the Boussinesq assumption mainly considers how to give $\nu_t(\vec{x})$. According to the number of extra introduced transport equations, it can be divided into algebraic model(it is also known as zero-equation model), one-equation model, two-equation model and so on. This section mainly describes the *SST k-ω* turbulence model used.

In fact, the *SST k-ω* turbulence model combines the advantages of the *k-ε* model and the *k-ω* model. Each of these two models contains two additional transport equations: the *k-ε* model contains model equations for turbulent kinetic energy k and dissipation rate ε of turbulent kinetic energy, which can better simulate shear flow, and performs well away from the wall; while the *k-ω* model contains model equations for turbulent kinetic energy k and turbulent frequency ω, which performs well within the near-wall region and is more numerically stable. *SST k-ω* turbulence model is a linear combination of the above two models in the form of a mixed equation to exert their respective performances. The transport

equations of the model are directly given below, and the detailed derivation will not be further discussed:

$$\bar{u}\frac{\partial k}{\partial x}+\bar{v}\frac{\partial k}{\partial y}=\frac{\partial}{\partial x}\left[(\nu+\sigma_k\nu_t)\frac{\partial k}{\partial x}\right]+\frac{\partial}{\partial y}\left[(\nu+\sigma_k\nu_t)\frac{\partial k}{\partial y}\right]+P_k-C_\mu\omega k \tag{2.51}$$

$$\begin{aligned}\bar{u}\frac{\partial \omega}{\partial x}+\bar{v}\frac{\partial \omega}{\partial y}=&\frac{\partial}{\partial x}\left[(\nu+\sigma_\omega\nu_t)\frac{\partial \omega}{\partial x}\right]+\frac{\partial}{\partial y}\left[(\nu+\sigma_\omega\nu_t)\frac{\partial \omega}{\partial y}\right]+\gamma\frac{\omega}{k}P_k-\beta\omega^2\\&+(1-F_1)\frac{2\sigma_{\omega 2}}{\omega}\left(\frac{\partial k}{\partial x}\frac{\partial \omega}{\partial x}+\frac{\partial k}{\partial y}\frac{\partial \omega}{\partial y}\right)\end{aligned} \tag{2.52}$$

The left-hand side terms of the above two transport equations are the convection terms; the first two terms on the right-hand side of the equations are the viscous diffusion terms; the third terms are the generation terms of k and ω, respectively; the fourth terms are the dissipation terms; the last term of the turbulent frequency ω transport equation can be regarded as a cross-diffusion term, which can be combined or switched between the k-ε model and the k-ω model, controlled by the mixing equation $F1$:

$$F_1=\tanh(\zeta),\qquad \zeta=\{\min\left[\max\left(\frac{\sqrt{k}}{C_\mu\omega y},\frac{500\nu}{y^2\omega}\right),\frac{4\sigma_{\omega 2}k}{CD_{k\omega}y^2}\right]\}^4 \tag{2.53}$$

$$CD_{k\omega}=\max\left(\rho\frac{2\sigma_{\omega 2}}{\omega}\frac{\partial k}{\partial x_i}\frac{\partial \omega}{\partial x_i},10^{-10}\right) \tag{2.54}$$

When $F1$ = 0, the above equation is the k-ω model equation; when $F1$ = 1, the cross-diffusion term is discarded, and the equation is switched to the k-ε model equation.

If the turbulent kinetic energy k and the turbulent frequency ω are known, the turbulent viscosity $\nu_t(\vec{x})$ can be expressed as:

$$\nu_t(\vec{x})=\frac{a_1k}{\max(a_1\omega,\Omega F_2)} \tag{2.55}$$

$$F_2=\tanh\{[\max\left(\frac{2\sqrt{k}}{C_\mu\omega y},\frac{500\nu}{y^2\omega}\right)]^2\} \tag{2.56}$$

According to the above expressions, the turbulent viscosity at different positions can be obtained. The first term in the denominator corresponds to the expression about $\nu_t(\vec{x})$ of the traditional form of two-equation model:

$$\nu_t(\vec{x}) \sim \frac{k^2}{\varepsilon} \text{ 或 } \nu_t(\vec{x}) \sim \frac{k}{\omega} \quad \omega \equiv \frac{\varepsilon}{k} \tag{2.57}$$

The second term in the denominator modifies $\nu_t(\vec{x})$ based on some relation of shear stress within the boundary layer to avoid overestimating its value in the boundary layers with inverse pressure gradients. SST hence the name.

It can be seen that after introducing the transport equations and the corresponding turbulent viscosity, the RANS equations based on the Boussinesq assumption are combined with the above transport equations to make the system of equations closed, and those equations can be solved according to the previous discretization method.

Finally, it should be noted that the above transport equations contain some empirical coefficients, such as C_μ, σ_k, σ_ω, etc. Some coefficients are derived from the experimental facts and theory for some specific turbulent flows, for example, the value of C_μ is derived from simple shear turbulence. In addition, since the SST k-ω turbulence model considers both the k-ε model and the k-ω model, the empirical coefficients corresponding to each model need to be given according to the specific calculation condition and spatial location. The following table gives the values of empirical coefficients in the transport equations:

Table 2.1 Empirical Coefficients Used in SST k-ω Turbulence Model

C_μ	σ_{k1}	σ_{k2}	$\sigma_{\omega1}$	$\sigma_{\omega2}$
0.09	0.85	1	0.5	0.856
β_1	β_2	γ_1	γ_2	a_1
0.075	0.0828	0.56	0.44	0.31

2.5 Chapter Summary

The analysis of the flow field around the airfoil is the key work in the study of icing. This chapter discusses in detail how to calculate the flow field around the airfoil from the perspectives of governing equations, discrete schemes, numerical calculation, and turbulence model selection. The governing equations adopt the complete set of N-S equations, and the

expressions in the form of conservative differential and conservative integral are given; after discretizing the flow field and governing equations by finite volume method, the discrete schemes adopted by convection term, diffusion term and gradient term are respectively given: among them, the convection term adopts the second-order upwind scheme, the diffusion term adopts the central difference scheme, the gradient term adopts the weighted least squares cell-based gradient method, and the pressure interpolation adopts the second-order scheme; then the definite conditions are applied, and the discrete equation system is calculated by the pressure-velocity coupled algorithm; In addition, this study takes into account the possibility of turbulent flow after airfoil icing, and uses $SST\ k$-ω turbulence model to describe the effect of turbulence.

So far, the analysis of the flow field around the airfoil is completed, and the third chapter will focus on the analysis of the water droplet trajectory and the airfoil icing behavior.

Chapter 3 Analysis of Supercooled Water Droplets Trajectory and Airfoil Icing Behavior

3.1 Foreword

The calculation of the motion trajectory of the supercooled water droplets is based on the obtained flow field around the airfoil. By analyzing the force applied on the supercooled water droplets and establishing the relevant dynamic equations, the motion trajectory of the supercooled water droplets can be numerically solved, and then the mass of water droplets intercepted by the airfoil per unit time can be determined. At present, the two mainstream calculation methods are Lagrangian method and Euler method, which are also the basis for the development of water droplet motion trajectory codes. Among them, the LEWICE software developed by NASA solves the trajectory of water droplets with Lagrangian method as the framework; while the FENSAP-ICE software developed by McGill University in Canada solves the trajectory of water droplets with the Euler method as the framework. This chapter will analyze the above two methods separately.

After the supercooled water droplets are intercepted by the airfoil, the amount of ice accretion will be calculated according to the mass and heat transfer behavior within the surface control volume of the icing airfoil. Most of the ice accretion calculation codes were developed based on the Messinger model, including FENSAP-ICE used in this study. Therefore, this chapter analyzes the improved Messinger model of FENSAP-ICE.

3.2 Analysis of Supercooled Water Droplets Trajectory

Before analyzing force and motion trajectory of supercooled water droplets, it is necessary to introduce some relevant assumptions in order to simplify the problem at hand:

1) The water droplets in the airflow have perfect spherical shape, and they are uniformly distributed; during movement, the droplets will not be deformed or broken;

2) The volume fraction occupied by water droplets in the air is very small, so it is unlikely that the water droplets will collide and fuse, and these interactions can be ignored;

3) During the movement of the water droplets, there is no mass and heat exchange with the air, and the physical properties including the density of the water droplets remain unchanged;

4) Since the size of the water droplets is small and the proportion is very low, it can be

considered that the movement of the water droplets does not affect the numerical solution of the airflow field;

5) Regardless of the influence of air turbulence on supercooled water droplets, the force exerted on supercooled water droplets only includes inertial force, air drag, air buoyancy and gravity;

6) The supercooled water droplets velocity far away from airfoil is the same as the free flow velocity of the air.

For this study, the above hypotheses about supercooled water droplets are reasonable and valid. Next, the governing equations for the motion of supercooled water droplets are derived by using Lagrangian method and Euler method respectively.

3.2.1 Description of Lagrangian Method

In order to track the motion of each supercooled water droplet in the flow field, it is necessary to establish the force balance equation of supercooled water droplets according to Newton's second law:

$$\overrightarrow{F_d} + \overrightarrow{F_b} + \overrightarrow{F_g} - m_w \frac{d\overrightarrow{v_w}}{dt} = 0 \tag{3.1}$$

In the above equation, $\overrightarrow{F_d}$ represents the air drag; $\overrightarrow{F_b}$ represents air buoyancy; $\overrightarrow{F_g}$ represents the gravity of the water droplet; $-m_w \frac{d\overrightarrow{v_w}}{dt}$ represents the inertial foce. For the aerodynamic force and the gravity, the corresponding calculation formulas are as follows:

$$\overrightarrow{F_d} = \frac{1}{2}\rho(\vec{v} - \overrightarrow{v_w})^2 A_w C_D \tag{3.2}$$

$$\overrightarrow{F_b} = -\frac{\rho}{\rho_w} m_w \vec{g} \tag{3.3}$$

$$\overrightarrow{F_g} = m_w \vec{g} \tag{3.4}$$

In above formulas, ρ represents the air density, ρ_w represents the density of supercooled water droplets, generally speaking, $\rho_w \gg \rho$; $\vec{v}$ represents the airflow velocity, $\overrightarrow{v_w}$ represents the velocity of the water droplet; A_w represents the projected area of the water droplet; C_D represents the drag coefficient of the water droplet; m_w represents the mass of a

single supercooled droplet, and $\vec{g}$ represents the gravity acceleration.

Based on the assumption that the water droplets remain spherical, the formulas for A_w and m_w are given:

$$A_w = \frac{1}{4}\pi d_w^2 \tag{3.5}$$

$$m_w = \frac{1}{6}\rho_w \pi d_w^3 \tag{3.6}$$

d_w represents the equivalent diameter of a spherical water droplet. Substituting the above expression into equation (3.1):

$$\frac{d\overrightarrow{v_w}}{dt} = \frac{3}{4}\frac{\rho}{\rho_w}\frac{1}{d_w}(\vec{v} - \overrightarrow{v_w})^2 C_D + \left(1 - \frac{\rho}{\rho_w}\right)\vec{g} \tag{3.7}$$

Since there is often a close relationship between the drag coefficient and the Reynolds number, in order to give the drag coefficient C_D, the water droplet Reynolds number is first defined as follows:

$$Re_w = \frac{\rho d_w |\vec{v} - \overrightarrow{v_w}|}{\mu} \tag{3.8}$$

μ represents the dynamic viscosity of air. Therefore, the above dynamic equation can be expressed as:

$$\frac{d\overrightarrow{v_w}}{dt} = \frac{3}{4}\frac{Re_w \mu |\vec{v} - \overrightarrow{v_w}| C_D}{\rho_w d_w^2} + (1 - \frac{\rho}{\rho_w})\vec{g} \tag{3.9}$$

Considering that the shape of the droplet remains spherical, the relationship between its drag coefficient and the droplet Reynolds number is given by:

$$C_D = c_1 + \frac{c_2}{Re_w} + \frac{c_3}{Re_w^2} \tag{3.10}$$

The coefficients $c1$, $c2$ and $c3$ in the formula change according to the different ranges of the water droplet Reynolds number. The reference values of these three coefficients under different conditions are as follows:

Table 3.1 Reference values of coefficients under different water droplet Reynolds numbers

Re_w	c_1	c_2	c_3
$0 < Re_w < 0.1$	0	24	0
$0.1 < Re_w < 1$	3.690	22.730	0.090
$1 < Re_w < 10$	1.222	26.167	-3.889
$10 < Re_w < 100$	0.617	46.500	-116.670
$100 < Re_w < 1000$	0.364	98.330	-2778

As can be seen from the above table, $Re_w \ll 1$ corresponds to the peristaltic flow around spherical particles, and the drag coefficient C_D is exactly equal to $\frac{24}{Re_w}$, which meets the actual requirement.

The above dynamic equation can be further simplified under certain conditions: because the density of water droplets is much greater than that of air, the buoyancy of air on water droplets can be ignored; in addition, when the size of water droplets is very small, the air drag is much greater than the gravity of the water droplets, so the main driving term in the dynamic equation is only air drag. It is generally considered that when the equivalent diameter d_w of a water droplet is less than $50\mu m$, the effect of gravity can be ignored.

The dynamic equation of the supercooled water droplet describes the relationship between the force and the motion acceleration of the water droplet. In addition, it is necessary to introduce the initial conditions and the kinematic equation, and then establish a complete set of equations for the supercooled water droplet:

$$\frac{d\overrightarrow{x_w}}{dt} = \overrightarrow{v_w} \tag{3.11}$$

$$\frac{d\overrightarrow{v_w}}{dt} = \frac{3}{4}\frac{Re_w \mu |\vec{v} - \overrightarrow{v_w}| C_D}{\rho_w d_w^2} \tag{3.12}$$

$$\overrightarrow{x_w}(t = 0) = \overrightarrow{x_{w0}} \tag{3.13}$$

$$\overrightarrow{v_w}(t=0) = \overrightarrow{v_{w0}} \tag{3.14}$$

The above equations can be regarded as nonlinear ordinary differential equations. The classical numerical calculation method is to use the fourth-order Runge-Kutta method, and the problem is solved step by step in discrete time steps, finally the position and velocity of the supercooled water droplet during the movement can be obtained. In addition, the calculation of this equation system depends on the airflow velocity distribution calculated by the flow field around the airfoil, so it is necessary to analyze the flow field around the airfoil first.

When the velocity distribution of the airflow is known, the airflow velocity at the location of the water droplet needs to be determined. Therefore it can be first judged whether the water droplet is located in a discrete control volume. Taking the following figure as an example:

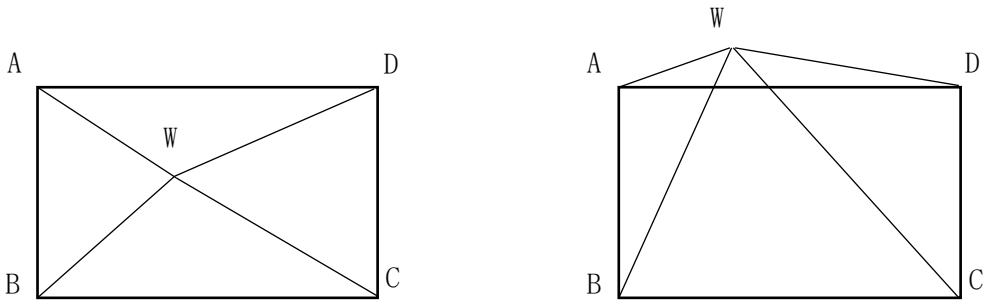

Figure 3.1 Determination of the relative position of water droplet and discrete control volume

The W point in the figure marks the position of the water droplet, the left figure indicates that the water droplet is inside the quadrilateral control volume; the right figure indicates that the water droplet is outside the quadrilateral control volume. There are many methods for judging the relative position of point W. For example, it can be determined according to the sum of the areas[42]: if the area enclosed by point W and the vertices of each control volume is equal to the area of the quadrilateral control volume, then point W is included in the control volume; otherwise the W point is outside the control volume. The formula is expressed as:

$$|S_{WAB} + S_{WBC} + S_{WCD} + S_{WDA} - S_{ABCD}| < \delta \tag{3.15}$$

δ can be a very small value, on the order of 10^{-10}; this setting mainly considers the numerical precision of the calculation. If the area enclosed by the W point and the control

volume nodes satisfies the above formula, then the supercooled water droplet is just located at the W point position within the control volume, and the airflow velocity $\vec{v}$ at this position can be obtained by a custom interpolation method.

In addition to the above method, it also includes the method of drawing half-line from point W to the interface, and judging by the parity of the number of intersection points; or the method of judging by the sequence of the connection between point W and each control volume vertex, etc. All of these methods can determine the relative position of the supercooled water droplet with respect to control volume at any time, and then determine the airflow velocity $\vec{v}$, so as to solve the system equations of motion.

After the trajectory of the supercooled water droplet is determined, the position of the water droplet impinging on the airfoil surface can be calculated, and then the distribution of the impinging water droplet on the airfoil surface can be obtained, which is usually expressed by the local water droplet collection efficiency β. The collection efficiency reflects the flux fraction of freestream droplets that can impact on a given airfoil location. Typically, β has its peak value near the leading edge stagnation point; while it tends to be 0 at the rearward position of the upper and lower surface.

The local droplet collection efficiency β is defined as follows:

$$\beta = \frac{dy_0}{ds} \tag{3.16}$$

In the formula, dy_0 represents the unit span area that a certain mass of water droplets in the free flow pass through; ds represents the unit span area covered by the impact region of the given mass of water droplets on the airfoil; and β is the ratio between the two. In order to have a more intuitive understanding of the local water droplet collection efficiency, the corresponding schematic diagram is as follows:

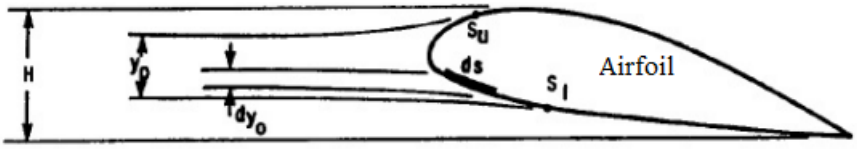

Figure 3.2 Schematic diagram of the definition of water droplet collection efficiency

The above figure clearly explains the definition formula of the local water droplet

collection efficiency β. In addition, the total collection efficiency E of water droplets can also be defined according to the above figure:

$$E = \frac{y_0}{H} \tag{3.17}$$

In the formula, y_0 represents the total amount of water in the free flow that can collide with the airfoil, and H represents the forward projection height of the airfoil. The total collection efficiency E reflects the ratio of the actual total freestream water droplets that can be collected by the airfoil to the maximum freestream water droplets that can be collected by the airfoil. In practice, the amount of water collected on the airfoil surface is defined by S_u and S_l in the figure, where S_u represents the upper surface impact limit, and S_l represents the lower surface impact limit. Beyond the upper and lower limit, the supercooled water droplets are no longer intercepted by the airfoil and will continue to flow downstream.

When the upper and lower limit trajectories of the water droplets are determined, and the local collection efficiency β is obtained by using its definition formula within the limit, the distribution map of β can be drawn, and the mass of water droplets colliding with the surface control volume per unit time $\dot{m}_{imp}$ can be expressed as:

$$\dot{m}_{imp} = LWC \cdot U_\infty \cdot \beta \cdot S_{imp} \tag{3.18}$$

LWC in the formula is the liquid water concentration, and its unit is usually expressed as g/m^3. Its physical meaning is the mass of liquid water contained in a unit volume of supercooled cloud layer, which is usually used as an important indicator to predict the development of ice accretion, and the ice shape, ice accretion rate, etc. are often affected by LWC; U_∞ is the freestream airflow velocity; β is the local water droplet collection efficiency described above; S_{imp} is the normal projection area of the interface when the supercooled water droplet collides with the surface control volume. $U_\infty \cdot \beta \cdot S_{imp}$ in the above formula can be regarded as the freestream volume flow rate of the water droplets that can be successfully intercepted by the airfoil.

$\dot{m}_{imp}$ will be used for the mass conservation condition in the subsequent icing model to solve the ice accretion mass $\dot{m}_{ice}$ per unit time, so it is necessary to determine the water droplets trajectory and collection efficiency β. It is more intuitive to solve the motion of water

droplets by the above Lagrangian method, and the motion state of each supercooled water droplet particle can be obtained. At present, many calculation models use this method.

3.2.2 Description of Euler Method

Different from Lagrangian method, Euler method no longer focuses on the motion of a single supercooled water droplet, but treats the droplets as another phase, and establishes the governing equations for the water droplets phase by introducing its volume fraction α_w. By discretely solving the equations, the volume fraction α_w, velocity $\overrightarrow{v_w}$ of supercooled water droplets within each control volume can be obtained; in addition, the local water droplet collection efficiency β can also be directly calculated from the flow solution. Compared with Lagrangian method, Euler method allows to share the same mesh when calculating the flow field of air and water droplets phase, which is more suitable for dealing with more complex three-dimensional flow problems.

Before describing the water droplets phase flow field with the governing equations, first define the volume fraction α_w of water droplets: α_w represents the proportion of the volume of water droplets in the mixed fluid per unit volume. Therefore, for a given mixed fluid volume V, the volume occupied by the water droplets phase V_w can be expressed as:

$$V_w = \int_V \alpha_w \, dV \tag{3.19}$$

In general, volume fraction has the following property:

$$\sum_{i=1}^{n} \alpha_i = 1 \tag{3.20}$$

α_i represents the volume fraction of the i^{th} substance component, and the sum of the volume fractions of all components should be equal to 1. For the problem of the movement of water droplets in the airflow, the mixed fluid only contains the air phase and the water droplets phase, therefore, such a problem can be regarded as a two-phase flow problem, only α_w can describe the respective contribution of air and water droplets on the density of the mixed fluid:

$$\rho_{mix} = \alpha_w \rho_w + (1 - \alpha_w)\rho \tag{3.21}$$

ρ_{mix} is the density of the mixed fluid, $\alpha_w \rho_w$ is the effective density of water droplets,

and $(1-\alpha_w)\rho$ is the effective density of air. Since α_w considered in this study is very small, on the order of 10^{-6}, the assumption that the movement of water droplets does not affect the air flow field is valid, and the effective density of air $(1-\alpha_w)\rho$ is almost the same as the density of pure air ρ.

In the Cartesian coordinate system, the two-dimensional continuity equation and momentum equations of the supercooled water droplets phase in differential form can be written in the following form:

$$\frac{\partial \alpha_w}{\partial t}+\frac{\partial(\alpha_w u_w)}{\partial x}+\frac{\partial(\alpha_w v_w)}{\partial y}=0 \tag{3.22}$$

$$\frac{\partial(\alpha_w u_w)}{\partial t}+\frac{\partial(\alpha_w {u_w}^2)}{\partial x}+\frac{\partial(\alpha_w u_w v_w)}{\partial y}=F_{dx} \tag{3.23}$$

$$\frac{\partial(\alpha_w v_w)}{\partial t}+\frac{\partial(\alpha_w u_w v_w)}{\partial x}+\frac{\partial(\alpha_w {v_w}^2)}{\partial y}=F_{dy}+F_b+F_g \tag{3.24}$$

The above equations have the same physical principles as the N-S equations of the airflow field, and the expressions are similar. u_w in the equations represents the velocity component of supercooled water droplets in the direction of x, v_w represents the velocity component of supercooled water droplets in the direction of y; F_{dx} represents the force component of air drag in the direction of x, and F_{dy} represents the force component of air drag in the direction of y; F_b and F_g represent air buoyancy and droplets gravity respectively.

The force applied in the governing equations is calculated by the following formulas:

$$\begin{aligned} F_{dx} &= \frac{1}{2}\rho\sqrt{(u-u_w)^2+(v-v_w)^2}(u-u_w)C_D\cdot\alpha_w\frac{\frac{1}{4}\pi d^2}{\frac{1}{6}\pi d^3} \\ &= \frac{3}{4}\frac{\alpha_w\rho|\vec{v}-\overrightarrow{v_w}|(u-u_w)C_D}{d} \end{aligned} \tag{3.25}$$

$$F_{dy}=\frac{3}{4}\frac{\alpha_w\rho|\vec{v}-\overrightarrow{v_w}|(v-v_w)C_D}{d} \tag{3.26}$$

$$F_b + F_g = \left(1 - \frac{\rho}{\rho_w}\right)\alpha_w \rho_w g = (\rho_w - \rho)\alpha_w g \tag{3.27}$$

where u and v are the velocity components of the airflow along x and y directions; d is the equivalent diameter of spherical water droplets; the drag coefficient C_D can be related to the water droplets Reynolds number Re_w, and is calculated from the coefficients given in Table (3.1); it can also be calculated using the following empirical formula:

$$C_D = \begin{cases} (\frac{24}{Re_w})(1 + 0.15Re_w^{0.687}) & Re_w \leq 1300 \\ 0.4 & Re_w > 1300 \end{cases} \tag{3.28}$$

The unknowns that need to be solved in the above governing equations for the supercooled water droplets phase include: the volume fraction of supercooled water droplets α_w, the velocity components of supercooled water droplets u_w and v_w. In order to solve the above equation system, it needs to be numerically discretized. FENSAP-ICE uses the Galerkin finite element method(GFEM) to discretize the equation system, and adds the streamline upwind Petrov-Galerkin(SUPG) formulation for stabilizing convection term.

The Galerkin finite element method aims to construct the discrete form of the above equations and obtain approximate solutions of the original partial differential equations. Considering an unknown quantity of the system of equations, such as $\alpha_w u_w$, the following equation is satisfied in the supercooled water droplets flow field V:

$$\frac{\partial(\alpha_w u_w)}{\partial t} + \vec{\nabla} \cdot \vec{\Gamma} = F_{dx} \tag{3.29}$$

$\vec{\Gamma}$ in the equation now corresponds to the flux of $\alpha_w u_w$. The equation is weighted with the trial function φ and integrated over the domain V to get the integral equation:

$$\int_V \frac{\partial(\alpha_w u_w)}{\partial t}\varphi dV + \int_V (\vec{\nabla} \cdot \vec{\Gamma})\,\varphi dV = \int_V F_{dx}\,\varphi dV \tag{3.30}$$

Using the divergence theorem to process the second term of the equation, we can get:

$$\int_V (\vec{\nabla} \cdot \vec{\Gamma})\, \varphi dV = -\int_V \vec{\Gamma} \cdot \vec{\nabla}\varphi dV + \int_{\partial V} (\vec{\Gamma}\varphi) \cdot \vec{n}\, dS \tag{3.31}$$

The purpose of this step is mainly to facilitate the realization of numerical solutions, so that the flux $\vec{\Gamma}$ does not have to be differentiable. Substituting the above formula into the integral equation, the weak-form formula of the finite element method can be obtained:

$$\int_V \frac{\partial(\alpha_w u_w)}{\partial t} \varphi dV - \int_V \vec{\Gamma} \cdot \vec{\nabla}\varphi dV + \int_{\partial V} \vec{\Gamma} \cdot \vec{n}\, \varphi dS = \int_V F_{dx}\, \varphi dV \tag{3.32}$$

The reason why the above formula is called a weak form formula is that it uses the trial function φ, which relaxes the requirement for the original governing equation, that is, it is no longer necessary to ensure that $\alpha_w u_w$ and its flux are clearly defined within the droplets flow field at any position, it is only necessary to ensure that the corresponding values after integration satisfy the weak-form formula; moreover, this formula allows for discontinuous first-order derivatives of the solution. Through the above steps, the original governing equations for supercooled water droplets can be solved discretely. In general, the trial function φ can have several types of choices, the most common choice is the polynomial type; in addition, if φ takes the value of 1, the above weak form formula will be transformed into the basic equation of the finite volume method.

To further discretize the weak form formula, it is necessary to approximate the quantities to be calculated, such as $\alpha_w u_w$:

$$\alpha_w u_w = \sum_j (\alpha_w u_w)_j\, \psi_j(\vec{x}) \tag{3.33}$$

$(\alpha_w u_w)_j$ in the formula is the physical quantity at the node of the calculation grid, $\psi_j(\vec{x})$ is a selected set of basis functions, which are related to the spatial position. In the Galerkin finite element method, the trial function and the basis function use the same function, so the following will continue to use φ to represent the trial function and the basis function. Substituting the above linear combination into the weak form formula corresponding to each trial function φ_i:

$$\int_V \sum_j \varphi_j \frac{\partial(\alpha_w u_w)_j}{\partial t} \varphi_i dV - \int_V \sum_j \vec{\Gamma}_j \varphi_j \cdot \vec{\nabla}\varphi_i dV + \int_{\partial V} \sum_j \vec{\Gamma}_j \varphi_j \cdot \vec{n} \varphi_i dS = \int_V F_{dx} [\sum_j (\alpha_w u_w)_j \varphi_j] \varphi_i dV \tag{3.34}$$

The unknown quantity of the above formula is transformed from the physical quantity $\alpha_w u_w$ at any point in the flow field to the physical quantity $(\alpha_w u_w)_j$ at the calculation node. In the case of known trial (basis) functions, assuming that the number of trial (basis) functions is N_t, a system of equations with a number of N_t can be represented, and the number of unknowns $(\alpha_w u_w)_j$ is also N_t, the system of equations can be solved after giving the boundary conditions and initial conditions of the flow field. The first term of the above formula is the time-related term, which can be expressed as the change of the physical quantity between the current time and the previous time with the time step by using the Euler backward difference method; if the steady flow problem is considered, this term can be neglected.

The above formula can be simplified into the form of a matrix equation system:

$$[K]\{\alpha_w u_w\} = \{b\} \tag{3.35}$$

$[K]$ can be regarded as a stiffness matrix with dimension of $N_t \times N_t$; $\{\alpha_w u_w\}$ is a discrete physical quantity vector at the computational grid nodes, with dimension of $N_t \times 1$; $\{b\}$ can be regarded as a load matrix generated by the force F_{dx}, and its dimension is $N_t \times 1$. In general, the $[K]$ matrix is a large sparse matrix.

In addition, in Galerkin finite element method, the trial (basis) function φ_i is a compact function, which means that each φ_i has values only in a small discrete interval, and remains 0 in other intervals. Such characteristics also makes finite element method different from Rayleigh-Ritz method, which is based on a globally defined trial function. If φ_i is expressed in the form of polynomial, the coefficient of each polynomial term can be determined by using certain interpolation method after considering the values on the grid nodes and the corresponding boundary conditions.

In addition to using the above-mentioned Galerkin finite element method to discretely solve the governing equations, FENSAP-ICE also added additional streamline upwind term, which mainly used the first-order derivative of the basis function ψ to correct the trial function φ, so that an artificial dissipation along the streamline direction is introduced; at this time, the

trial function φ is different from the basis function ψ in order to stabilize the convection term in the governing equation and suppress the numerical oscillation that may occur during the numerical calculation.

The boundary conditions of the droplets flow field include far-field boundary conditions and wall boundary conditions. For far-field boundary conditions, the volume fraction of the droplets and the droplets velocity can be determined by the following equations:

$$\alpha_{w\infty} = \frac{LWC_{\infty}}{\rho_w} \tag{3.36}$$

$$\overrightarrow{v_{w\infty}} = \vec{v}_{\infty} \tag{3.37}$$

In the formula, LWC_{∞} is the liquid water concentration in the freestream; $\vec{v}_{\infty}$ is the freestream velocity of air, which is consistent with the assumption made at the beginning of this chapter.

For the wall boundary conditions, the impinging surface can be regarded as one-way outlet for water droplets, which means that water droplets can only flow out of the computational domain. Because when hitting the airfoil surface, the water droplets either freeze immediately or attach to the surface in the form of water film and do not return to the computational domain again. If the velocity of the supercooled water droplets hitting the surface is denoted as $\overrightarrow{v_{ws}}$, and the outer normal vector of the surface is denoted as $\vec{n}$, then when $\overrightarrow{v_{ws}} \cdot \vec{n} < 0$, the droplets collide with the surface, the volume fraction and velocity of droplets on the surface can be obtained by the above calculation method; When $\overrightarrow{v_{ws}} \cdot \vec{n} > 0$, the one-way outlet condition is not satisfied, and the volume fraction of water droplets here is set to 0, indicating that the water droplets did not collide with the surface.

After numerically solving the governing equations of the supercooled water droplets flow field under Euler method, the local droplets collection efficiency β can be directly obtained according to the calculation results. The volume fraction of the water droplets on the impact surface is denoted as α, the normal velocity magnitude $|\overrightarrow{v_{ws}} \cdot \vec{n}|$ is denoted as U_{wn}; the volume fraction of the water droplets in the freestream is denoted as $\alpha_{w\infty}$, the velocity magnitude is denoted as $U_{w\infty}$, then the local collection efficiency β can be obtained by the following formula:

$$\beta = \frac{\alpha}{\alpha_{w\infty}} \frac{U_{wn}}{U_{w\infty}} \tag{3.38}$$

After obtaining the local water droplet collection efficiency β using the above Euler method, the subsequent ice accretion calculation can be carried out. In this study, FENSAP-ICE was used to complete the calculation of airfoil icing under a series of test conditions, including the solution of water droplets motion. Figures 3.3 and 3.4 are collection efficiency distribution diagram and liquid water concentration distribution diagram respectively, selecting the NACA0012 airfoil with chord length of $1m$, and flight speed is $65m/s$, flight angle of attack is 4°, freestream pressure is 101325Pa, static temperature is −15°C, cloud LWC is $1\ g/m^3$, droplets MVD is $25\mu m$, freezing step is $120s$, and total freezing time is $360s$.

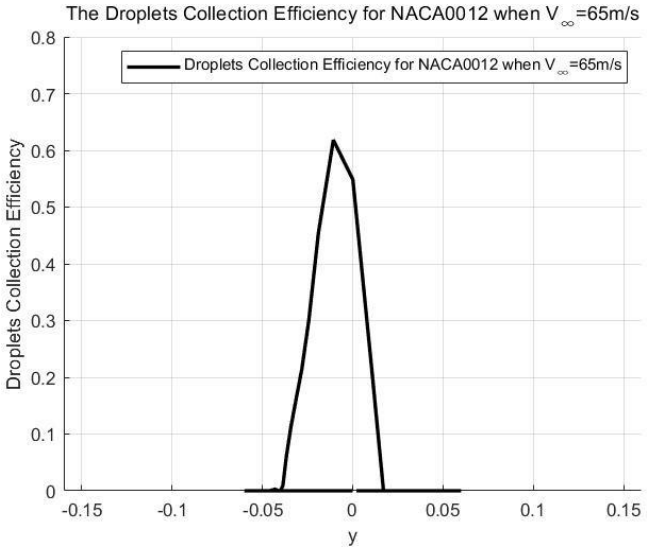

Figure 3.3 Droplet collection efficiency distribution under given test condition of NACA0012 airfoil

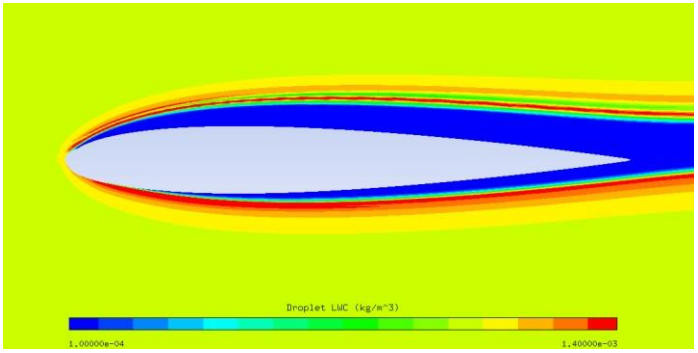

Figure 3.4 Liquid water concentration distribution under given test condition of NACA0012 airfoil

The water droplet collection efficiency distribution diagram generally uses the abscissa to represent the arc length from the surface point on the airfoil to the leading edge point, and the ordinate represents the local water droplet collection efficiency β. It can be seen from Figure 3.3 that the distribution of the collection efficiency β on the upper and lower surface of the NACA0012 airfoil is not asymmetric under this test condition. Since the flight angle of attack is 4°, the incoming water droplets are more likely to collide with the lower airfoil surface in this case. Figure 3.4 reflects the distribution of liquid water concentration, with the dark blue area indicating that the volume fraction of water droplets is 0.

3.3 Analysis of Airfoil Icing Behavior

After analyzing the flow field around the airfoil and the trajectory of water droplets, the ice accretion behavior on the airfoil surface can be described by establishing an improved Messinger model and transforming it into a partial differential equation system composed of conservation equations. In FENSAP-ICE, the physical quantities transferred to the ice accretion calculation module ICE3D include[43]: 1) convective heat flux $\dot{Q}_h$ and wall shear force τ_w obtained by solving the air flow field; 2) local water droplet collection efficiency β and droplets impact speed $\overrightarrow{v_{wd}}$ obtained by solving the water droplets flow field. Through the transfer of the above physical quantities, the improved Messinger model can be completely constructed.

The airfoil icing problem is usually caused by supercooled water droplets hitting the airfoil to form water film and gradually freezing. The freezing process is accompanied by the conversion and transfer of mass and heat. For convenience, first define surface control volume (also called surface mesh) on the icing airfoil. The surface control volume refers to the control volume including the interface of the air with the initial airfoil or icing airfoil, so the lower boundary of the volume is always kept as the clean airfoil surface or the icing surface. Performing mass and energy conservation analyses for each surface control volume can help to understand the physical processes that occur when ice accretion forms.

Before the analysis, the assumptions of the original Messinger model for the icing problem are given first, and on the basis of the original assumptions, the improvements made by FENSAP-ICE are illustrated. The main assumptions of the Messinger model include: 1) Only the water that has not been frozen within the surface control volume is allowed to run back, and all water flows to the downstream mesh cells along the airflow direction, so the runback water that is still liquid will not stay in the current mesh or fall off the surface; 2) The temperature at which the runback occurs corresponds to the freezing point of the water; 3) The thermal radiation is ignored due to the low

temperature when the airfoil freezes; 4) The heat conduction between the runback water and the surface is ignored. The above Messinger assumptions are relatively simple. By discarding some flow and heat transfer details, the icing problem can be simplified, but it will reduce the accuracy of ice shape prediction. To this end, FENSAP-ICE mainly adds some details of the water film flow in the surface control volume, considering the driving forces such as airflow shear and pressure gradient when the water film flows, so that the water film flow, as well as its mass conversion and transfer are more clearly described.

Next, the mass conservation during ice accretion is analyzed:

For a flowing water film system, the mass change per unit area of the water film system per unit time is caused by the following factors: 1) the collision of supercooled water droplets with the airfoil brings a part of the mass; 2) the evaporation of liquid water and ice sublimation takes away part of the mass; 3) the freezing of water takes away part of the mass. The formula can be expressed as:

$$\frac{Dm_f}{Dt} = \dot{m}_{imp} - \dot{m}_{es} - \dot{m}_{ice} \tag{3.39}$$

In the right-hand side of the equation, $\dot{m}_{imp}$ is the mass of supercooled water droplets flowing into the system, which can be regarded as the source term of the water film mass; $\dot{m}_{es}$ is the mass loss caused by water evaporation or ice sublimation to form water vapor, and $\dot{m}_{ice}$ is the mass of water freezing, $\dot{m}_{es}$ and $\dot{m}_{ice}$ can be regarded as the sink term of the water film mass; the left-hand side of the equation represents the mass change per unit area of the water film system per unit time during the flow, and can also be written in the following form:

$$\frac{Dm_f}{Dt} = \frac{D(\rho_w h_f)}{Dt} = \rho_w \frac{Dh_f}{Dt} = \rho_w [\frac{\partial h_f}{\partial t} + (\bar{u}_w \cdot \vec{\nabla}) h_f] \tag{3.40}$$

h_f represents the thickness of the water film, and $\bar{u}_w$ represents the average flow velocity of the water film along the thickness direction. Since the water film flow is an incompressible flow, the density ρ_w of water is regarded as a constant. $\bar{u}_w$ is represented by the following formula:

$$\bar{u}_w(\vec{x}_s) = \frac{1}{h_f} \int_0^{h_f} \vec{u}_w(\vec{x}_s, y) dy \tag{3.41}$$

$\vec{x}_s$ is the surface coordinates vector and y is the coordinate in the thickness direction of the water film. $\vec{u}_w(\vec{x}_s, y)$ is the flow velocity of liquid water in the water film, which can be different along the surface direction and the water film thickness direction. In addition, due to the incompressibility of water flow, the continuity equation can be expressed as:

$$\vec{\nabla} \cdot \vec{u}_w = 0 \tag{3.42}$$

Therefore, the mass conservation equation per unit area of the surface control volume per unit time is finally established:

$$\rho_w \left[\frac{\partial h_f}{\partial t} + \vec{\nabla} \cdot \left(\bar{u}_w h_f \right) \right] = \dot{m}_{imp} - \dot{m}_{es} - \dot{m}_{ice} \tag{3.43}$$

$\dot{m}_{imp}$ and $\dot{m}_{es}$ can be calculated by the following formulas:

$$\dot{m}_{imp} = LWC \cdot U_\infty \cdot \beta \tag{3.44}$$

$$\dot{m}_{es} = -0.696 \frac{h_c}{C_p} \frac{p_{v\infty} - p_{vs}}{p_m} \tag{3.45}$$

In the calculation formula of evaporation and sublimation mass flow, h_c is the convective heat transfer coefficient of the surface control volume, C_p is the constant pressure specific heat of air, $p_{v\infty}$ is the saturated vapor pressure of water corresponding to the free flow temperature, and p_{vs} is the saturated vapor pressure of water corresponding to the surface temperature, p_m is the mean value of the pressure on the airfoil surface and the pressure in the free flow. The above calculation formula of $\dot{m}_{es}$ is one of the empirical formulas, and there are other similar expression forms, which will not be described here.

The water film thickness h_f and the ice accretion rate $\dot{m}_{ice}$ in the mass conservation equation are the quantities to be solved; while the water film flow velocity $\vec{u}_w(\vec{x}_s, y)$ and the average velocity along the thickness direction $\bar{u}_w(\vec{x}_s)$ are determined according to the driving force applied on the water flow. Generally speaking, the water film on the icing surface is very thin, less than 10μm, so after considering that the water film velocity at the surface is 0, the velocity profile of the water film subjected to the airflow shear force can be simplified by the

linear model:

$$\vec{u}_{wsh}(\vec{x}_s, y) = \frac{\tau_w}{\mu_w} y \tag{3.46}$$

In this model, τ_w is the wall shear force from the airflow, and is also the main driving force for the water film far from the stagnation point, which can be directly obtained from the numerical solutions of the CFD solver; μ_w is the dynamic viscosity coefficient of water; y is the distance from the wall along the thickness direction. If the driving effect of the pressure gradient is also considered, the complete water film flow velocity is expressed as follows:

$$\vec{u}_w(\vec{x}_s, y) = (\frac{\tau_w}{\mu_w} - \frac{h_f}{\mu_w}\frac{dp}{ds})y \tag{3.47}$$

The second term on the right-hand side of the equation is the contribution of the pressure gradient, where s represents the curve distance between the surface position where the velocity to be obtained and the stagnation point. In the vicinity of the stagnation point or separation point, the influence of the pressure gradient is relatively large. In the two-dimensional case, the dimensionless pressure gradient at the stagnation point is defined as:

$$-\frac{s}{\rho u_e^2}\frac{dp}{ds} = 1 \tag{3.48}$$

According to the above formula, the water film flow velocity $\vec{u}_w(\vec{x}_s, y)$ can be determined; if only the airflow shear force is considered, the mean value along the thickness direction $\bar{u}_w(\vec{x}_s)$ is expressed as:

$$\bar{u}_w(\vec{x}_s) = \frac{1}{h_f}\int_0^{h_f} \vec{u}_w(\vec{x}_s, y)dy = \frac{h_f \tau_w}{2\mu_w} \tag{3.49}$$

So far, the analysis of mass conservation during ice accretion has been completed. The quantities to be solved include two unknowns, h_f and $\dot{m}_{ice}$. Next, energy conservation during ice accretion is analyzed, and then the calculation method of the unknowns is explained.

When the water film system is flowing, its enthalpy value will also change, which is mainly

caused by different types of heat transfer. The heat transfer per unit area per unit time includes: 1) heat increase caused by the impact of supercooled water droplets $\dot{Q}_{imp}$; 2) heat loss caused by the liquid water evaporation and the ice sublimation $\dot{Q}_{es}$; 3) heat increase caused by water freezing $\dot{Q}_L$; 4) heat loss caused by ice sensible cooling $\dot{Q}_{si}$; 5) heat loss caused by thermal radiation $\dot{Q}_r$; 6) heat loss caused by the convection heat transfer between water film and air $\dot{Q}_{hc}$; 7) The heat increase caused by the aerodynamic heating of air $\dot{Q}_a$. The energy conservation of water film system can be expressed by the following equation:

$$\frac{DE_f}{Dt} = \dot{Q}_{imp} - \dot{Q}_{es} + \dot{Q}_L - \dot{Q}_{si} - \dot{Q}_r - \dot{Q}_{hc} + \dot{Q}_a \tag{3.50}$$

The enthalpy change rate of the water film system per unit area can be written as:

$$\begin{aligned} \frac{DE_f}{Dt} &= \frac{D\left(\rho_w h_f e_f\right)}{Dt} = \rho_w \frac{D\left(h_f e_f\right)}{Dt} \\ &= \rho_w [\frac{\partial\left(h_f C_{pw} \tilde{T}_s\right)}{\partial t} + (\bar{u}_w \cdot \vec{\nabla})(h_f C_{pw} \tilde{T}_s)] \end{aligned} \tag{3.51}$$

In the formula, e_f is the enthalpy of the water film per unit mass, C_{pw} is the constant pressure specific heat of water, $\tilde{T}_s$ is the temperature of icing surface, and "~" indicates that the temperature is expressed in degrees Celsius(°C). Combined with the continuity equation for incompressible flow, the equation is organized as:

$$\frac{DE_f}{Dt} = \rho_w [\frac{\partial\left(h_f C_{pw} \tilde{T}_s\right)}{\partial t} + \vec{\nabla} \cdot (\bar{u}_w h_f C_{pw} \tilde{T}_s)] \tag{3.52}$$

The first term $\dot{Q}_{imp}$ on the right-hand side of the energy conservation equation includes the sensible heat and kinetic energy of the impinging water droplets:

$$\dot{Q}_{imp} = \left(C_{pw}\tilde{T}_{w\infty} + \frac{|\overrightarrow{v_{ws}}|^2}{2}\right)\dot{m}_{imp} = \left(C_{pw}\tilde{T}_{w\infty} + \frac{|\overrightarrow{v_{ws}}|^2}{2}\right) \cdot LWC \cdot U_\infty \cdot \beta \tag{3.53}$$

$\tilde{T}_{w\infty}$ is the temperature in Celsius of the water droplets in the freestream, and $|\overrightarrow{v_{ws}}|$ is the velocity magnitude of the droplets when hitting on the surface. The other terms on the right-

hand side of the energy conservation equation are written in turn:

$$\dot{Q}_{es} = 0.5(L_{eva} + L_{subl})\dot{m}_{es} \tag{3.54}$$

$$\dot{Q}_L = L_{fus}\dot{m}_{ice} \tag{3.55}$$

$$\dot{Q}_{si} = C_{pice}\tilde{T}_s\dot{m}_{ice} \tag{3.56}$$

$$\dot{Q}_r = \varepsilon_{emi}\sigma_{bol}(T_s^4 - T_\infty^4) \tag{3.57}$$

$$\dot{Q}_{hc} = h_c(T_s - T_\infty) \tag{3.58}$$

$$\dot{Q}_a = h_c r\frac{U_\infty^2}{2C_p} \tag{3.59}$$

where L_{eva} is the evaporation latent heat per unit mass of water, L_{subl} is the sublimation latent heat per unit mass of ice, L_{fus} is the freezing latent heat(or fusing latent heat of ice) per unit mass of water, C_{pice} is the constant pressure specific heat of ice, ε_{emi} is the surface radiation rate, σ_{bol} is the Boltzmann constant, T_s is the icing surface temperature expressed in Kelvin(K), T_∞ is the free flow temperature, and r is the recovery coefficient. These parameters actually represent physical properties of air, water, ice, etc.(e.g. L_{eva}), as well as flow field properties specified by the user (e.g. T_∞). The following table gives the reference values of parameters related to physical properties:

Table 3.2 Reference values of parameters related to physical properties

$C_p(J\cdot kg^{-1}\cdot K^{-1})$	$C_{pw}(J\cdot kg^{-1}\cdot ℃^{-1})$	$C_{pice}(J\cdot kg^{-1}\cdot ℃^{-1})$
1006.43	4200	2060
$L_{eva}(J\cdot kg^{-1})$	$L_{subl}(J\cdot kg^{-1})$	$L_{fus}(J\cdot kg^{-1})$
2.50×10^6	2.84×10^6	3.34×10^5
ε_{emi}	$\sigma_{bol}(W\cdot m^{-2}\cdot K^{-4})$	r
0.02-0.2	5.67×10^{-8}	0.895

In addition, it is also necessary to determine the value of the convective heat transfer coefficient h_c. The way FENSAP-ICE determines h_c is: using the convective heat flux $\dot{Q}_{hc}$ previously obtained by the Fluent solver to derive the convective heat transfer coefficient h_c for ice accretion:

$$h_c = \frac{\dot{Q}_{hc}}{(T_w - T_\infty)} \tag{3.60}$$

Here T_w is the wall temperature value set by the user in the Fluent solver. Generally, before solving the flow field around the airfoil, the thermal boundary conditions of the wall need to be determined. The Fluent solver provides several settings, the main two are: 1) set the convective heat flux at the wall $\dot{Q}_{hc}$; 2) set the temperature T_w at the wall. Stefano Fornasier et al.[44] studied the above two settings respectively, and judged which setting is more suitable for the calculations under different ice accretion conditions. The results show that by setting the wall temperature $T_w = 283.15K$, the values of h_c and $\dot{Q}_{hc}$ which are consistent with the LEWICE reference values under different conditions can be obtained; however, if the first setting was used, the given value of $\dot{Q}_{hc}$ needs to be carefully selected, because too small or too large values of $\dot{Q}_{hc}$ will make h_c deviate from the actual value.

The setting of T_w here is only to obtain the convective heat flux and convective heat transfer coefficient that are consistent with the actual values; the icing surface temperature T_s during ice accretion is still a quantity to be solved, and it is necessary to solve the equations of mass conservation and energy conservation simultaneously. It is worth noting that if T_w is set to be lower than or equal to the freezing point, when the freestream temperature value T_∞ is close to T_w, the denominator of the above formula tends to 0, and a numerical error will occur, resulting in the failure of the calculation of h_c. The setting reference value of T_w in the FENSAP-ICE user manual is 281K.

In practice, the convective heat transfer coefficient h_c is relatively independent of the surface temperature distributed along the airfoil; however, the value of h_c tends to vary depending on the boundary layer thickness. Therefore, some references will establish the boundary layer energy equation and use the integral method of boundary layer to solve h_c; in addition, due to the different transition positions of the flow on the smooth surface and the rough surface, the laminar and turbulent boundary layer regions are affected, which will lead to changes in h_c. Therefore, this study also introduced the equivalent sand roughness to

simulate the effect of rough surface after icing on flow and h_c calculations.

Therefore, the value of the above h_c is actually determined by the flow field position, flow condition and the physical information contained in the boundary layer, etc., which have been determined during the calculation of the airflow field. Then, according to the above formula, the value of the convective heat flux $\dot{Q}_{hc}$ is also determined; Fluent uses the saved data of $\dot{Q}_{hc}(\vec{x})$ and $T_w - T_\infty$ to inversely obtain the value of $h_c(\vec{x})$, which is used to solve the relevant terms in the ice accretion calculation.

Finally, the energy conservation equation per unit time and unit area for the surface control volume is written in the following form:

$$\begin{aligned}&\rho_w\left[\frac{\partial\left(h_f C_{pw}\tilde{T}_s\right)}{\partial t}+\left(\vec{u}_w\cdot\vec{\nabla}\right)\left(h_f C_{pw}\tilde{T}_s\right)\right]\\&=\left(C_{pw}\tilde{T}_{w\infty}+\frac{|\overrightarrow{v_{ws}}|^2}{2}\right)\cdot LWC\cdot U_\infty\cdot\beta-0.5(L_{eva}+L_{subl})\dot{m}_{es}+L_{fus}\dot{m}_{ice}\\&-C_{pice}\tilde{T}_s\dot{m}_{ice}-\varepsilon_{emi}\sigma_{bol}(T_s^4-T_\infty^4)-h_c(T_s-T_\infty)+h_c r\frac{U_\infty^2}{2C_p}\end{aligned}\tag{3.61}$$

So far, the mass conservation equation and energy conservation equation of airfoil icing have been established. The physical quantities to be solved include: 1) Ice accretion mass $\dot{m}_{ice}$; 2) Water film thickness h_f; 3) Icing surface equilibrium temperature $\tilde{T}_s$(or T_s, only the units are different). In order to solve the above physical quantities by closing the system of equations, the following compatibility conditions are introduced:

$$h_f \geq 0 \tag{3.62}$$

$$\dot{m}_{ice} \geq 0 \tag{3.63}$$

$$h_f\tilde{T}_s \geq 0 \tag{3.64}$$

$$\dot{m}_{ice}\tilde{T}_s \leq 0 \tag{3.65}$$

These four compatibility conditions actually constrain the three physical quantities to be solved: 1) When $\tilde{T}_s > 0$℃, $\dot{m}_{ice}$ must be equal to 0 to satisfy the above conditions, indicating

that when the surface temperature is higher than the freezing point, there is no ice accumulation; 2) When $\tilde{T}_s = 0℃$, all of the above conditions can be satisfied. At this time, only $\dot{m}_{ice}$ and h_f are left as the unknowns of the ice accretion conservation equations. The equations are closed and solvable, which means that when the surface temperature is at the freezing point, the water film and ice accretion are allowed to coexist; 3) When $\tilde{T}_s < 0℃$, h_f must be equal to 0 to satisfy the compatibility condition, indicating that there is no water film, and the supercooled water droplets in the surface control volume are completely frozen.

The introduction of compatibility conditions makes the system of equations closed, and the closed system of equations can be solved by iterative method: that is, assuming that the surface equilibrium temperature $\tilde{T}_s = 0℃$ in the control volume, $\dot{m}_{ice}$ and h_f are obtained through the above equations, and it is judged whether all the compatibility conditions are satisfied. If they are satisfied, it indicates that the initial assumption is correct and the unknown quantities has been solved; if one or more of them are not satisfied, the corresponding unsatisfied condition should be found out, for example: if the calculation result h_f is a negative value, then set h_f equal to 0, and re-solve the system of equations to obtain $\dot{m}_{ice}$ and $\tilde{T}_s$ satisfying all conditions. Through the above iterative method, the airfoil icing calculation can be successfully completed.

Finally, a brief description of the equivalent sand roughness k_s used in this study is given. Generally speaking, the surface of the icing airfoil is rougher than the clean airfoil, and the influence of the roughness on the surrounding flow field and icing calculation needs to be considered; however, the formation process and detailed characterization of the roughness of the icing airfoil still require in-depth research. Therefore, the main roughness calculation model of FENSAP-ICE is the equivalent sand roughness model. The corresponding concept can be traced back to the work done by German scientist Nikuradse in the 1930s: he explored the relationship between wall roughness and drag coefficient of pipe flow with tightly packed, uniform sand particles adhered to the pipe wall. The NASA research institute later gave the following empirical formula for the equivalent roughness, which is suitable for this study:

$$k_s = \left[\frac{\frac{k_s}{c}}{\left(\frac{k_s}{c}\right)_{base}}\right]_{LWC} \cdot \left[\frac{\frac{k_s}{c}}{\left(\frac{k_s}{c}\right)_{base}}\right]_{T_\infty} \cdot \left[\frac{\frac{k_s}{c}}{\left(\frac{k_s}{c}\right)_{base}}\right]_{V_\infty} \cdot \left[\frac{\frac{k_s}{c}}{\left(\frac{k_s}{c}\right)_{base}}\right]_{MVD} \cdot \left(\frac{k_s}{c}\right)_{base} \cdot c \tag{3.66}$$

$\left(\frac{k_s}{c}\right)_{base}$ in the formula is the reference value of the ratio of roughness k to airfoil chord length c, which is 0.001177; the first four terms on the right-hand side of the formula can be

regarded as the influence coefficients of $\frac{k_s}{c}$ under different weather and flight conditions, which can be obtained by the following calculation formulas:

$$\left[\frac{\frac{k_s}{c}}{\left(\frac{k_s}{c}\right)_{base}}\right]_{LWC} = 0.5714 + 0.2457 \cdot LWC + 1.2571 \cdot LWC^2 \tag{3.67}$$

$$\left[\frac{\frac{k_s}{c}}{\left(\frac{k_s}{c}\right)_{base}}\right]_{T_\infty} = 0.047 \cdot T_\infty - 11.27 \tag{3.68}$$

$$\left[\frac{\frac{k_s}{c}}{\left(\frac{k_s}{c}\right)_{base}}\right]_{V_\infty} = 0.4286 + 0.0044139 \cdot V_\infty \tag{3.69}$$

$$\left[\frac{\frac{k_s}{c}}{\left(\frac{k_s}{c}\right)_{base}}\right]_{MVD} = \begin{cases} 1 & MVD \leq 20\mu m \\ 1.667 - 0.0333 \cdot MVD & MVD > 20\mu m \end{cases} \tag{3.70}$$

Using the above empirical formulas, the effect of icing surface roughness was also considered in this study. The airfoil icing behavior analysis is over, and the ice accretion shapes are given under the test condition corresponding to the water droplets trajectory diagram:

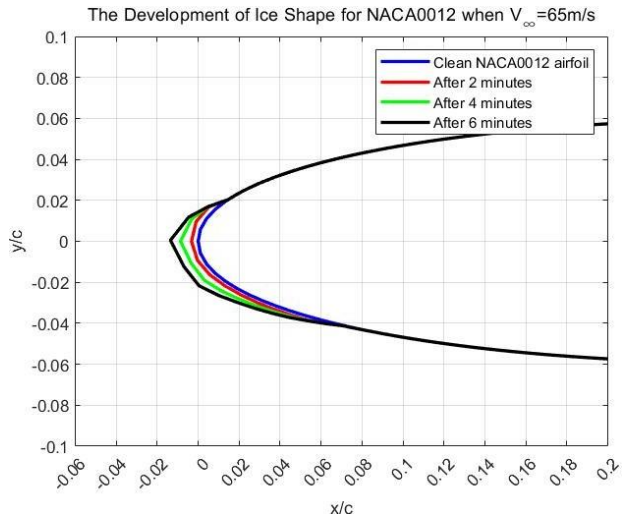

Figure 3.5 Ice accretion shape at different times under given test condition of NACA0012 airfoil

3.4 Chapter Summary

This chapter mainly analyzed the motion trajectory of supercooled water droplets and the icing behavior of airfoils. The motion trajectory of supercooled water droplets in the flow field can be described by Lagrangian method or Euler method. In this study, Euler method was used to calculate the governing equations of the water droplets phase, and the equations were numerically discretized with the Galerkin finite element method; under the given test condition, the water droplets collection efficiency and liquid water concentration distribution of the NACA0012 airfoil were drawn.

After the calculations of the air flow field and the water droplets flow field were completed, some parameters such as the wall shear force and convective heat flux obtained by the airflow, as well as the local water droplet collection efficiency and water droplet impact velocity obtained by the movement of the water droplets were transferred to the ice accretion module of FENSAP-ICE, for analyzing the airfoil surface icing behavior. Based on the improved Messinger model, the mass and energy conservation equations for the water film system and the surface control volume were established by analyzing the changes in mass and energy that occur when the water film flows. Once established, combined with certain compatibility conditions, the system of equations can be solved and the ice accretion behavior can be correctly analyzed.

All the theories, numerical discretization methods and calculation ideas related to the airfoil icing problem have been clarified. The subsequent chapters will focus on the construction and verification of the ANSYS numerical simulation platform, and the processing and analysis of simulation results.

Chapter 4 Construction and Verification of ANSYS Numerical Simulation Platform

4.1 Foreword

This chapter mainly discusses the ANSYS numerical simulation platform built in this study, and compares the numerical simulation results with the experimental and numerical reference data given in the literature to verify the correctness of the numerical simulation platform. First, the geometries of the airfoils, the selection and generation of computational grid, and the grid update technology are illustrated and presented; then, from the perspective of the airfoil icing calculation process, the relevant configurations about Fluent solver and FENSAP-ICE solver are given, and the schematic diagram of the platform after construction is shown; finally, the experimental verification conditions used in the literature are given to complete the verification work.

4.2 Airfoils Selection and Grid Generation and Update

Four airfoils from the NACA series were selected for this study, including: NACA0012 airfoil, NACA0015 airfoil, NACA4412 airfoil, and NACA23012 airfoil. The first two belong to symmetrical airfoils, and the latter two belong to the airfoils with certain cambers. In fact, the naming of this series of airfoils follows certain rules, for airfoils with four digits: the first number indicates the maximum relative camber, the second number indicates where the maximum camber occurs, and the last two numbers indicate the maximum relative thickness. Take the NACA4412 airfoil as an example: this airfoil has a maximum relative camber of 4%, which occurs at the 40% chord position; the maximum relative thickness of it is 12%. For airfoils with five digits: the first number corresponds to the designed lift coefficient, the second number corresponds to the maximum camber position, the third number corresponds to the mean camber line type, and the last two digits correspond to the maximum relative thickness. Take the NACA23012 airfoil as an example: the designed lift coefficient of this airfoil is $2 \times \frac{3}{20} = 0.3$, the maximum camber position is $3/20 = 0.15$, which is 15% of the chord length position; 0 indicates that the mean camber line type is simple type with no inflection point; the maximum relative thickness is 12%.

The coordinate points data of each airfoil can be obtained from Airfoil Tools, Profili, etc., or it can be calculated using the airfoil shape formula. The airfoil shapes drawn using Matlab are shown in the following figure:

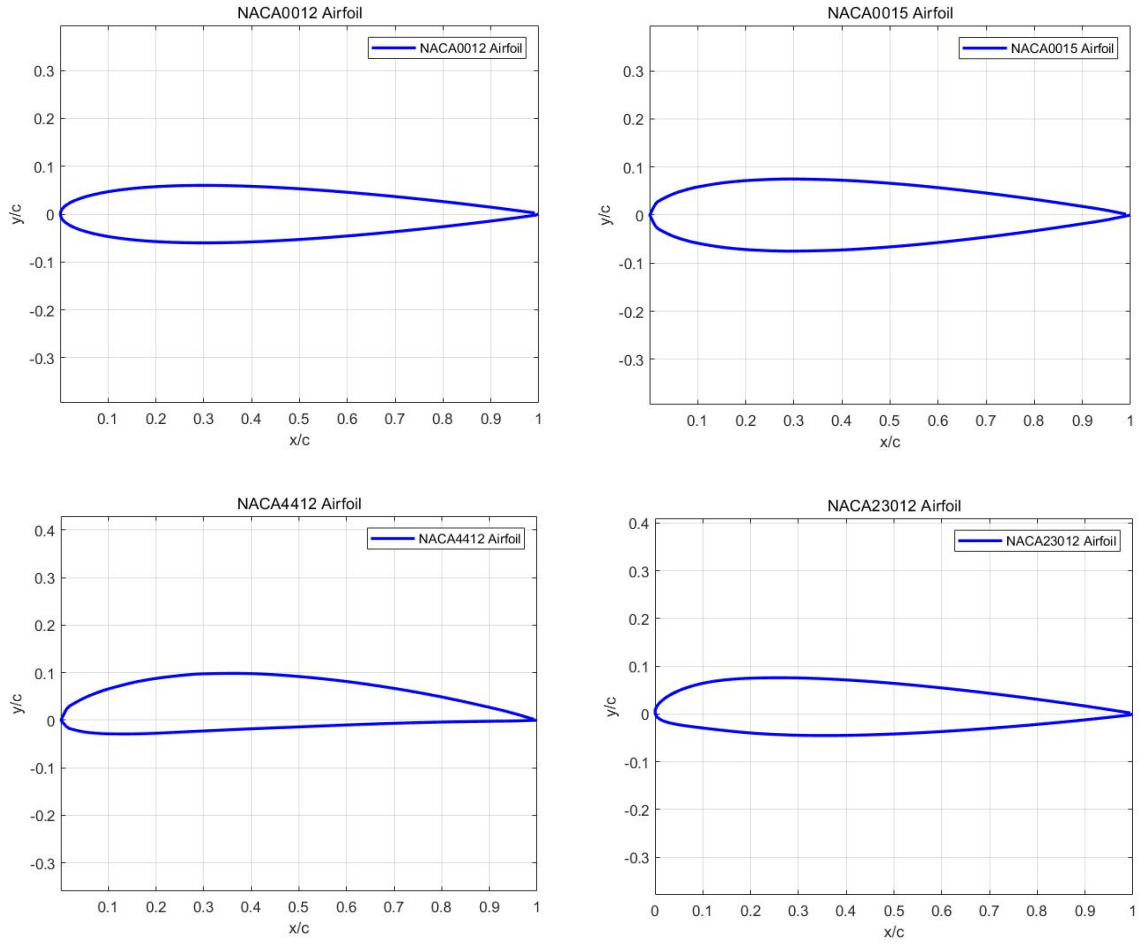

Figure 4.1 The geometries of selected NACA airfoils

After obtaining the coordinate points of the airfoils, computational grid can be generated. There are two main types of grids commonly used in CFD calculations: structured grid and unstructured grid. The structured grid has a regular topology and the grid nodes are arranged in an orderly manner. In general, the grid nodes are numbered and identified one by one in sequence. If the location and number identifier of a node are known, then the locations and identifiers of its adjacent nodes are determined accordingly. The grid distribution of the unstructured grid is irregular, the arrangement is more flexible, and the numbering of grid nodes is irregular.

Common structured grid shapes include quadrilateral in the 2D case, hexahedron in the 3D case; unstructured grid shapes include triangles in the 2D case and tetrahedrons in the 3D case. Compared with unstructured grid, structured grid generally has a higher grid quality due to its regularity and orderliness, and is not prone to distortion during deformation and update, so that the calculation accuracy can be guaranteed; in addition, for solving the same flow problem,

the number of structured grid elements is often less than that of unstructured grid elements, especially when dealing with boundary layer close to the wall, structured grid is generally used for division. Therefore, for this airfoil icing problem, the structured grid is adopted to discretize the entire flow field.

According to the overall shape of the grid, the structured grid can be further divided into C-type grid, O-type grid and so on. The C-type grid is selected for this study, and according to the idea of block division, the following grid for the flow field is generated:

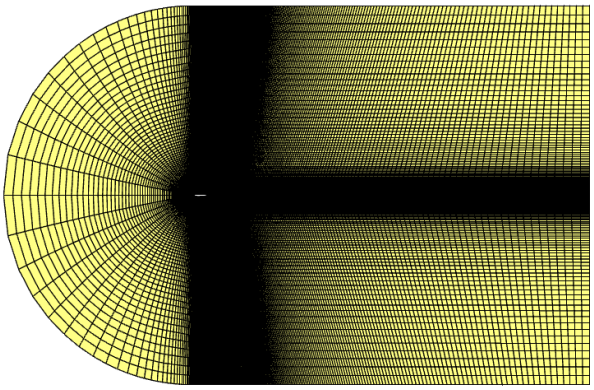

Figure 4.2 NACA0012 C-type grid global diagram

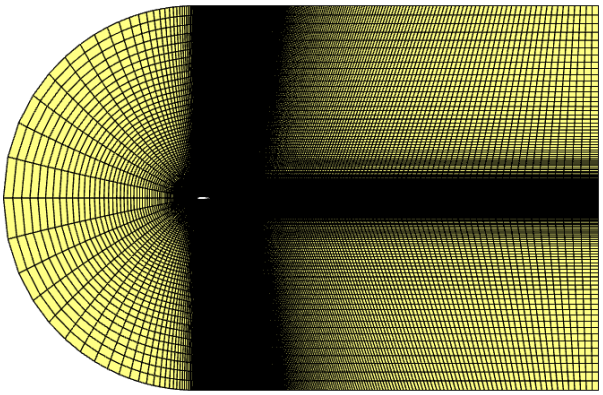

Figure 4.3 NACA0015 C-type grid global diagram

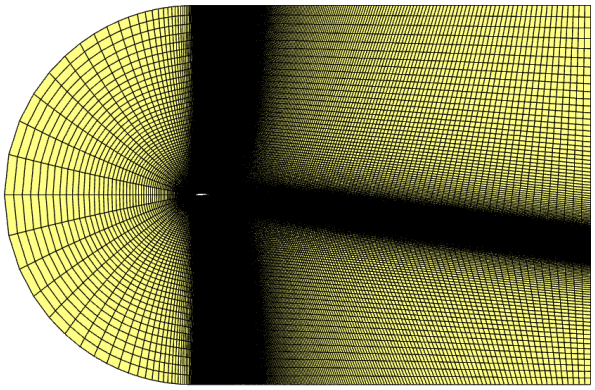

Figure 4.4 NACA4412 C-type grid global diagram

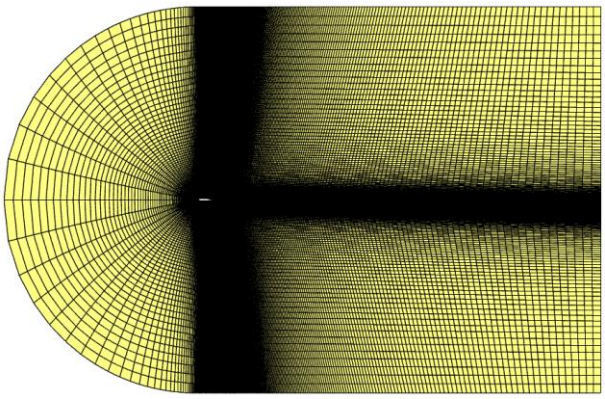

Figure 4.5 NACA23012 C-type grid global diagram

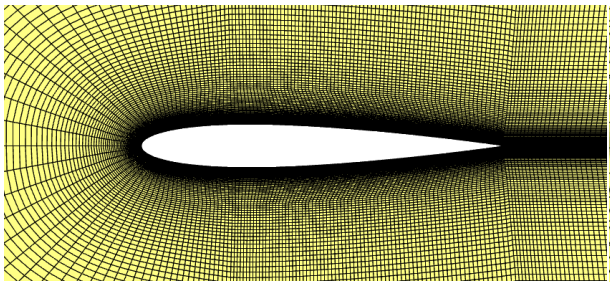

Figure 4.6 NACA0012 grid partial enlargement

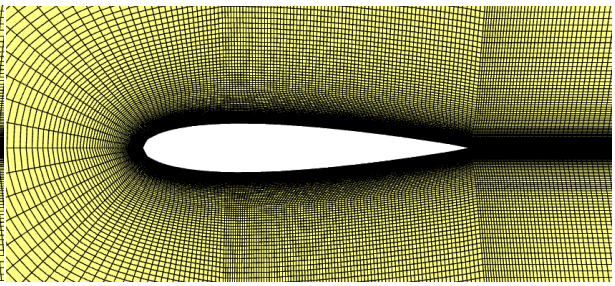

Figure 4.7 NACA0015 grid partial enlargement

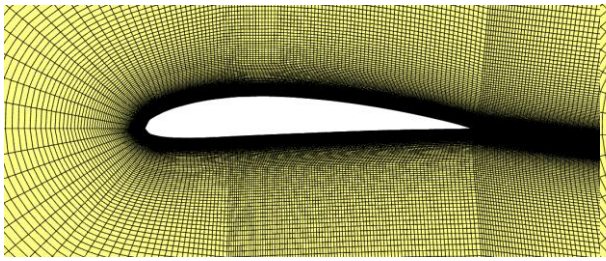

Figure 4.8 NACA4412 grid partial enlargement

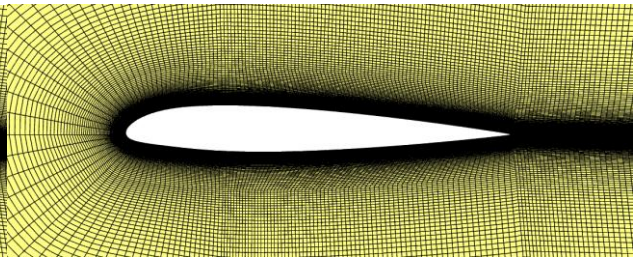

Figure 4.9 NACA23012 grid partial enlargement

The computational grid is generated in the Linux operating system using the blockMesh command provided by OpenFOAM, and the corresponding mesh generation file blockMeshDict is written by using a Python program.

The Python program used to write the blockMeshDict file mainly includes the following steps: 1) Define some key parameters for the mesh generation, such as: airfoil chord length, airfoil geometry data file to be imported, flow field height, wake length, the first layer grid height from the airfoil wall, grid size growth rate, the maximum grid size, trailing edge block angle, etc.; 2) Define relevant indicators for improving grid quality, such as: boundary layer height, grid size grading near the leading edge, grid size grading near the trailing edge, etc.; 3) Read the airfoil coordinate points, distinguish the upper and lower airfoil surfaces and perform quadrant division; 4) Calculate the normal vector of each coordinate point of the airfoil to stretch the boundary layer mesh; 5) Determine the coordinates of the trailing edge point, and the wake angle is determined according to the Kutta condition; 6) Define the key coordinate points for dividing the flow field into blocks; 7) Define the interpolation control points during grid division; 8) Calculate the grid size grading and grid size in each block; 9) Write the data obtained in the above steps into the blockMeshDict file according to the required format.

The blockMeshDict file of OpenFOAM is generally located in the system subfolder of the case folder, and its writing format has rules to follow, generally including: 1) Conversion of coordinate units; 2) Definition of block vertices; 3) Definition of blocks; 4) Definition of some special edges of each block, such as splines on the airfoil surface, interpolation lines at the outer

edge of the boundary layer, arcs of the freestream inlet, etc.; 5) Definition of the surfaces on which the boundary conditions should be applied. There are a total of 12 blocks written into this file, taking the NACA0012 airfoil as an example, the blocks diagram drawn is as follows:

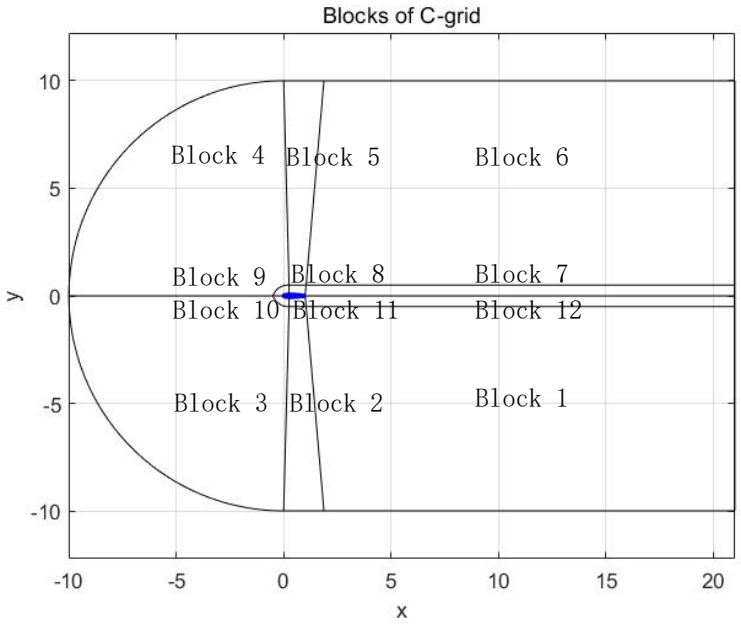

Figure 4.10 Twelve blocks of NACA0012 airfoil C-type grid

Block 7 to block 12 divide the boundary layer grid and are scaled approximately 50 times for display purposes. The actual boundary layer grid height is around $10mm$. Some parameter definitions of the C-type grid include: the airfoil chord length is set to $1m$; the length of the freestream inlet is $10m$; the height of the flow field and the length of the wake are $20m$; the height of the first layer grid from the airfoil wall is calculated by the y^+ calculator, which is in the order of $10^{-5}m$, mainly to ensure the accuracy of *SST k-ω* turbulence model; the growth rate of grid size is 1.05; the maximum grid size is 0.5 times the chord length; trailing edge block angle is 5°.

Finally, the blockMeshDict file was successfully written and obtained, and blockMesh command was used to generate C-type grid; in order to convert the grid into a recognizable format for Fluent solver, the foamMeshToFluent command was used to successfully convert foam-format mesh into the Fluent-format mesh. The grid generation work was completed, the number of grid nodes generated is about 260000, and the number of grid elements is about 130000; ICEM CFD was used to check the quality of the generated grid, the minimum grid quality is 0.667, the average grid quality is 0.975, computational requirement is satisfied. The grid quality histogram looks like this:

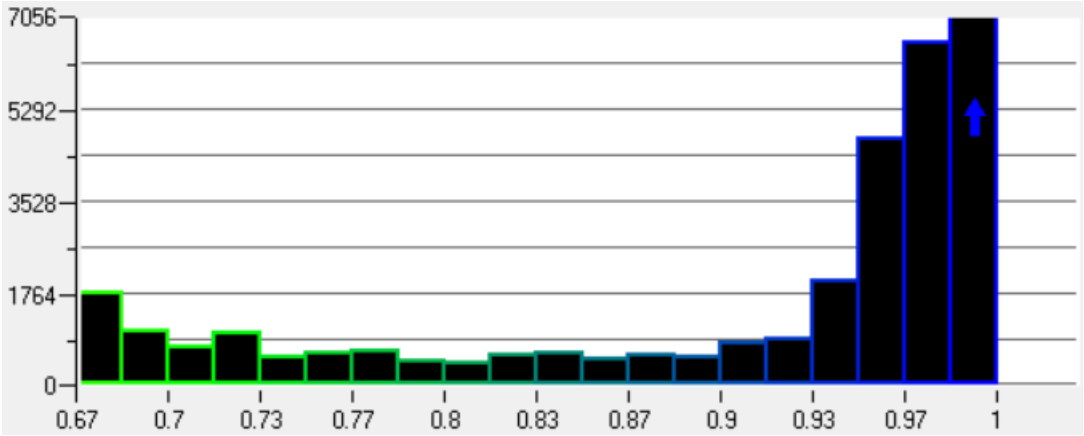

Figure 4.11 C-type grid quality histogram

When the airfoil icing phenomenon occurs, the original airfoil shape will be destroyed, so the existing grid needs to be updated to adapt to the new icing surface. The grid update technique provided by FENSAP-ICE is based on the arbitrary Lagrangian-Euler method (ALE) to determine the computational grid around the new surface.

In the framework of arbitrary Lagrangian-Eulerian method, the grid nodes can neither move with the displacement of the material particles, nor remain stationary in the original spatial position, and their movement velocity and movement position can be independent of the description of the Lagrangian method and the Euler method, therefore, this method adapts the deformation update of the grid to the shape of the airfoil after icing. Generally speaking, after the ice shape data points are obtained, the new icing surface is given by these data points; the ALE method is used to ensure that the grid nodes on the surface move and deform with the surface, and the nodes that are not on the surface will make corresponding movement adjustment according to the displacement of the surface nodes and a certain deformation law.

The deformation law of the grid can be determined by the method of elastic analogy, that is, each edge of the grid is regarded as a spring or other elastic body, and the grid nodes are located at both ends of the spring. At this time, the grid is actually represented by an elastic network composed of springs. According to the resultant force of each node of the grid, a force equation system is established, and combined with the initial conditions and boundary conditions, the motion behavior of all nodes can be calculated. In order to prevent the phenomenon of edge overlap(zero volume) or negative volume when the grid is deformed, some improvement strategies to the original linear spring analogy method have also been proposed one after another. For example, the spring can be considered as nonlinear, and its stiffness K_{ij}(i and j respectively represent the nodes at both ends of the spring) is no longer fixed. The smaller the

spring length, the greater the K_{ij}, and the greater the force against the node motion; or the grid is regarded as a solid structure, and a complete elastic analogy is performed, that is, the structural coefficients such as Young's modulus E and Poisson ratio ν are used and make them related to the element size to represent the force system, and the degree of grid deformation is determined by solving such a system. The smaller the mesh element, the larger the Young's modulus E, etc., the stiffer the element, and the less likely it is to be distorted to cause negative volume.

Considering the test condition given in Chapter 3, the comparison between the original grid and the deformed grid is presented after the NACA0012 airfoil is icing for 6 minutes:

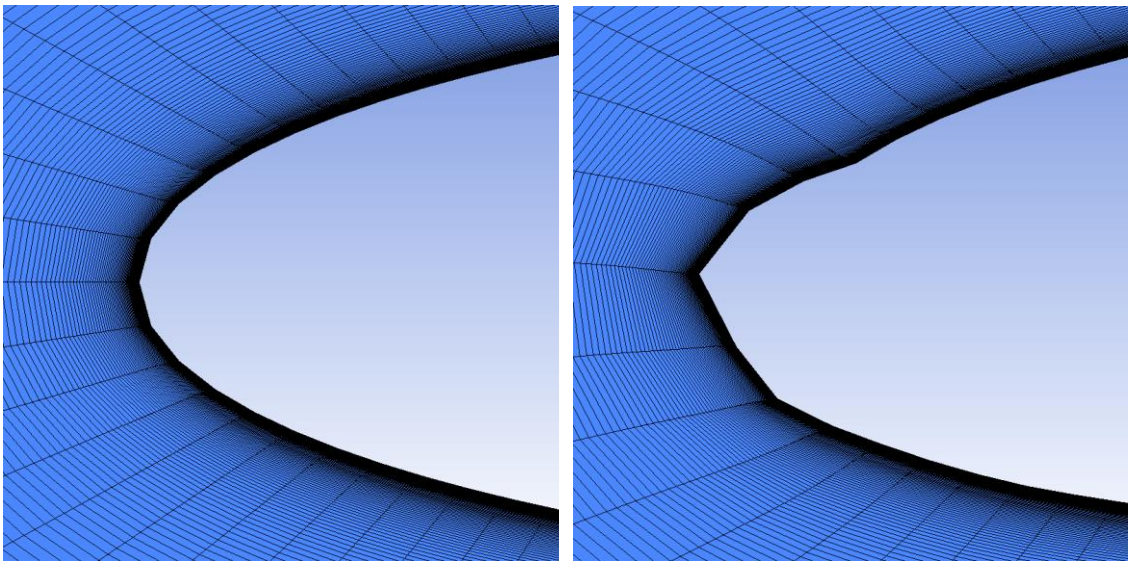

Figure 4.12 Comparison of original grid and deformed grid under the given NACA0012 airfoil test condition

4.3 Construction of ANSYS Numerical Simulation Platform

First, the computational grid is imported into Fluent solver, and the flow field computational model and fluid properties are set. This study uses a pressure-based solver for calculations and takes into account the effect of viscosity and turbulence, so the corresponding *SST k-ω* model needs to be selected; air is considered an ideal gas, and its viscosity is determined through Sutherland law as described above.

After that, boundary conditions need to be defined for the boundary surfaces. The freestream inlet boundary surface includes the frontmost inlet surface and the upper and lower surfaces of the far field, and the velocity inlet boundary condition is applied for it, in which the freestream velocity magnitude, the flight angle of attack and the static temperature of the freestream are defined to clarify the inlet conditions; Since the grid generated by OpenFOAM is

generally a 3D grid, and the default grid dimension of the Fluent solver is also 3D, it is necessary to set the front and back surfaces of the grid to symmetrical boundary conditions in Fluent, so that the airfoil icing problem in this study can be treated as a two-dimensional problem. if OpenFOAM was used to calculate the flow field around the airfoil, the front and back surfaces can be set as the empty boundary surfaces, in short, such surfaces do not participate in the calculation; the outlet boundary surface can be set as the pressure outlet boundary, the pressure remains the default 101325Pa, and the static temperature is consistent with that of freestream flow. The airfoil surface is regarded as a non-slip solid wall, and its thermal boundary condition selects a fixed wall temperature of 281*K*. This temperature value is only used to correctly calculate the convective heat transfer coefficient and convective heat flux. When ice accretion occurs, the surface temperature is still obtained by icing calculation, which has been clarified above; in addition, the roughness after icing is also introduced in the definition of wall boundary conditions: by selecting a high-roughness model, and importing the calculated roughness file after icing, the effects exerted by roughness can also be taken into account in the flow field solution. The schematic diagram of boundary surfaces and the corresponding boundary conditions are as follows:

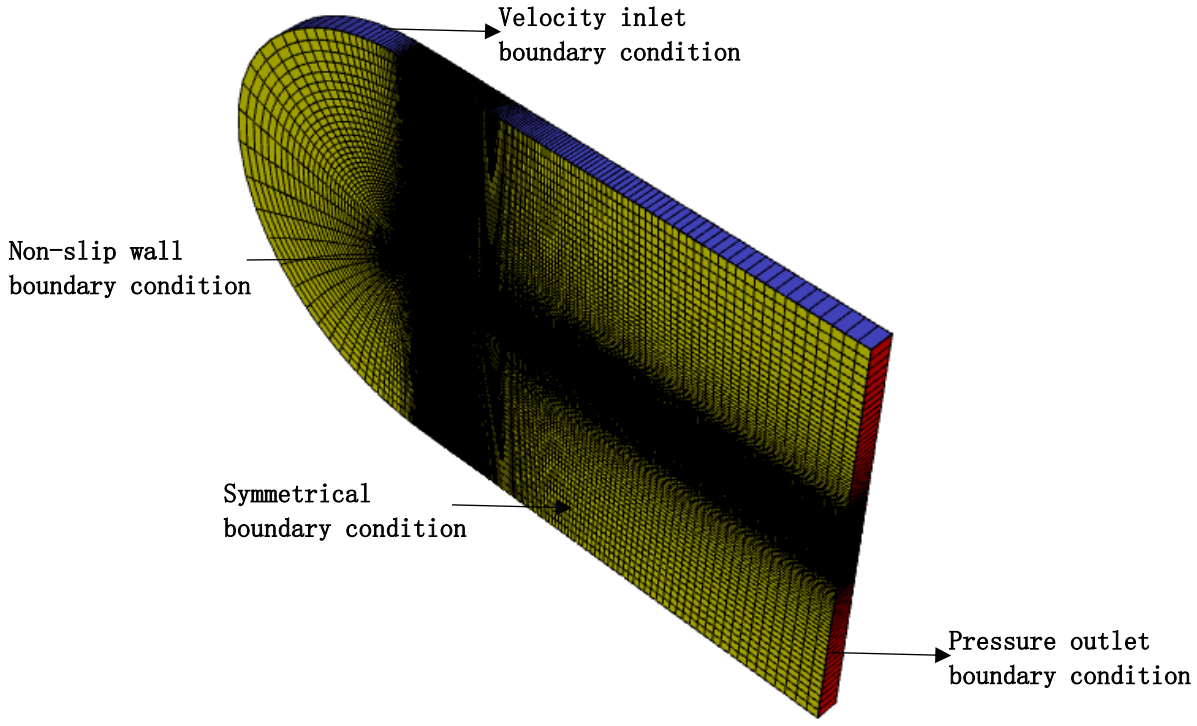

Figure 4.13 The boundary surfaces of the computational grid and the corresponding boundary conditions

After the boundary conditions are defined, the calculation reference values can be set to accurately calculate the lift coefficient and drag coefficient of the airfoil. Since the airfoil chord length is $1m$, and the grid length along the z direction is also $1m$, the reference area is determined to be $1m^2$; the reference values of velocity, temperature, pressure, etc. have been given in the previous definitions.

After the above preparations are completed, the calculation method used to solve the flow field and the discrete schemes for the terms of governing equations are given: the pressure-velocity coupled algorithm is used, the convection term adopts the second-order upwind scheme, the diffusion term adopts the central difference scheme, The gradient term adopts the weighted least square cell-based gradient method, and the pressure interpolation adopts the second-order interpolation. In addition, the convergence speed and convergence stability of the solution can be controlled by adjusting the relaxation factor of each quantity. If the relaxation factor is close to 1, the convergence speed of the numerical solution is relatively fast, but it may cause unstable oscillation of the solution and cannot meet the convergence conditions, so it is necessary to appropriately adjust the relaxation factor to a smaller value.

Since this study needs to compare the change of the aerodynamic coefficients before and after the airfoil is icing, the lift coefficient and drag coefficient are numerically solved by defining the directions of the lift and drag forces, and combining the calculation reference values set above. Finally, the allowable residual values are given as the convergence criterion(the default is 10^{-3}, and in this study is set to 10^{-6}), the residual monitor and the maximum number of iteration steps are set, and the flow field is initialized to start solving the problem.

When the solution is completed, the resulting data is transferred to the FENSAP-ICE solver, and the relevant parameters and boundary conditions for the calculation of the water droplets trajectory are set, including: the cloud liquid water concentration, the median volumetric diameter of the water droplets; the initial velocity components of the incoming droplets. After the relevant calculation settings are checked, and the maximum iteration time step is given, the solution of the droplets phase flow field is completed. The solutions of the air flow and the water droplets flow are stored in FENSAP-ICE as the input of airfoil icing. After the icing time is specified, the calculation can be carried out to obtain the ice accretion amount and ice shape at this time. The ice shape data is used for grid update to obtain a new computational grid after deformation. Repeating the above process, the ANSYS airfoil icing numerical simulation platform can be successfully built. The calculation flow chart of the numerical simulation platform is as follows:

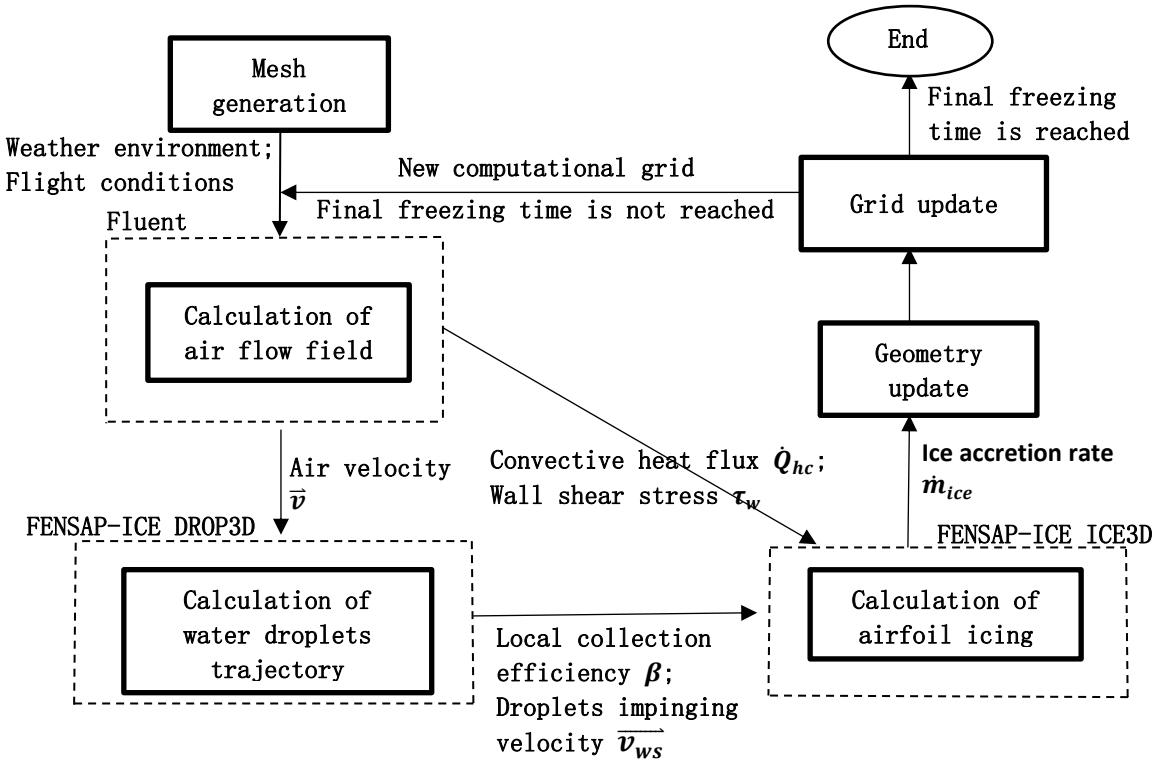

Figure 4.14 Calculation flow chart of ANSYS airfoil icing numerical simulation platform

The built ANSYS airfoil icing platform is shown in the following figure:

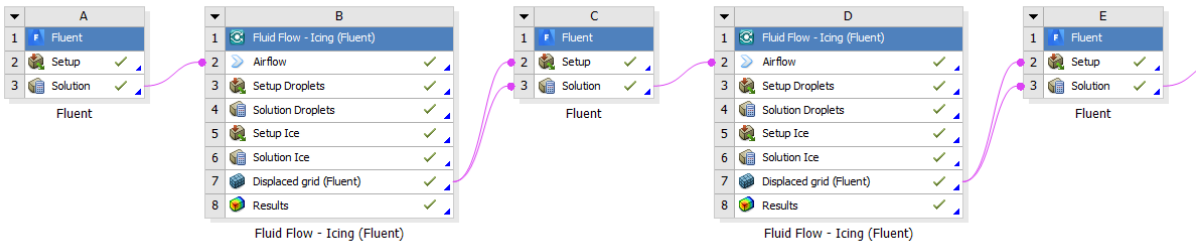

Figure 4.15 The built ANSYS airfoil icing platform(icing time is 4 minutes)

4.4 Verification of Airfoil Icing Numerical Simulation Platform

Combined with the reference results given by the icing wind tunnel experiments and NASA LEWICE icing simulation software, the numerical simulation platform built here was verified to judge its accuracy, so as to ensure the following analysis can be carried out smoothly. Because the vast majority of airfoil icing wind tunnel experiments select the NACA0012 airfoil as the research object, with sufficient data and high reliability, four verification cases of this airfoil icing were selected for this study, and the corresponding icing results were compared with the reference results of experiments and numerical simulations[44, 45]. Table 4.1 gives the specific

icing conditions for the four verification cases:

Table 4.1 Specific icing conditions for the four verification cases

Icing conditions	Verification case 1	Verification case 2	Verification case 3	Verification case 4
Selected airfoils	NACA0012	NACA0012	NACA0012	NACA0012
Chord length c(m)	0.5334	0.5334	0.5334	0.5334
Flight speed U_∞(m/s)	102.8	67.1	67.056	67.1
Angle of attack $\alpha(^\circ)$	4	4	4	4
Free flow pressure p_∞(Pa)	101300	101300	101300	101300
Free flow temperature $T_\infty(K)$	261.54	244.51	253.69	268.4
Liquid water concentration LWC(g/m^3)	0.47	1	1	1
Median volume diameter MVD(μm)	30	20	20	20
Total icing time t(min)	8.2	6	6	6
Single icing step Δt(min)	2	2	2	2

According to the above table, the icing airfoil shapes obtained by using the simulation platform are shown in the following figures:

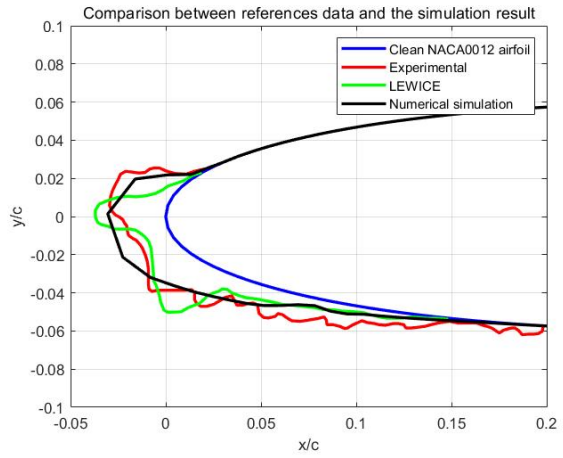

Figure 4.16 Ice shapes for verification case 1

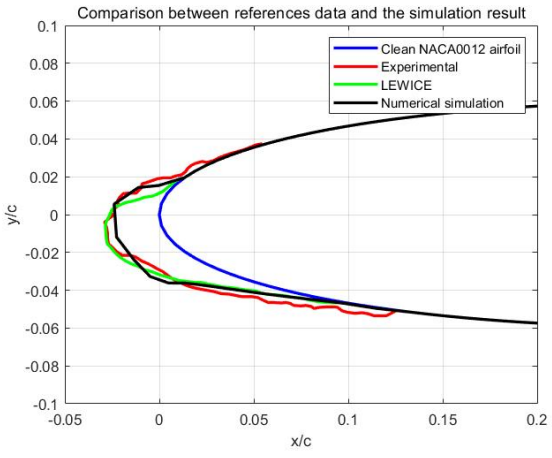

Figure 4.17 Ice shapes for verification case 2

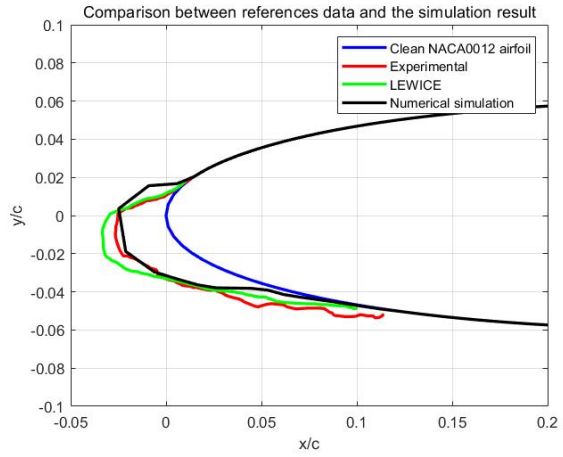

Figure 4.18 Ice shapes for verification case 3

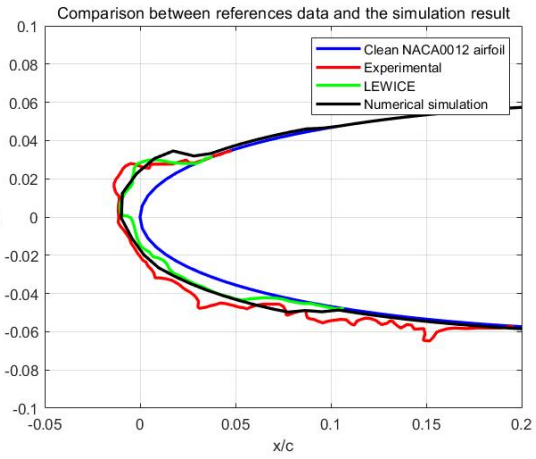

Figure 4.19 Ice shapes for verification case 4

The figures above correspond to the four verification cases in Table 4.1. The blue lines in the figures represent the clean NACA0012 airfoil, the black lines represent the icing shape calculated by the numerical simulation platform, the red lines represent the experimental reference icing shapes given in the literature, and the green lines represent the LEWICE numerical reference icing shapes. It can be seen from the figures that the icing shapes of NACA0012 airfoil obtained by the platform are basically consistent with the reference results, which verifies the reliability of the platform. Among these four cases, it is verified that the icing condition of case 1 corresponds to the mixed ice formation condition. Generally speaking, the mixed ice has relatively complex shape on the icing surface, and the current numerical simulation results have a certain deviation from the experimental results, so that the detailed icing shape cannot be well described, as shown in figure 4.16. While the icing conditions of verification case 2 and verification case 3 correspond to lower flight speed and lower free flow static temperature, therefore, the icing shapes are relatively simple, and the results are in good agreement; it is verified that the icing condition of case 4 corresponds to the clear ice formation condition, and the calculated icing shape profile is very similar to the references.

According to the above comparisons, the numerical simulation platform built in this study has the ability to solve the airfoil icing problem, and further in-depth research on ice accretion and its influence under different parameters conditions can be carried out.

4.5 Chapter Summary

This chapter discussed the construction of the ANSYS numerical simulation platform. According to the technical route of airfoil icing problem, the selection of airfoils and the generation of calculation grid were the first steps. This study chose NACA0012, NACA0015, NACA4412 and NACA23012 airfoils as the research objects, and illustrated the naming rules

of NACA series airfoils. In order to generate suitable calculation grids, the advantages and disadvantages of structured grids and unstructured grids were analyzed and compared, and C-type structured grids were selected for ice accretion. By using the Python program and the mesh generator carried by OpenFOAM, the calculation grids based on block division were created; then the grids were successfully imported into Fluent through the relevant operation commands, and the grid quality was checked in ICEM CFD.

After grid generation, Fluent solver, FENSAP-ICE DROP3D solver and FENSAP-ICE ICE3D ice accretion solver were configured in turn. The detailed icing conditions were specified by selecting the verification cases and the test cases. The relevant mathematical models and numerical methods had been discussed in Chapters 2 and 3. After each part of the calculation was completed, the resulting data were transferred between the above solvers according to the technical route; finally, the local collection efficiency of water droplets, icing shapes, and aerodynamic characteristics of airfoils after a certain time can be obtained.

After the numerical simulation platform was built, it needs to be verified. In this chapter, the most well-researched NACA0012 airfoil was selected, and four verification cases with experimental and numerical reference data were given, which successfully verified the accuracy of the ANSYS numerical simulation platform, and also showed that the calculations in this study were correct.

Chapter 5 Influence of airfoil icing on aerodynamic characteristics under different parameters

5.1 Foreword

When the weather conditions, flight conditions, etc. change, different icing shapes will appear on the airfoil surface, resulting in different degrees of aerodynamic performance deterioration. Therefore, the airfoil icing problem is actually affected by a variety of parameters. Among them, the key parameters related to weather conditions are: free flow temperature T_∞, cloud liquid water concentration(LWC), median volume diameter of water droplets(MVD), cloud range, and so on; the key parameters related to the flight conditions are: flight speed U_∞, flight angle of attack α, and so on. In this chapter, according to the idea of the control variable method, the values of the above parameters are changed in turn, and under different parameters, the local water droplet collection efficiency β, icing shape, surface pressure coefficient, and aerodynamic coefficients on the airfoil are studied, in order to see the influence of airfoil icing on aerodynamic characteristics.

5.2 Different Free Flow Temperature Conditions

In this study, four different free flow temperatures were selected, namely: −25°C; −15°C; −11°C; −7°C. The specific icing conditions are given in Table 5.1:

Table 5.1 Different free flow temperature conditions

Icing conditions	Test cases 1-4	Test cases 5-8	Test cases 9-12	Test cases 13-16
Selected airfoils	Four airfoils	Four airfoils	Four airfoils	Four airfoils
Chord length c(m)	1	1	1	1
Flight speed U_∞(m/s)	65	65	65	65
Angle of attack $\alpha(^\circ)$	4	4	4	4
Free flow pressure p_∞(Pa)	101325	101325	101325	101325
Free flow temperature $T_\infty(K)$	248.15	258.15	262.15	266.15
Liquid water concentration LWC(g/m^3)	1.0	1.0	1.0	1.0
Median volume diameter	25	25	25	25

MVD(μm)				
Total icing time t(min)	6	6	6	6
Single icing step Δt(min)	2	2	2	2

Under different temperature conditions, the local water droplet collection efficiency distributions of the four airfoils are shown in the following figures:

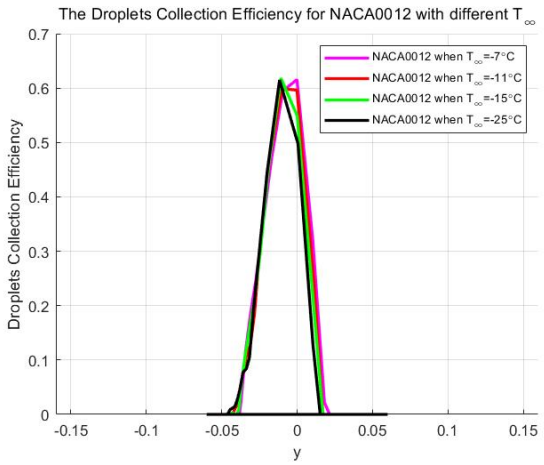

Figure 5.1 Collection efficiency of NACA0012 with different temperatures

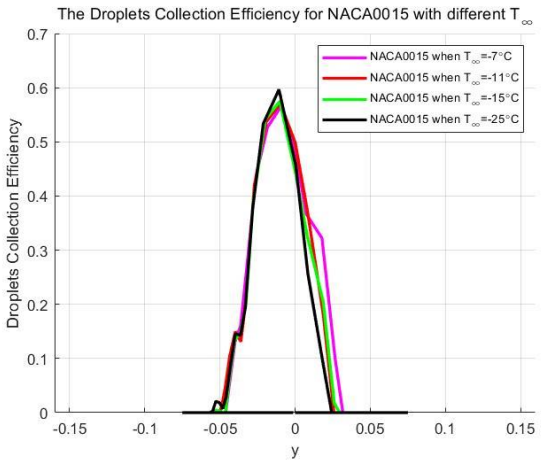

Figure 5.2 Collection efficiency of NACA0015 with different temperatures

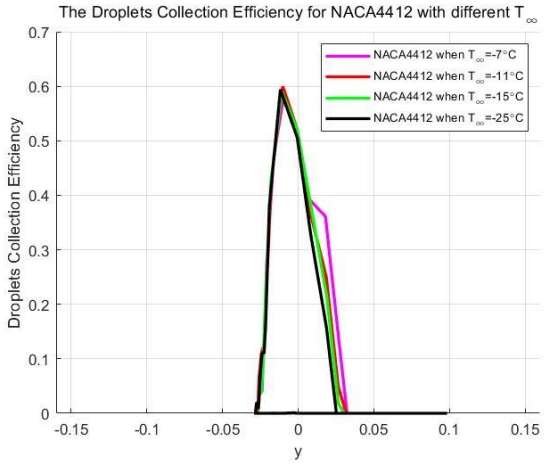

Figure 5.3 Collection efficiency of NACA4412 with different temperatures

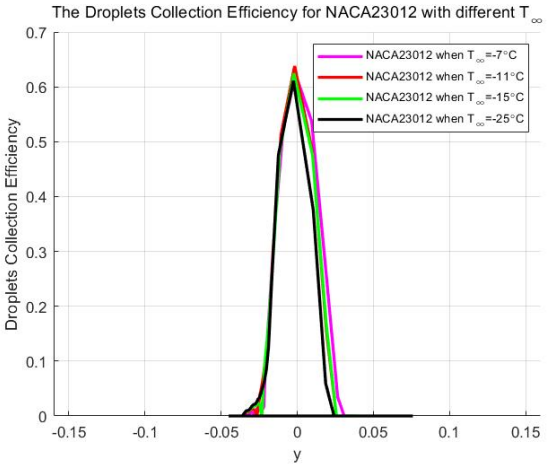

Figure 5.4 Collection efficiency of NACA23012 with different temperatures

The purple lines in the above figures correspond to $T_\infty = -7℃$, the red lines correspond to $T_\infty = -11℃$, the green lines correspond to $T_\infty = -15℃$, and the black lines correspond to $T_\infty = -25℃$. It can be seen from the figures that while keeping other parameters unchanged, the collection efficiency distributions of different airfoils under different temperatures are

different. For the two symmetrical airfoils NACA0012 and NACA0015, the overall collection efficiency distributions are skewed to the left, which means that at angle of attack of 4°, more water droplets in the free flow hit the lower surfaces of airfoils; while for the two cambered airfoils NACA4412 and NACA23012, although there are still many water droplets colliding with the lower airfoil surfaces, compared with symmetrical airfoils, the upper surfaces can intercept more droplets due to the camber.

After 6 minutes of ice accumulation, the ice shapes for the four airfoils are as follows:

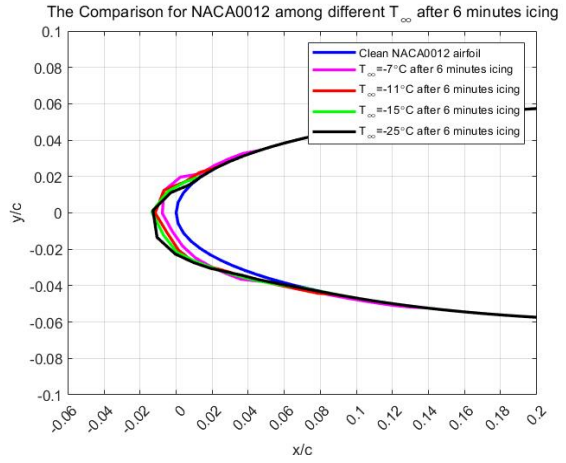

Figure 5.5 Ice shapes of NACA0012 with different temperatures

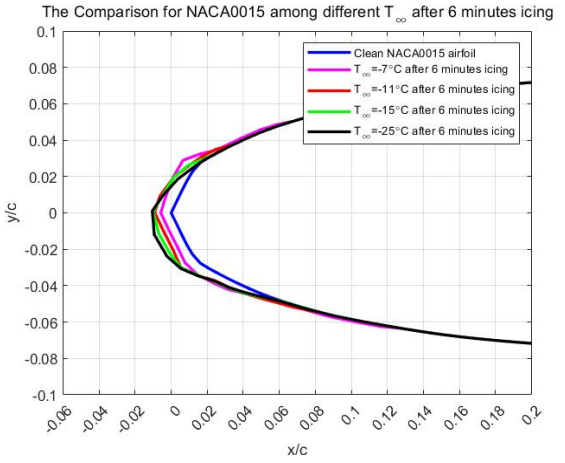

Figure 5.6 Ice shapes of NACA0015 with different temperatures

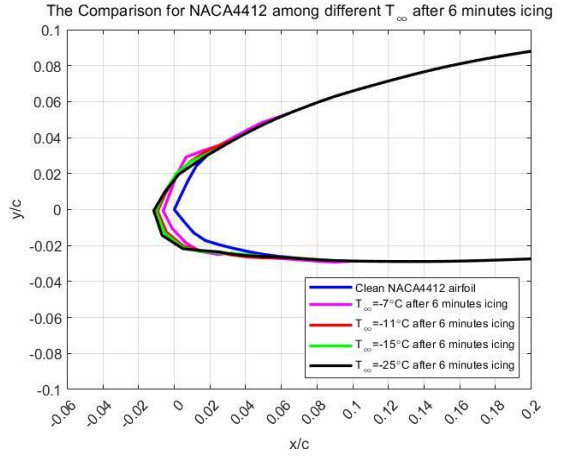

Figure 5.7 Ice shapes of NACA4412 with different temperatures

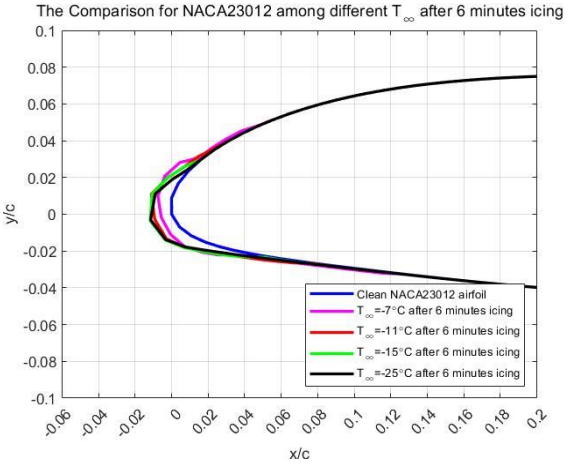

Figure 5.8 Ice shapes of NACA23012 with different temperatures

When the free flow temperature is −7°C, the ice shapes of the four airfoils are described by purple lines. It can be seen that there are protruding ice “horns” on the upper airfoil surfaces, which is an important feature of clear ice, indicating that when the temperature is higher, the upper surfaces are more likely to have ice accretion, and it is more likely to form

clear ice; when the temperature is as low as −25°C, there is no ice "horn", and the ice accretion has better streamlined shape, reflecting the characteristics of rime ice, as shown by the black lines in the above figures.

Under different temperature conditions, due to the difference in the icing types of airfoils, the surface pressure coefficient, lift and drag coefficient of the airfoils also change differently:

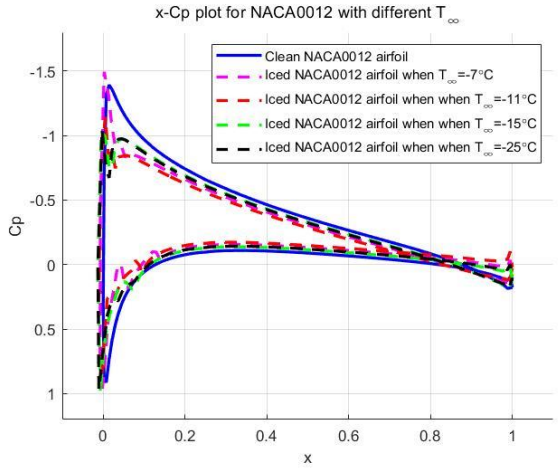

Figure 5.9 $x - Cp$ diagrams of NACA0012 with different temperatures

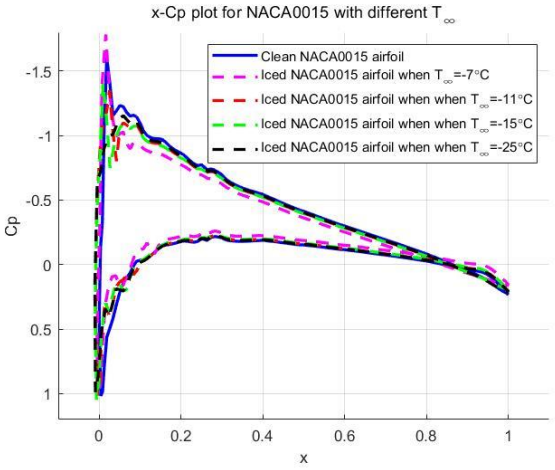

Figure 5.10 $x - Cp$ diagrams of NACA0015 with different temperatures

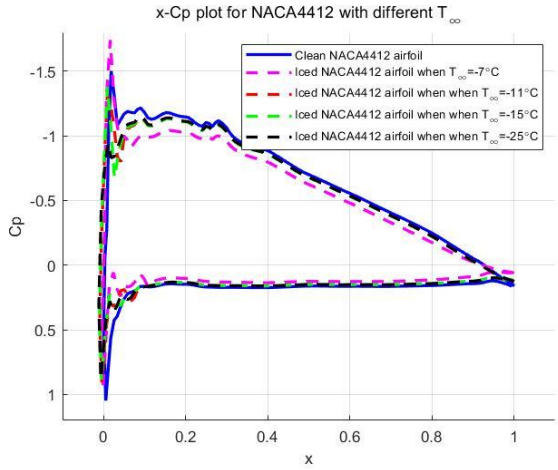

Figure 5.11 $x - Cp$ diagrams of NACA4412 with different temperatures

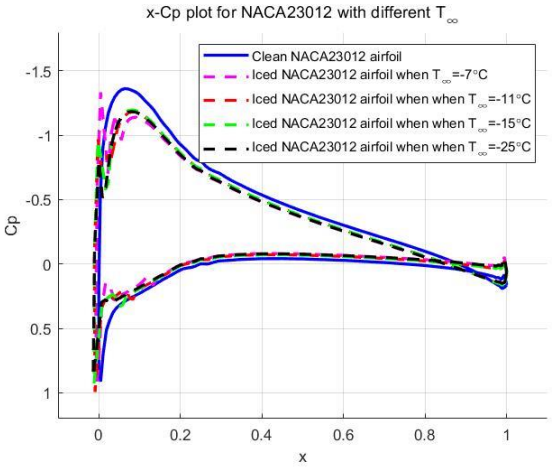

Figure 5.12 $x - Cp$ diagrams of NACA23012 with different temperatures

The x axis in the figures represents the position of the upper and lower airfoil surfaces along the chord length direction, and the y axis represents the surface pressure coefficient Cp. According to the expression convention, the y axis is reversed, which means that the upper half of the curve reflects the pressure coefficient on the upper surface, and the lower half of the curve reflects the pressure coefficient on the lower surface. Due to ice accretion, the pressure coefficients on the airfoil surfaces start to change from a negative x value; different

temperature conditions have different effects on the surface pressure coefficients, which are represented by dotted lines; while the blue solid lines represent the $x - Cp$ curves of clean airfoils. In general, ice accretion will reduce the pressure difference between the upper and lower airfoil surfaces. The free flow temperature of −7°C has a relatively large influence on the distribution of Cp, which can be seen from the purple dotted lines in the figures.

The following tables show the changes of the lift and drag coefficients of the four airfoils under different temperature conditions:

Table 5.2 Variation of lift and drag coefficients of NACA0012 under different temperature conditions

Incoming temperature T_∞(℃)	Initial C_L	After icing C_{L_ice}	Loss percentage of C_L(%)	Initial C_D	After icing C_{D_ice}	Growth percentage of C_D(%)
−25	0.41456	0.33215	19.88%	0.009948	0.015185	52.64%
−15	0.41493	0.34680	16.42%	0.010058	0.014234	41.52%
−11	0.41506	0.25715	38.04%	0.010102	0.018836	86.46%
−7	0.41519	0.30186	27.30%	0.010144	0.019887	96.05%

Table 5.3 Variation of lift and drag coefficients of NACA0015 under different temperature conditions

Incoming temperature T_∞(℃)	Initial C_L	After icing C_{L_ice}	Loss percentage of C_L(%)	Initial C_D	After icing C_{D_ice}	Growth percentage of C_D(%)
−25	0.40237	0.38695	3.83%	0.011670	0.012247	4.94%
−15	0.40407	0.36896	8.69%	0.011756	0.014754	25.50%
−11	0.40358	0.37961	5.94%	0.011795	0.013132	11.36%
−7	0.40393	0.30794	23.76%	0.011835	0.018738	58.33%

Table 5.4 Variation of lift and drag coefficients of NACA4412 under different temperature conditions

Incoming temperature T_∞(℃)	Initial C_L	After icing C_{L_ice}	Loss percentage of C_L(%)	Initial C_D	After icing C_{D_ice}	Growth percentage of C_D(%)
−25	0.84333	0.80565	4.47%	0.012960	0.013545	4.51%
−15	0.84481	0.80174	5.10%	0.013050	0.013987	7.18%
−11	0.84539	0.80622	4.63%	0.013090	0.013845	5.77%
−7	0.84594	0.72204	14.65%	0.013120	0.020746	58.13%

Table 5.5 Variation of lift and drag coefficients of NACA23012 under different temperature conditions

Incoming temperature T_∞(℃)	Initial C_L	After icing C_{L_ice}	Loss percentage of C_L(%)	Initial C_D	After icing C_{D_ice}	Growth percentage of C_D(%)
−25	0.54335	0.43700	19.57%	0.01007	0.015668	55.59%
−15	0.54374	0.45796	15.78%	0.010184	0.015054	47.82%
−11	0.54382	0.45844	15.70%	0.010231	0.015504	51.54%
−7	0.54393	0.43405	20.20%	0.010275	0.016486	60.45%

It can be seen from the above tables that when the temperature conditions change, the lift loss and the drag growth of different airfoils are quite different. Therefore, the change of lift and drag cannot be generalized, and it needs to be determined according to the selected airfoils and specific icing conditions. In this study, the four airfoils all showed severe lift and drag deterioration at free flow temperature of −7°C, because the obvious ice "horns" appeared on the upper airfoil surfaces, and the aerodynamic shapes of the airfoils were greatly damaged.

5.3 Different Cloud Liquid Water Concentration Conditions

The liquid water concentration(LWC) in the cloud directly determines the mass of supercooled water droplets that collide with the airfoil per unit time, which in turn affects the amount of ice accretion on the airfoil. In this study, five conditions of cloud liquid water concentration were selected: $0.5g/m^3$, $0.7g/m^3$, $1.0g/m^3$, $1.5g/m^3$, $2.0g/m^3$, and the specific icing conditions are shown in the following table:

Table 5.6 Different cloud liquid water concentration conditions

Icing conditions	Test cases 17-20	Test cases 21-24	Test cases 25-28	Test cases 29-32	Test cases 33-36
Selected airfoils	Four airfoils	Four airfoils	Four airfoils	Four airfoils	Four airfoils
Chord length c(m)	1	1	1	1	1
Flight speed U_∞(m/s)	65	65	65	65	65
Angle of attack $\alpha(^\circ)$	4	4	4	4	4
Free flow pressure p_∞(Pa)	101325	101325	101325	101325	101325
Free flow temperature $T_\infty(K)$	258.15	258.15	258.15	258.15	258.15
Liquid water concentration LWC(g/m^3)	0.5	0.7	1.0	1.5	2.0
Median volume diameter MVD(μm)	25	25	25	25	25

Total icing time t(min)	6	6	6	6	6
Single icing step Δt(min)	2	2	2	2	2

The collection efficiency distributions corresponding to different cloud liquid water concentrations for different airfoils are shown in the following figures:

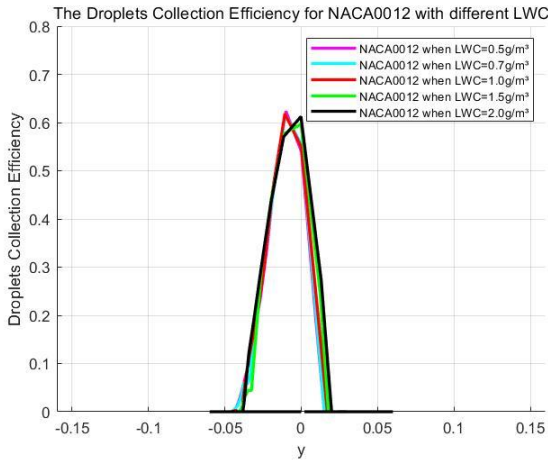

Figure 5.13 Collection efficiency of NACA0012 with different LWC

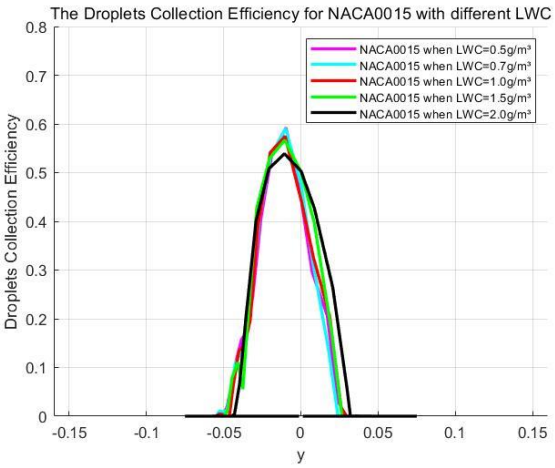

Figure 5.14 Collection efficiency of NACA0015 with different LWC

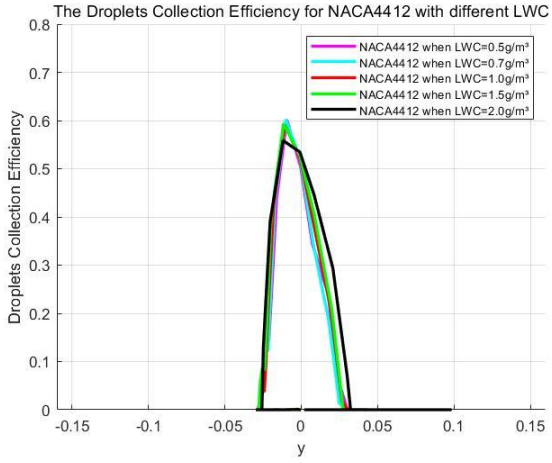

Figure 5.15 Collection efficiency of NACA4412 with different LWC

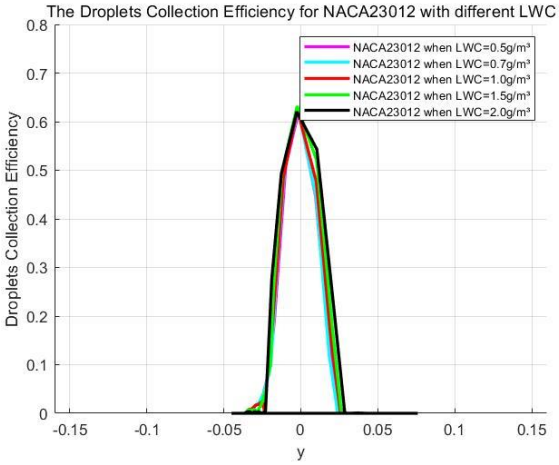

Figure 5.16 Collection efficiency of NACA23012 with different LWC

The droplet collection efficiency distributions of each airfoil under different liquid water concentrations are basically the same or very similar, indicating that the liquid water concentration and the collection efficiency are independent of each other, that is, the liquid water concentration hardly affects the impact range and impact location of supercooled water

droplets on the airfoil surface. In fact, $LWC = 2.0g/m^3$ is already a very high concentration value, which has little effect on the collection efficiency; however, in the same icing time, the high liquid water concentration will significantly increase the amount of ice accretion on the airfoil, which can be reflected by the ice shapes after 6 minutes of icing:

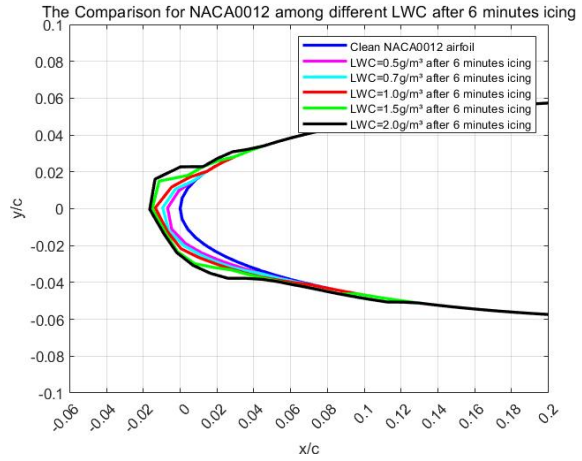

Figure 5.17 Ice shapes of NACA0012 with different LWC

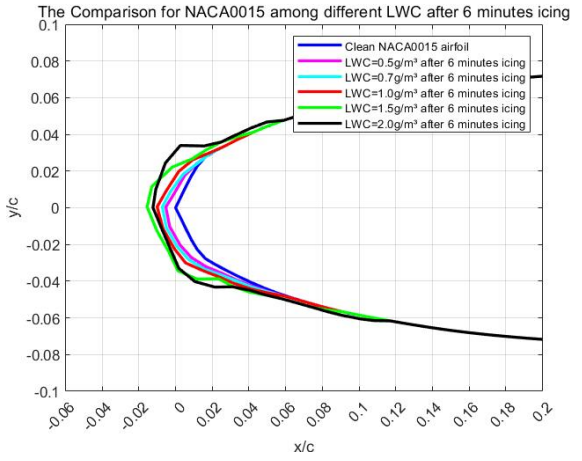

Figure 5.18 Ice shapes of NACA0015 with different LWC

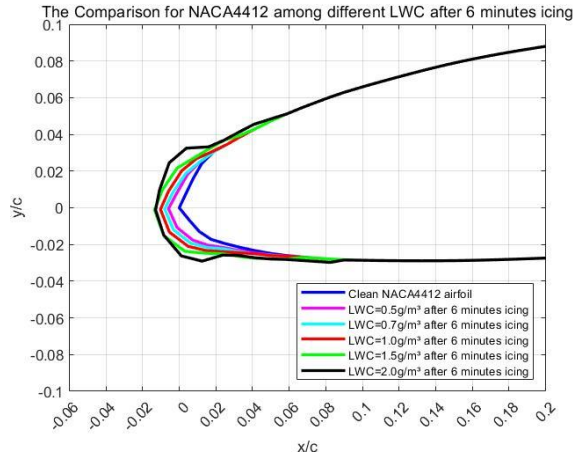

Figure 5.19 Ice shapes of NACA4412 with different LWC

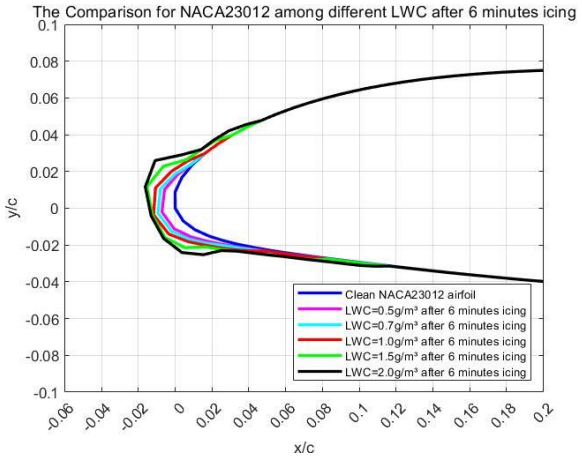

Figure 5.20 Ice shapes of NACA23012 with different LWC

The blue lines in the figures represent the clean airfoil shapes, the purple lines represent the ice shapes with $LWC = 0.5g/m^3$, the light blue lines represent the ice shapes with $LWC = 0.7g/m^3$, the red lines represent the ice shapes with $LWC = 1.0g/m^3$, the green lines represent the ice shapes with $LWC = 1.5g/m^3$, and the black lines represent the ice shapes with $LWC = 2.0g/m^3$. When $LWC = 0.5g/m^3$, the amount of ice accretion on the airfoils is the smallest; as the liquid water concentration gradually increases, the ice accretion on the airfoils also gradually thickens. When $LWC = 2.0g/m^3$, the airfoil icing problem is

quite serious, there is a certain amount of ice on the upper and lower airfoil surfaces, and the ice shapes are irregular, which significantly deteriorates the aerodynamic characteristics of the airfoils.

The following figures reflect the changes of the surface pressure coefficient of the four airfoils under different LWC:

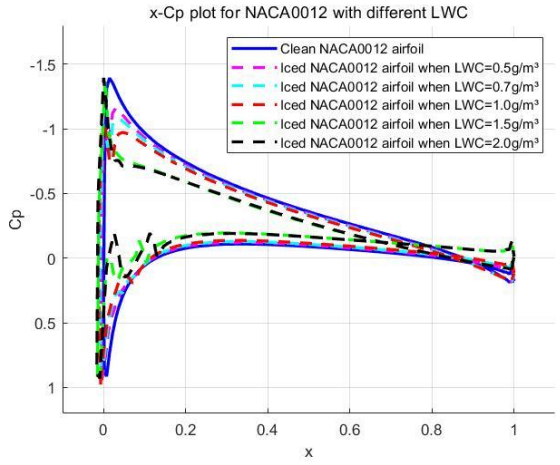

Figure 5.21 $x-Cp$ diagrams of NACA0012 with different LWC

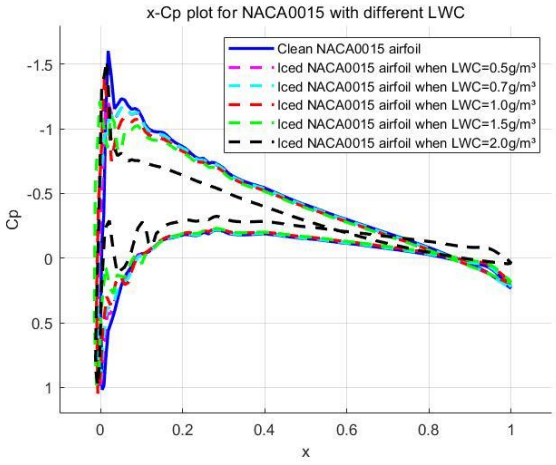

Figure 5.22 $x-Cp$ diagrams of NACA0015 with different LWC

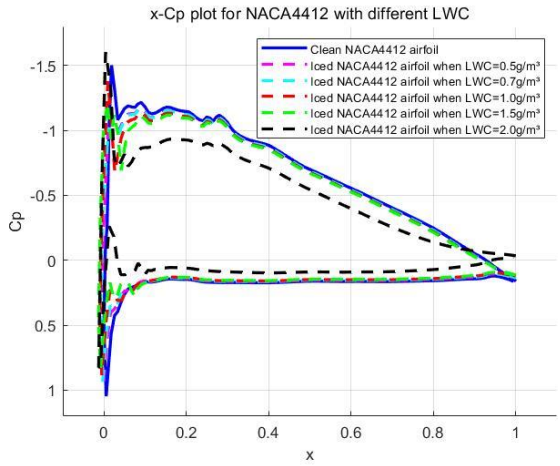

Figure 5.23 $x-Cp$ diagrams of NACA4412 with different LWC

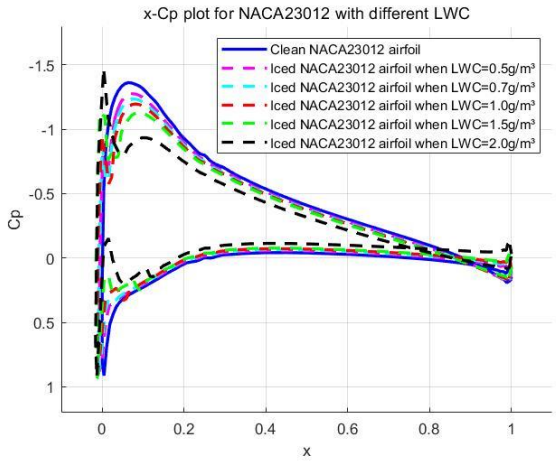

Figure 5.24 $x-Cp$ diagrams of NACA23012 with different LWC

It can be seen from the figures that when the liquid water concentration is low, the surface pressure coefficients on the icing airfoils are not much different from those on the clean airfoils; while when the liquid water concentration reaches $2.0g/m^3$, the surface pressure coefficients of the four airfoils have significant changes, and the pressure differences between the upper and lower surfaces are greatly reduced. Therefore, it can be predicted that

under this condition, the icing airfoil will have a greater loss of lift coefficient. The specific variation of the lift and drag coefficients of each airfoil is shown in the following tables:

Table 5.7 Variation of lift and drag coefficients of NACA0012 under different LWC conditions

LWC (g/m^3)	Initial C_L	After icing C_{L_ice}	Loss percentage of C_L(%)	Initial C_D	After icing C_{D_ice}	Growth percentage of C_D(%)
0.5	0.41493	0.38093	8.19%	0.010058	0.011500	14.34%
0.7	0.41493	0.36558	11.89%	0.010058	0.012692	26.19%
1.0	0.41493	0.34680	16.42%	0.010058	0.014234	41.52%
1.5	0.41493	0.22278	46.31%	0.010058	0.030150	199.76%
2.0	0.41493	0.22421	45.96%	0.010058	0.028858	186.92%

Table 5.8 Variation of lift and drag coefficients of NACA0015 under different LWC conditions

LWC (g/m^3)	Initial C_L	After icing C_{L_ice}	Loss percentage of C_L(%)	Initial C_D	After icing C_{D_ice}	Growth percentage of C_D(%)
0.5	0.40407	0.38582	4.52%	0.011756	0.012157	3.41%
0.7	0.40407	0.39305	2.73%	0.011756	0.011840	0.71%
1.0	0.40407	0.36896	8.69%	0.011756	0.014754	25.50%
1.5	0.40407	0.36165	10.50%	0.011756	0.015454	31.46%
2.0	0.40407	0.17345	57.07%	0.011756	0.033605	185.85%

Table 5.9 Variation of lift and drag coefficients of NACA4412 under different LWC conditions

LWC (g/m^3)	Initial C_L	After icing C_{L_ice}	Loss percentage of C_L(%)	Initial C_D	After icing C_{D_ice}	Growth percentage of C_D(%)
0.5	0.84481	0.81685	3.31%	0.013050	0.013079	0.22%
0.7	0.84481	0.81648	3.35%	0.013050	0.013095	0.34%
1.0	0.84481	0.80174	5.10%	0.013050	0.013987	7.18%
1.5	0.84481	0.79223	6.22%	0.013050	0.014879	14.02%
2.0	0.84481	0.60873	27.94%	0.013050	0.029013	122.32%

Table 5.10 Variation of lift and drag coefficients of NACA23012 under different LWC conditions

LWC (g/m^3)	Initial C_L	After icing C_{L_ice}	Loss percentage of C_L(%)	Initial C_D	After icing C_{D_ice}	Growth percentage of C_D(%)
0.5	0.54374	0.49525	8.92%	0.010184	0.012473	22.48%
0.7	0.54374	0.47300	13.01%	0.010184	0.013970	37.18%

1.0	0.54374	0.45796	15.78%	0.010184	0.015054	47.82%
1.5	0.54374	0.44599	17.98%	0.010184	0.017604	72.86%
2.0	0.54374	0.35032	35.57%	0.010184	0.026910	164.24%

From the changes of lift and drag coefficients with different liquid water concentration, it can be seen that with the increase of liquid water concentration, the loss percentage of lift coefficients and the growth percentage of drag coefficients of the four airfoils are also getting higher and higher, especially when $LWC = 2.0g/m^3$, the lift losses of the four airfoils are all over 25%, the drag growth exceeds 100%, and the aerodynamic characteristics of the airfoils drop sharply. The performance changes of different airfoils under different cloud liquid water concentrations still need to be determined according to the specific icing conditions and actual calculations, but the effects caused by high liquid water concentrations cannot be underestimated. Therefore, some aircraft should avoid cumulonimbus clouds as much as possible when flying to prevent crashes.

5.4 Different Median Volume Diameter Conditions

The median volume diameter(MVD) of water droplets refers to the diameter of a single spherical particle when the actual water droplets particles group is replaced by a spherical particles group of the same volume. In Chapter 3, it was assumed that the water droplets are spherical, so the equivalent diameter d_w of the spherical water droplets can represent the median volume diameter. In this study, three diameters of $10\mu m$, $25\mu m$ and $40\mu m$ were selected to explore the icing situations of airfoils. The specific icing conditions are shown in the following table:

Table 5.11 Different median volume diameter conditions

Icing conditions	Test cases 37-40	Test cases 41-44	Test cases 45-48
Selected airfoils	Four airfoils	Four airfoils	Four airfoils
Chord length c(m)	1	1	1
Flight speed U_∞(m/s)	65	65	65
Angle of attack $\alpha(^\circ)$	4	4	4
Free flow pressure p_∞(Pa)	101325	101325	101325
Free flow temperature $T_\infty(K)$	258.15	258.15	258.15
Liquid water concentration LWC(g/m^3)	1.0	1.0	1.0
Median volume diameter MVD(μm)	10	25	40

Total icing time t(min)	6	6	6
Single icing step Δt(min)	2	2	2

The median volume diameter of water droplets has a direct influence on the droplet collection efficiency distribution, which can be reflected in the following figures:

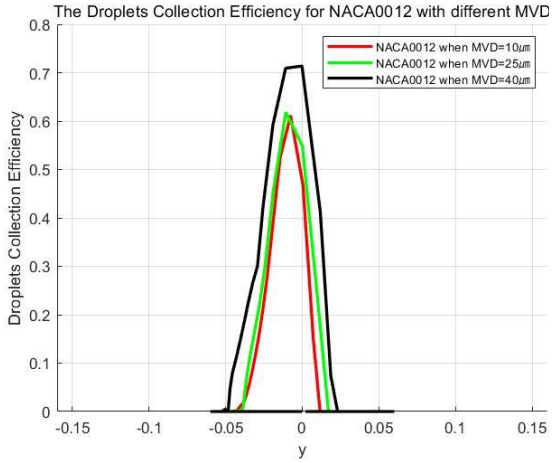

Figure 5.25 Collection efficiency of NACA0012 with different MVD

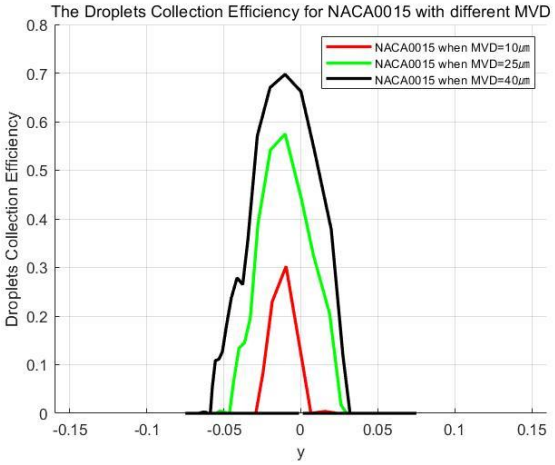

Figure 5.26 Collection efficiency of NACA0015 with different MVD

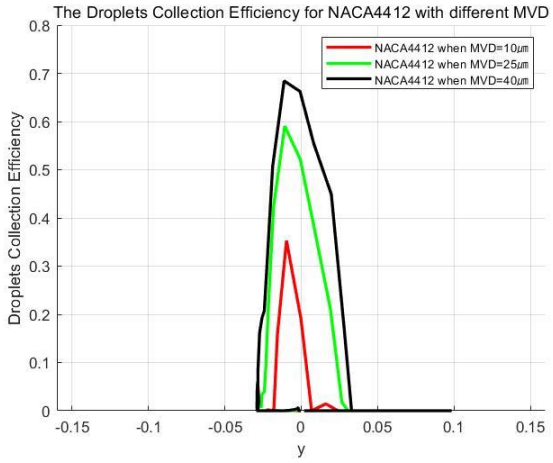

Figure 5.27 Collection efficiency of NACA4412 with different MVD

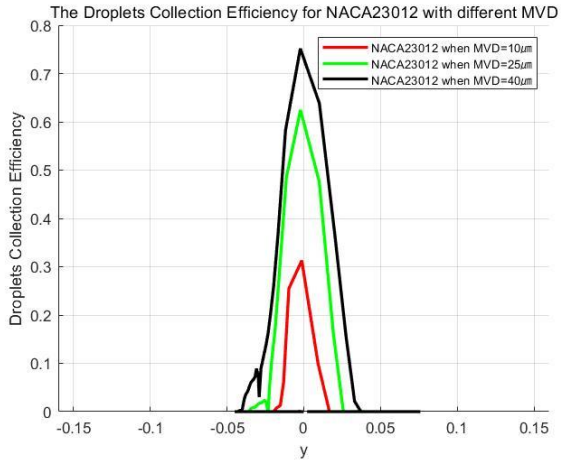

Figure 5.28 Collection efficiency of NACA23012 with different MVD

The red lines in the figures correspond to the droplets of $MVD = 10\mu m$, the green lines correspond to the droplets of $MVD = 25\mu m$, and the black lines correspond to the droplets of $MVD = 40\mu m$. It can be seen that the larger the diameter of the supercooled water droplets, the larger the impact limit on the upper and lower airfoil surfaces, and the wider the range of ice accretion; in addition, at a given airfoil position, the larger the MVD, the more the

freestream water droplets are successfully intercepted, therefore, the height of the curve at a fixed abscissa in the above figures is higher. The reason for this phenomenon is that the larger supercooled water droplets have larger inertia and will not easily change the original motion state when moving in the flow field, there will be more water droplets hitting the airfoil, so that both width and height of the curve will increase. Therefore, the median volume diameter of droplets affects the ice accretion amount on the airfoil by affecting the local water droplet collection efficiency β. The final ice shapes look like this:

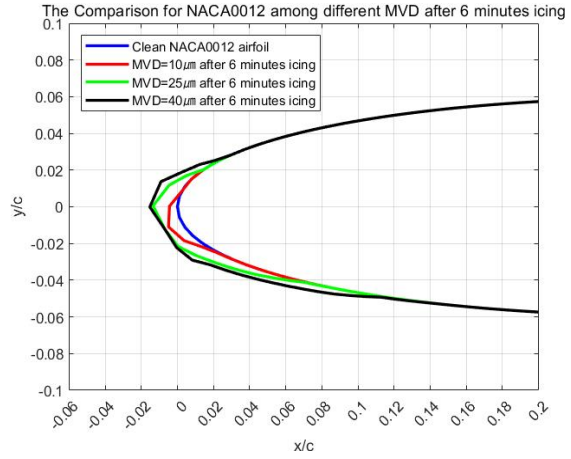

Figure 5.29 Ice shapes of NACA0012 with different MVD

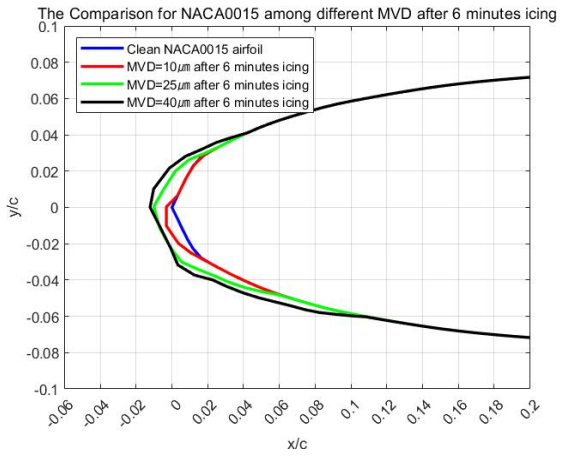

Figure 5.30 Ice shapes of NACA0015 with different MVD

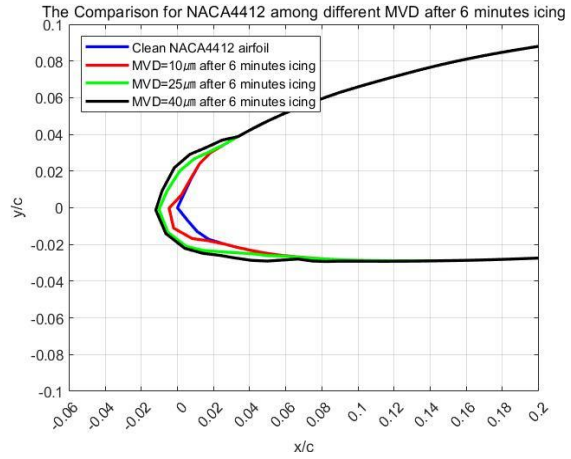

Figure 5.31 Ice shapes of NACA4412 with different MVD

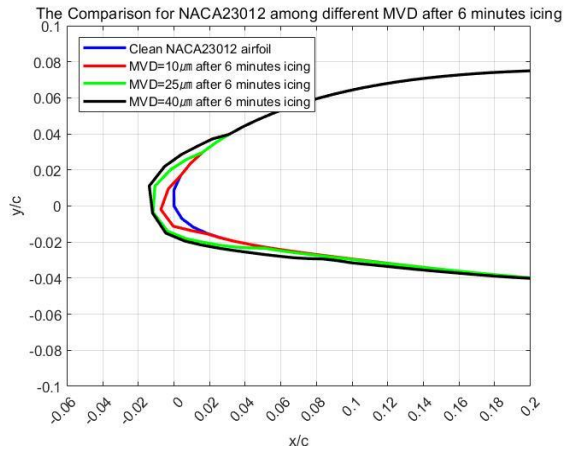

Figure 5.32 Ice shapes of NACA23012 with different MVD

Within 6 minutes, when $MVD = 10\mu m$, the amount of ice accretion on the airfoil surface is small, and the ice-covered area is mainly concentrated on the lower surface; when $MVD = 40\mu m$, there is a significant increase in the icing amount, and the ice-covered area is also much wider.

The following figures show the changes of the surface pressure coefficients under

different median volume diameters:

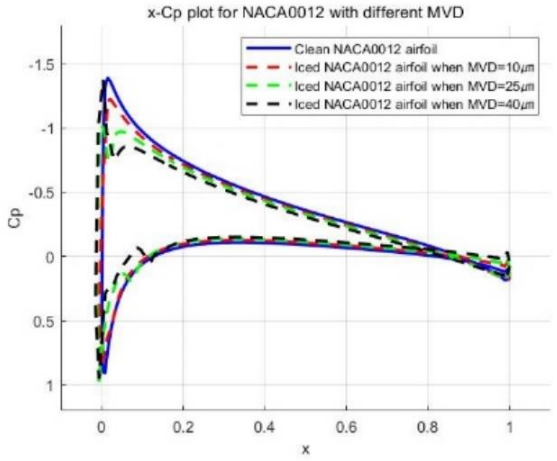

Figure 5.33 $x-Cp$ diagrams of NACA0012 with different MVD

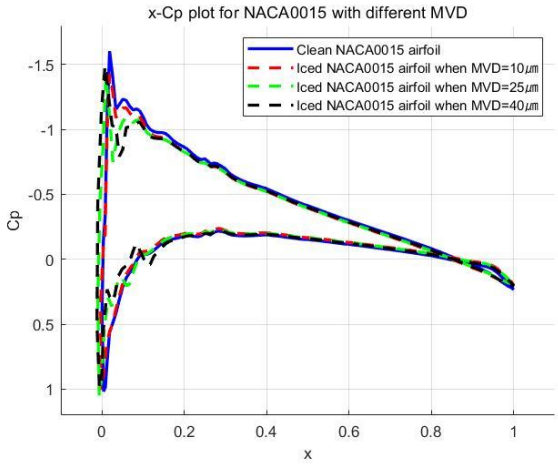

Figure 5.34 $x-Cp$ diagrams of NACA0015 with different MVD

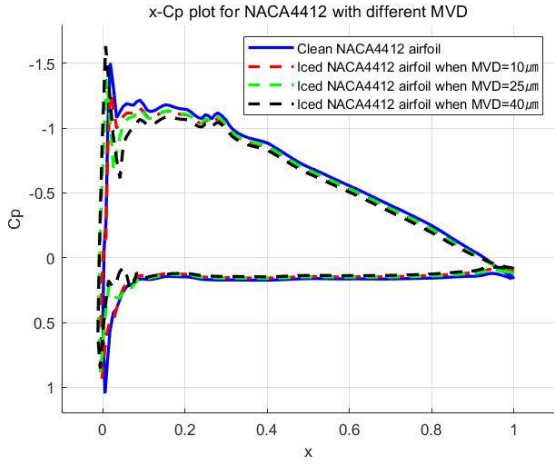

Figure 5.35 $x-Cp$ diagrams of NACA4412 with different MVD

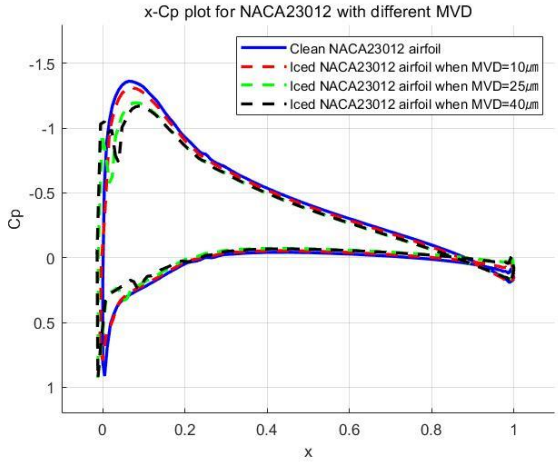

Figure 5.36 $x-Cp$ diagrams of NACA23012 with different MVD

When the median volume diameter of supercooled water droplets is $10\mu m$, the pressure coefficients on the icing airfoils are close to those on the clean airfoils; when the median volume diameter of supercooled water droplets is $40\mu m$, the pressure coefficients show obvious changes, as shown by the black dotted lines.

The deteriorations of the lift and drag coefficients under the conditions of three median volume diameters are as follows:

Table 5.12 Variation of lift and drag coefficients of NACA0012 under different MVD conditions

MVD (μm)	Initial C_L	After icing C_{L_ice}	Loss percentage of C_L(%)	Initial C_D	After icing C_{D_ice}	Growth percentage of C_D(%)
10	0.41493	0.37001	10.83%	0.010058	0.011988	19.19%
25	0.41493	0.34680	16.42%	0.010058	0.014234	41.52%
40	0.41493	0.30261	27.07%	0.010058	0.016531	64.36%

Table 5.13 Variation of lift and drag coefficients of NACA0015 under different MVD conditions

MVD (μm)	Initial C_L	After icing C_{L_ice}	Loss percentage of C_L(%)	Initial C_D	After icing C_{D_ice}	Growth percentage of C_D(%)
10	0.40407	0.36171	10.48%	0.011756	0.012930	9.99%
25	0.40407	0.36896	8.69%	0.011756	0.014754	25.50%
40	0.40407	0.38149	5.59%	0.011756	0.013386	13.87%

Table 5.14 Variation of lift and drag coefficients of NACA4412 under different MVD conditions

MVD (μm)	Initial C_L	After icing C_{L_ice}	Loss percentage of C_L(%)	Initial C_D	After icing C_{D_ice}	Growth percentage of C_D(%)
10	0.84481	0.78983	6.51%	0.013050	0.014283	9.45%
25	0.84481	0.80174	5.10%	0.013050	0.013987	7.18%
40	0.84481	0.75930	10.12%	0.013050	0.016654	27.62%

Table 5.15 Variation of lift and drag coefficients of NACA23012 under different MVD conditions

MVD (μm)	Initial C_L	After icing C_{L_ice}	Loss percentage of C_L(%)	Initial C_D	After icing C_{D_ice}	Growth percentage of C_D(%)
10	0.54374	0.50864	6.46%	0.010184	0.011215	10.12%
25	0.54374	0.45796	15.78%	0.010184	0.015054	47.82%
40	0.54374	0.46633	14.24%	0.010184	0.015082	48.10%

For the three airfoils of NACA0012, NACA4412 and NACA23012, when MVD = 40μm, the ice shapes on the airfoils are irregular, and the protruding ice “horns” can be observed on the upper surfaces, which makes the lift and drag coefficients have large change; For the NACA0015 airfoil, the ice shape is relatively regular when MVD = 40μm; although there is a certain amount of ice accretion on the upper surface, the overall transition is relatively smooth, resulting in a little change in aerodynamic characteristics. The reasons for the above differences may be related to the maximum thickness of the airfoils or to specific icing conditions, which need to be further explored.

5.5 Different icing time conditions

When the cloud layer containing supercooled water droplets covers a large area, the time it takes for the aircraft to pass through the cloud layer is also longer, and the time for ice accretion on the airfoil is also longer. Therefore, the icing situation on the airfoils and the corresponding effects on aerodynamic characteristics under different icing time conditions also need to be studied. The selected test conditions are the same as those used in Chapter 3, and the icing time is increased to 10 minutes.

Within 10 minutes of icing, the changes of ice shapes of different airfoils with time are as follows:

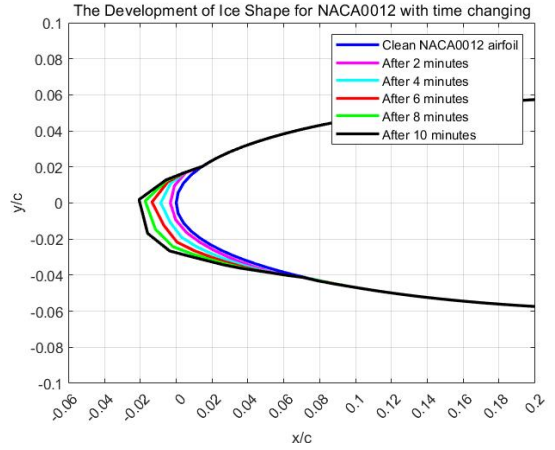

Figure 5.37 Ice shapes of NACA0012 with different time

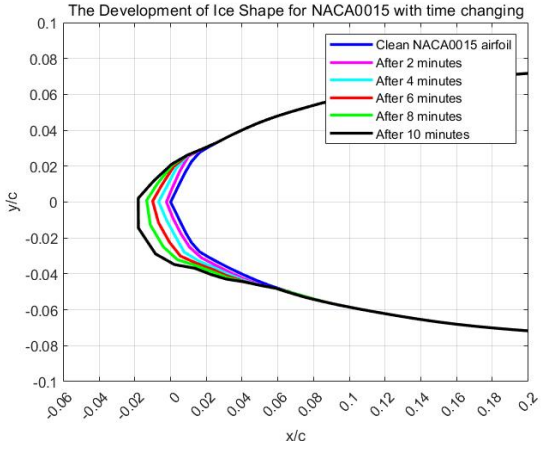

Figure 5.38 Ice shapes of NACA0015 with different time

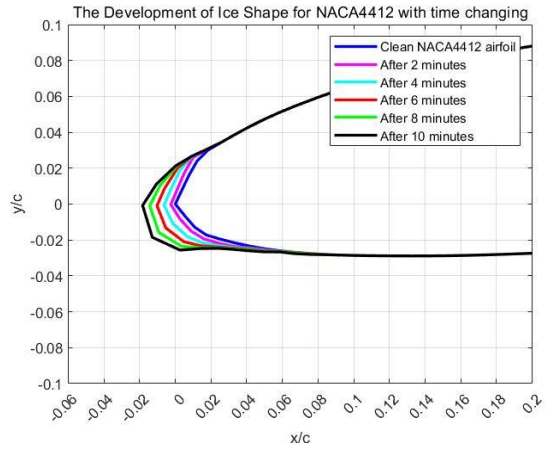

Figure 5.39 Ice shapes of NACA4412 with different time

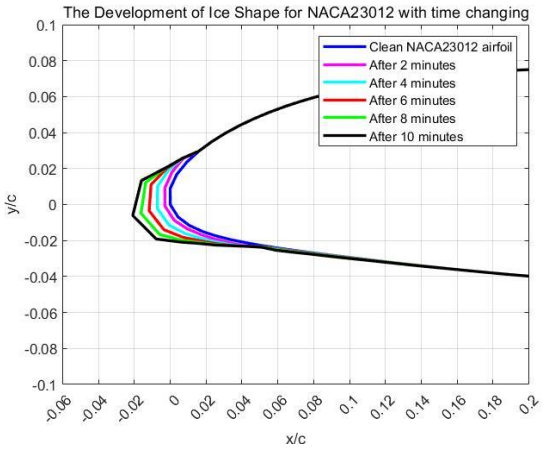

Figure 5.40 Ice shapes of NACA23012 with different time

With the extension of the ice accretion time, the amount of ice accretion on the airfoil gradually increased, from the original ice accretion with a maximum thickness of about 2 mm at 2 minutes to an ice accretion with a maximum thickness of about 2 cm at 10 minutes. Therefore, the design of the anti-icing system should consider the time interval of periodic

deicing and the timing of deicing, otherwise it is easy to produce thick ice; pilots also need to clearly understand the damage caused by icing before starting the deicing operation, and fully realize that deicing is urgent.

Taking NACA0012 and NACA23012 as examples to illustrate the changes of the aerodynamic coefficients at different icing times:

Table 5.16 Variation of lift and drag coefficients of NACA0012 under different icing time conditions

Icing time t (minutes)	C_L	Loss percentage of C_L(%)	C_D	Growth percentage of C_D(%)
0	0.41493	0%	0.010058	0%
4	0.35964	13.33%	0.012676	26.03%
6	0.34680	16.42%	0.014234	41.52%
8	0.31824	23.30%	0.016369	62.75%
10	0.26878	35.22%	0.019328	92.17%

Table 5.17 Variation of lift and drag coefficients of NACA23012 under different icing time conditions

Icing time t (minutes)	C_L	Loss percentage of C_L(%)	C_D	Growth percentage of C_D(%)
0	0.54374	0%	0.010184	0%
4	0.48608	10.60%	0.012847	26.15%
6	0.45796	15.78%	0.015054	47.82%
8	0.40390	25.72%	0.018296	79.65%
10	0.34630	36.31%	0.021706	113.14%

When the icing time reaches 10 minutes, the lift coefficients of both airfoils lose more than 35%, and the drag coefficients increase by about 1 times.

5.6 Different Flight Speed Conditions

This study selects four flight speeds, namely: $45m/s$, $65m/s$, $85m/s$ and $105m/s$. The specific icing conditions are as follows:

Table 5.18 Different flight speed conditions

Icing conditions	Test cases 49-52	Test cases 53-56	Test cases 57-60	Test cases 61-64
Selected airfoils	Four airfoils	Four airfoils	Four airfoils	Four airfoils
Chord length c(m)	1	1	1	1
Flight speed U_∞(m/s)	45	65	85	105

Angle of attack $\alpha(^\circ)$	4	4	4	4
Free flow pressure p_∞(Pa)	101325	101325	101325	101325
Free flow temperature $T_\infty(K)$	258.15	258.15	258.15	258.15
Liquid water concentration LWC(g/m^3)	1.0	1.0	1.0	1.0
Median volume diameter MVD(μm)	25	25	25	25
Total icing time t(min)	6	6	6	6
Single icing step Δt(min)	2	2	2	2

The local collection efficiency distributions of supercooled water droplets under different flight speeds are shown in the following figures:

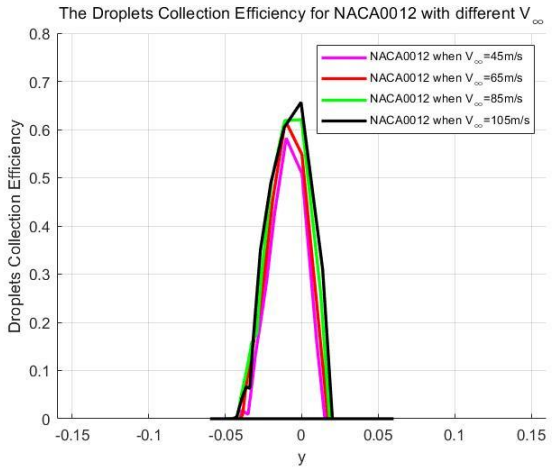

Figure 5.41 Collection efficiency of NACA0012 with different speeds

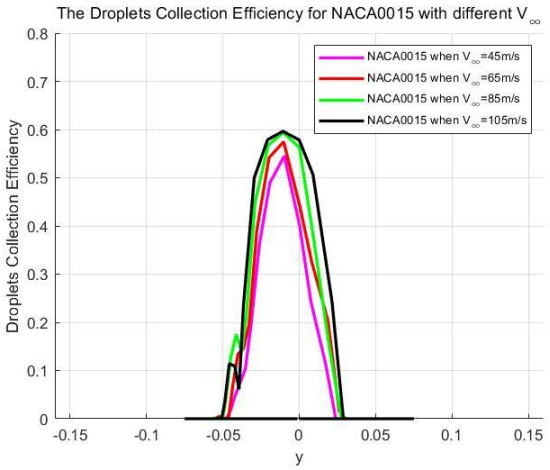

Figure 5.42 Collection efficiency of NACA0015 with different speeds

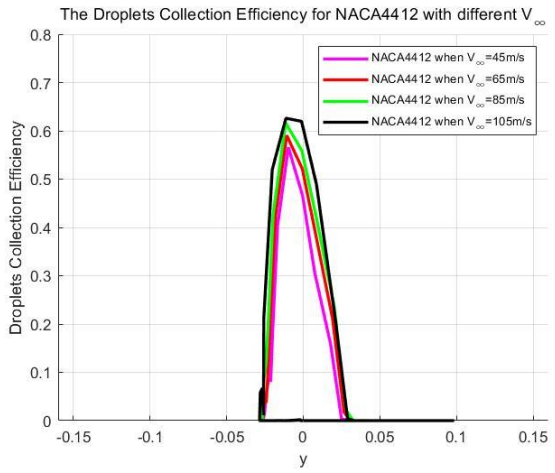

Figure 5.43 Collection efficiency of NACA4412 with different speeds

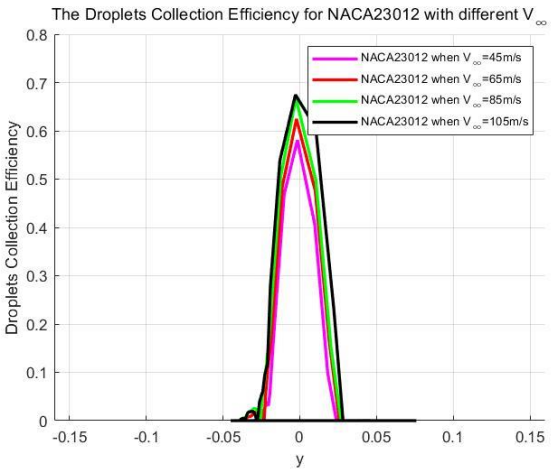

Figure 5.44 Collection efficiency of NACA23012 with different speeds

When the flight speed is fast, the impact range of the water droplets on the airfoil is relatively wider, indicating that the faster droplets of the same mass have greater momentum, and it takes longer to change the trajectories, and some droplets may not have enough time to bypass the airfoil. The ice shapes of the four airfoils after 6 minutes of icing under different flight speeds are shown in the following figures:

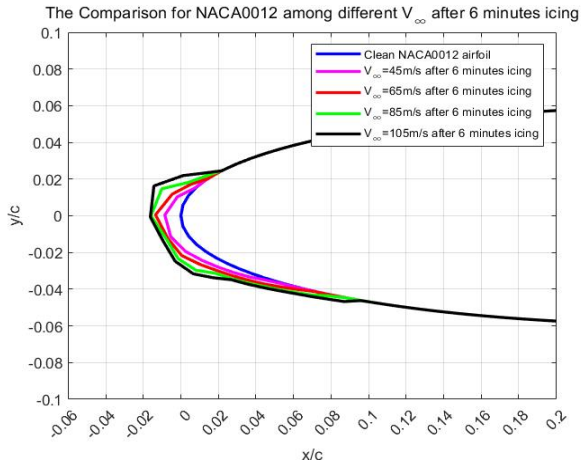

Figure 5.45 Ice shapes of NACA0012 with different speeds

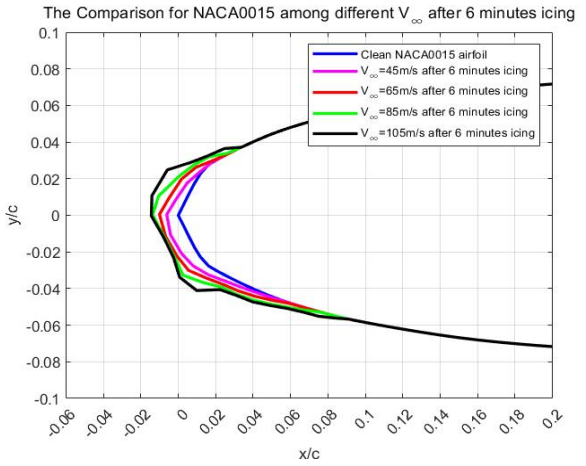

Figure 5.46 Ice shapes of NACA0015 with different speeds

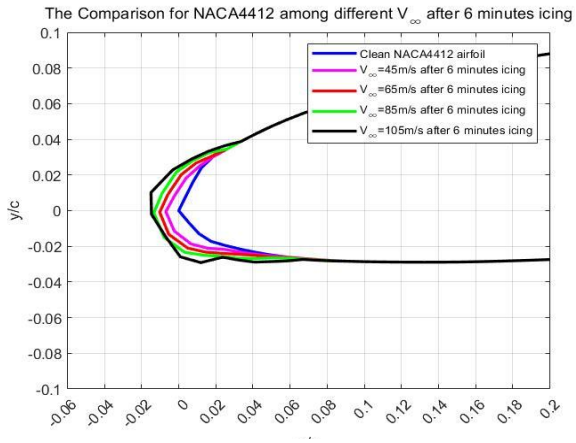

Figure 5.47 Ice shapes of NACA4412 with different speeds

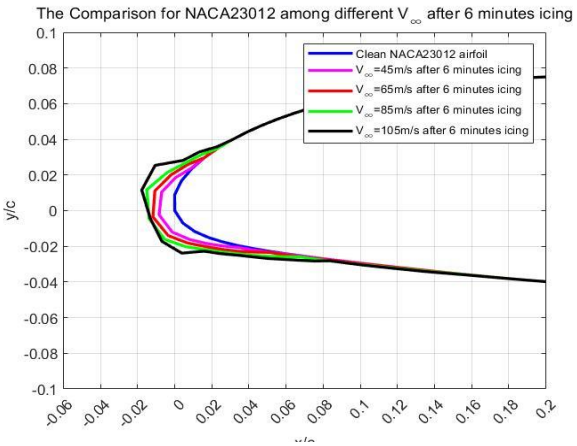

Figure 5.48 Ice shapes of NACA23012 with different speeds

When the flight speed gradually increases, the amount of ice accretion on the airfoil gradually increases, and the ice accretion range on the upper and lower airfoil surfaces expands. The reason is that the incoming flow speed will affect the shear force and the pressure gradient of the air on the water film layer, thereby affecting the flow of the water film. When the incoming flow velocity is high, the force driving the water film to flow is large, so that part of the unfrozen liquid water continues to flow until it is completely frozen at a position far from the stagnation point. In addition, the mass of ice accretion per unit time is proportional to the incoming flow velocity, so under the same icing time, the faster the incoming flow velocity, the thicker the ice on the surface. In general, as the flight speed increases, the ice shape tends to be clear ice, with apparent ice "horn" appearing on the upper surface.

The surface pressure coefficients under different flight speeds are as follows:

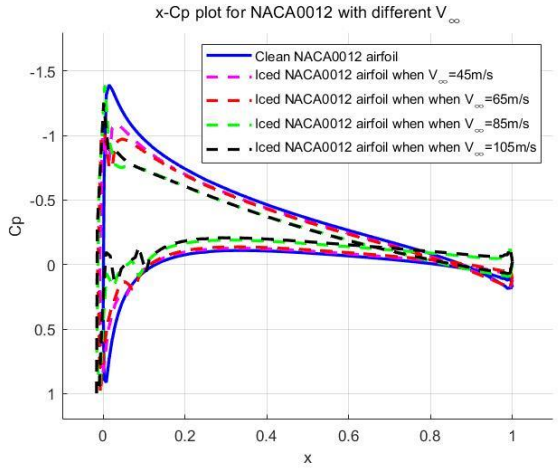

Figure 5.49 $x-Cp$ diagrams of NACA0012 with different speeds

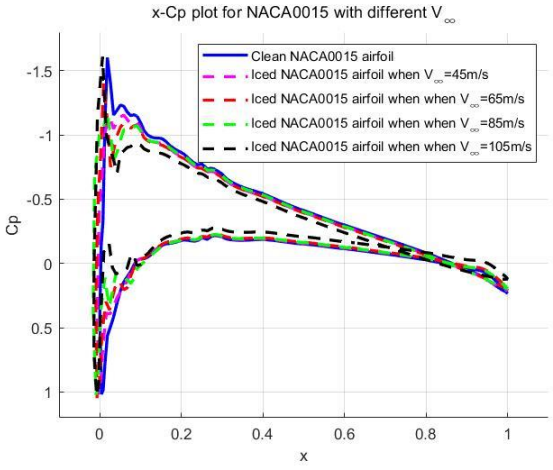

Figure 5.50 $x-Cp$ diagrams of NACA0015 with different speeds

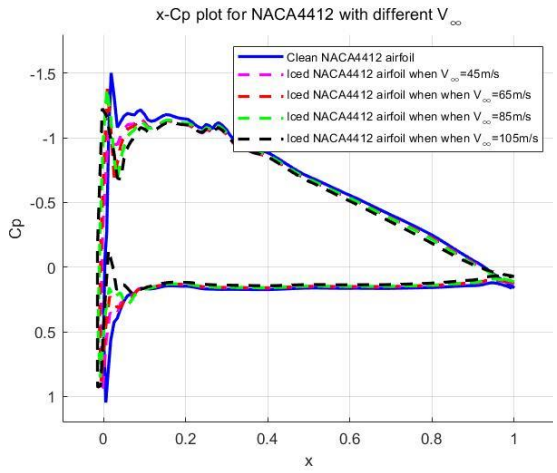

Figure 5.51 $x-Cp$ diagrams of NACA4412 with different speeds

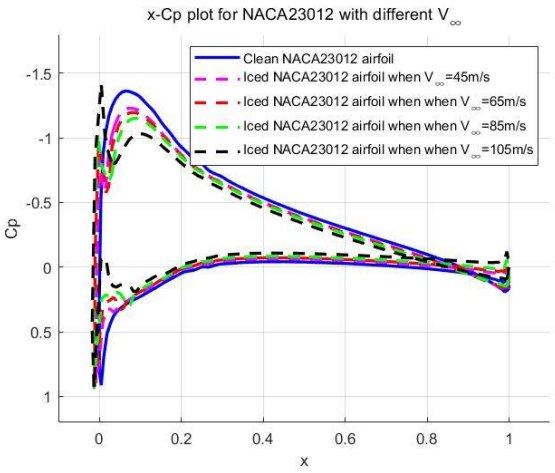

Figure 5.52 $x-Cp$ diagrams of NACA23012 with different speeds

The faster flight speed leads to the thickening of the ice layer and the irregularity of the ice shape, which further affects the change of the pressure coefficient Cp. When the incoming flow velocity $U_\infty = 105m/s$, there are large differences in the pressure coefficients distributions between the icing airfoils and the clean airfoils, and the changes of pressure near the leading edges of the airfoils are more severe, which is not conducive to flow stability. In addition, it should be noted that, for convenience of drawing, the pressure coefficients curves of the clean airfoils used here for comparison is drawn under the speed of $U_\infty = 65m/s$; and when the flight speed or flight Mach number changes, the pressure coefficient actually changes accordingly:

$$C_p = \frac{C_{p0}}{\sqrt{1 - Ma_\infty^2}} \tag{5.1}$$

C_{p0} corresponds to the pressure coefficient of $Ma_\infty \sim 0$. Therefore, as the flight speed increases, the differences between the actual pressure coefficients of the clean airfoils and the icing airfoils become more pronounced.

The following tables show the changes of the lift and drag coefficients of the four airfoils under different flight speeds:

Table 5.19 Variation of lift and drag coefficients of NACA0012 under different flight speeds

Flight speed $U_\infty\,(m/s)$	Initial C_L	After icing C_{L_ice}	Loss percentage of C_L(%)	Initial C_D	After icing C_{D_ice}	Growth percentage of C_D(%)
45	0.40840	0.36292	11.14%	0.010528	0.012643	20.09%
65	0.41493	0.34680	16.42%	0.010058	0.014234	41.52%

85	0.42269	0.23460	44.50%	0.009774	0.024882	154.57%
105	0.43231	0.22099	48.88%	0.009600	0.032370	237.19%

Table 5.20 Variation of lift and drag coefficients of NACA0015 under different flight speeds

Flight speed $U_\infty(m/s)$	Initial C_L	After icing C_{L_ice}	Loss percentage of C_L(%)	Initial C_D	After icing C_{D_ice}	Growth percentage of C_D(%)
45	0.39753	0.37864	4.75%	0.012265	0.012591	2.66%
65	0.40407	0.36896	8.69%	0.011756	0.014754	25.50%
85	0.40993	0.38390	6.35%	0.011463	0.014865	29.68%
105	0.41853	0.28335	32.30%	0.011291	0.021604	91.34%

Table 5.21 Variation of lift and drag coefficients of NACA4412 under different flight speeds

Flight speed $U_\infty(m/s)$	Initial C_L	After icing C_{L_ice}	Loss percentage of C_L(%)	Initial C_D	After icing C_{D_ice}	Growth percentage of C_D(%)
45	0.83103	0.80166	3.53%	0.013350	0.013523	1.30%
65	0.84481	0.80174	5.10%	0.013050	0.013987	7.18%
85	0.86063	0.80322	6.67%	0.012753	0.015027	17.83%
105	0.87985	0.76929	12.57%	0.012592	0.019599	55.65%

Table 5.22 Variation of lift and drag coefficients of NACA23012 under different flight speeds

Flight speed $U_\infty(m/s)$	Initial C_L	After icing C_{L_ice}	Loss percentage of C_L(%)	Initial C_D	After icing C_{D_ice}	Growth percentage of C_D(%)
45	0.53439	0.47379	11.34%	0.010689	0.013660	27.79%
65	0.54374	0.45796	15.78%	0.010184	0.015054	47.82%
85	0.55460	0.43917	20.81%	0.009882	0.017289	74.95%
105	0.56787	0.38217	32.70%	0.009714	0.024250	149.64%

When the flight speed $U_\infty = 45m/s$, the lift loss of the four airfoils does not exceed 15%, and the drag increase does not exceed 30%; with the increase of the flight speed, the aerodynamic characteristics deteriorate more and more seriously, when $U_\infty = 105m/s$, the lift loss of the NACA0012 airfoil is close to 50%, and the drag increases by nearly 2.5 times; the lift and drag coefficients of other airfoils also change significantly, so when the flight speed increases, it is necessary to make anti-icing preparations, so as to avoid the occurrence of thick ice accretion. The cruising speed of some large civil aircraft is about 200m/s, when flying in the clouds with supercooled water droplets, it is more likely to freeze to form thick clear ice. Therefore, an anti-icing system for the wings must be designed for large civil aircraft to

prevent stalling.

5.7 Different Angle of Attack Conditions

The flight angle of attack starts from -2°, and the angle of attack data is selected every 2°, namely: -2°, 0°, 2°, 4°, 6°, 8°. Other parameters are the same as the calculation conditions in Chapter 3.

First, the surface pressure coefficients distributions of the clean airfoils under the conditions of -2° and 0° angle of attack are shown:

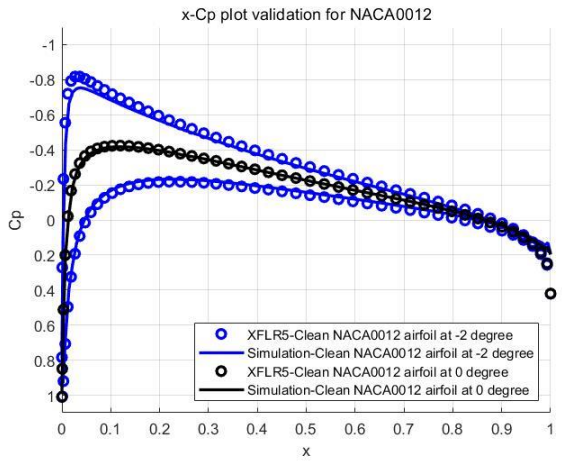

Figure 5.53 $x-Cp$ Verifications for NACA0012 Clean Airfoil

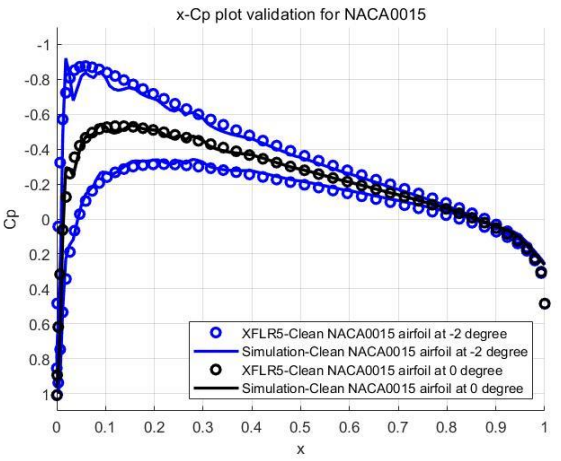

Figure 5.54 $x-Cp$ Verifications for NACA0015 Clean Airfoil

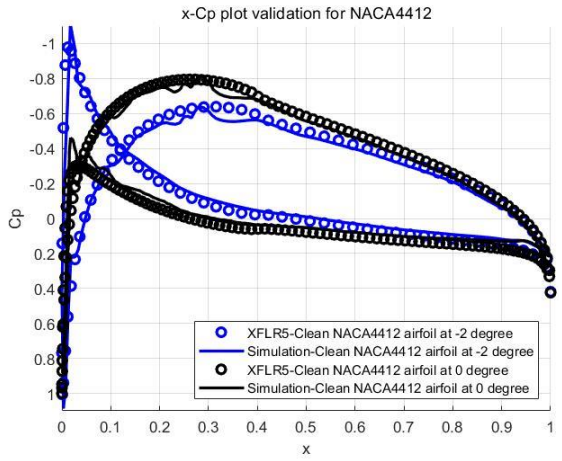

Figure 5.55 $x-Cp$ Verifications for NACA4412 Clean Airfoil

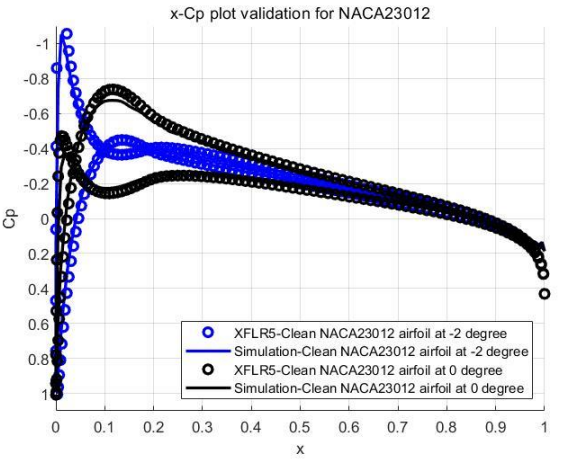

Figure 5.56 $x-Cp$ Verifications for NACA23012 Clean Airfoil

The blue data points in the figures represent the reference pressure coefficients of the airfoils at -2° angle of attack obtained by XFLR5 software, and the blue solid lines represent the pressure coefficients at -2° angle of attack calculated by this numerical simulation; The

black data points represent the reference pressure coefficients at 0° angle of attack obtained by XFLR5 software, and the black solid lines represent the lift coefficients at 0° angle of attack obtained by numerical simulation. It can be seen from the figures that the numerical simulation results of the four clean airfoils are in good agreement with the reference data points, which further indicates that the mesh divisions for calculations and the Fluent settings are correct; combined with the previous verifications of ice shapes, it can be concluded that the data calculated in this study are reliable and valid.

The local droplet collection efficiency distributions of different airfoils under different flight angles of attack are as follows:

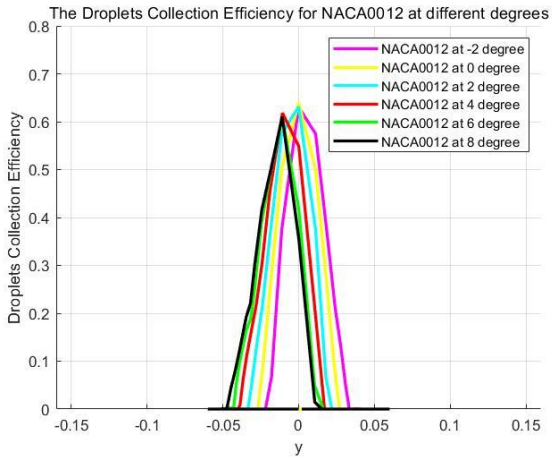

Figure 5.57 Collection efficiency of NACA0012 with different angles of attack

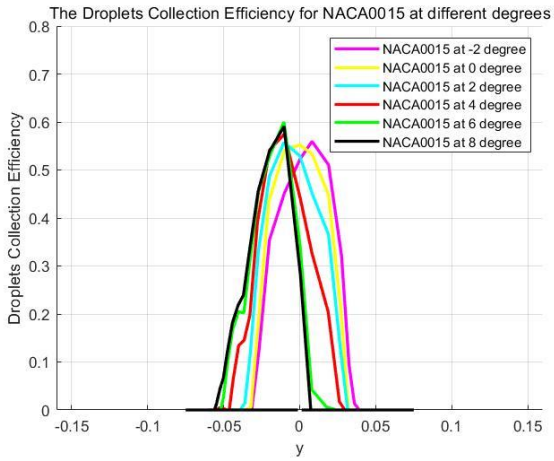

Figure 5.58 Collection efficiency of NACA0015 with different angles of attack

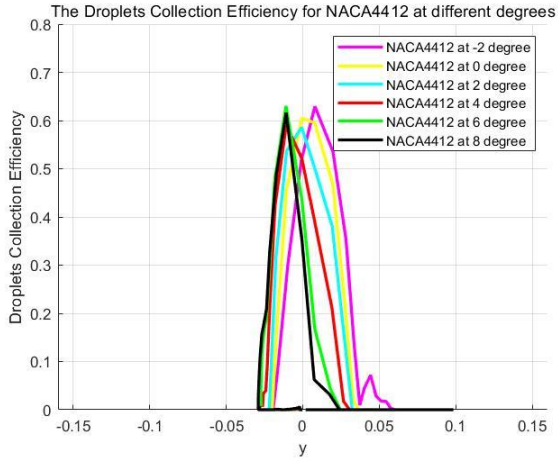

Figure 5.59 Collection efficiency of NACA4412 with different angles of attack

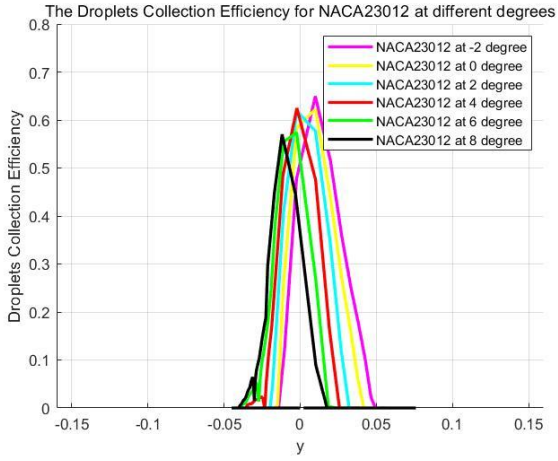

Figure 5.60 Collection efficiency of NACA23012 with different angles of attack

From the perspective of the distributions of collection efficiency, the common trend of the four airfoils is that as the flight angle of attack gradually increases, the distribution

positions of droplets on the airfoils gradually deviate toward the lower airfoil surfaces. When the flight angle of attack is equal to -2°, many water droplets collide with the upper surfaces, as shown by the purple lines in the figures; but when the flight angle of attack is equal to 8°, most of the droplets are intercepted by the lower surfaces, while the upper wing surfaces capture only a small amount of droplets, as shown by the black lines in the figures. In addition, the collection efficiency distributions of different airfoils at the same angle of attack are also different: the upper impact limits of the two airfoils NACA4412 and NACA23012 are larger, and the collection efficiency distributions deviate to the right as a whole, indicating that under the same conditions, the upper surfaces of these two airfoils intercept relatively more water droplets, which is caused by the camber of the airfoils.

The ice shapes at different angles of attack are shown in the figures below:

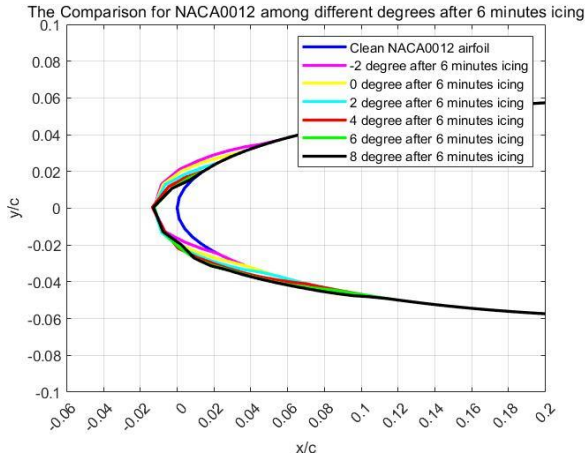

Figure 5.61 Ice shapes of NACA0012 with different angles of attack

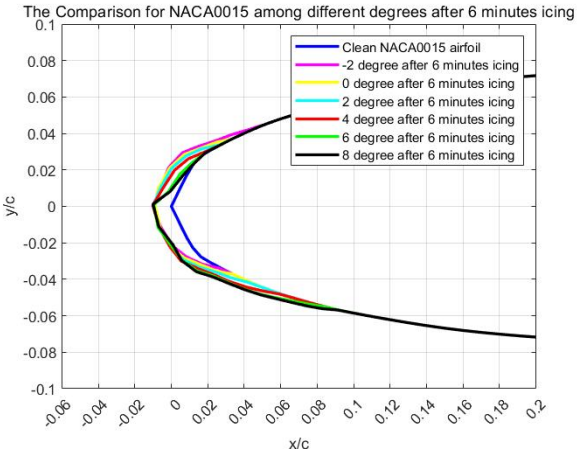

Figure 5.62 Ice shapes of NACA0015 with different angles of attack

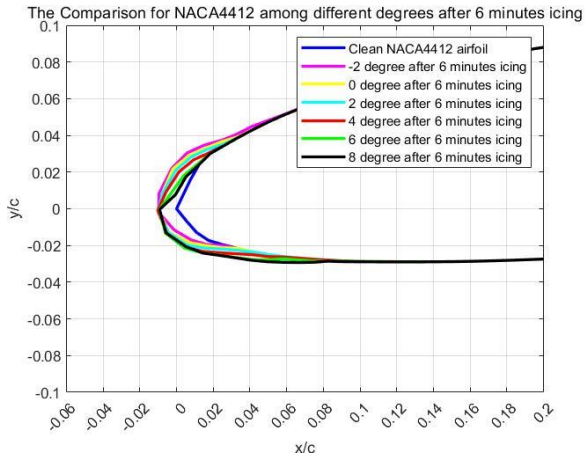

Figure 5.63 Ice shapes of NACA4412 with different angles of attack

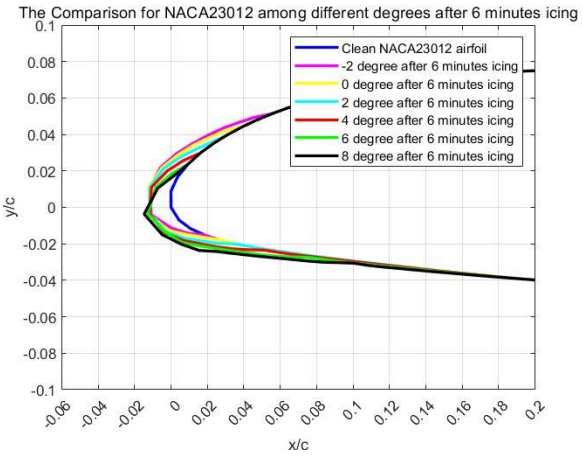

Figure 5.64 Ice shapes of NACA23012 with different angles of attack

It can be seen from the figures that when the angle of attack is -2°, compared with the lower surfaces of the airfoils, the upper surfaces have more ice accretion and thicker ice layers; when the angle of attack increases, the icing coverage moves towards the lower surfaces, and when the angle of attack is 8°, airfoil icing mainly occurs on the lower surfaces. Taking NACA0012 as an example to illustrate the pressure coefficients of icing airfoils at different angles of attack:

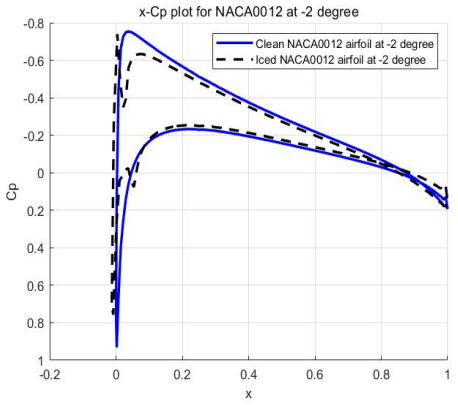

Figure 5.65 $x-Cp$ diagrams of NACA0012 at $-2°$

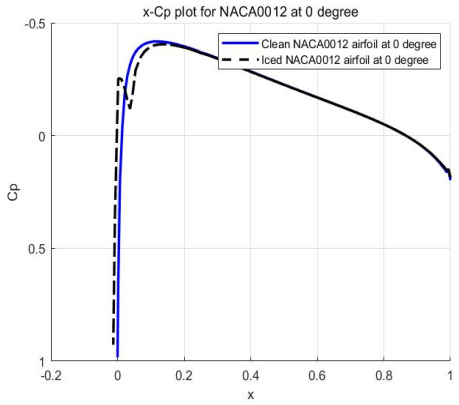

Figure 5.66 $x-Cp$ diagrams of NACA0012 at $0°$

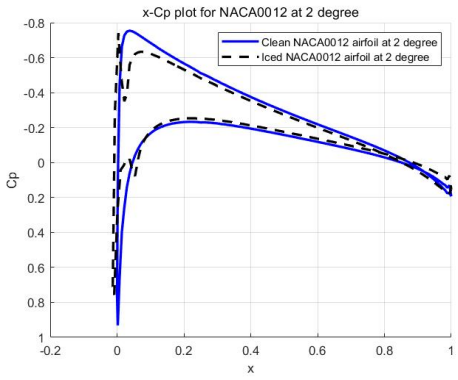

Figure 5.67 $x-Cp$ diagrams of NACA0012 at $2°$

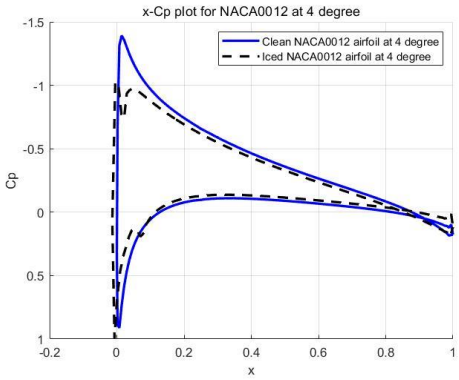

Figure 5.68 $x-Cp$ diagrams of NACA0012 at $4°$

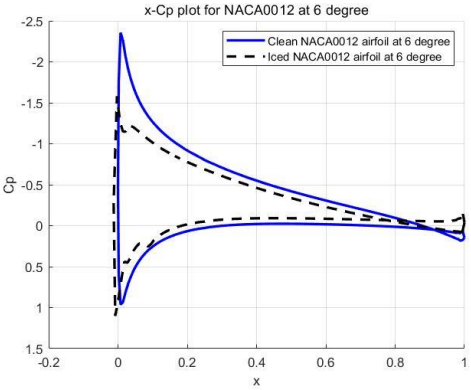

Figure 5.69 $x-Cp$ diagrams of NACA0012 at $6°$

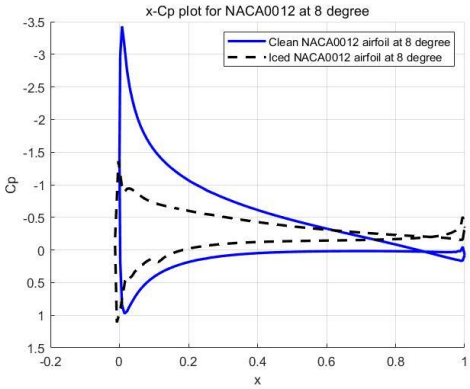

Figure 5.70 $x-Cp$ diagrams of NACA0012 at $8°$

When the flight angle of attack is relatively small, the effect of icing on the surface pressure coefficients of the NACA0012 airfoil is small; but if the flight angle of attack is increased to 8°, the change of the surface pressure coefficients is quite obvious compared to the clean airfoil, the negative pressure coefficient peak of the airfoil is greatly reduced, indicating that the icing upper surface near the leading edge can no longer provide a large enough suction area; in addition, the back part of the curve is relatively flat, Cp maintains a certain value, and the flow separation has already appeared. For the other three airfoils, the changes of the surface pressure coefficients under the condition of 8° angle of attack are also significant.

The changes of the lift and drag coefficients of the four airfoils with the angles of attack are shown below:

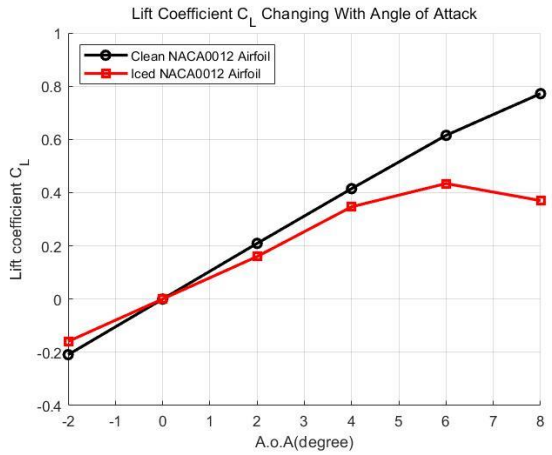

Figure 5.71 $\alpha - C_L$ curve of NACA0012

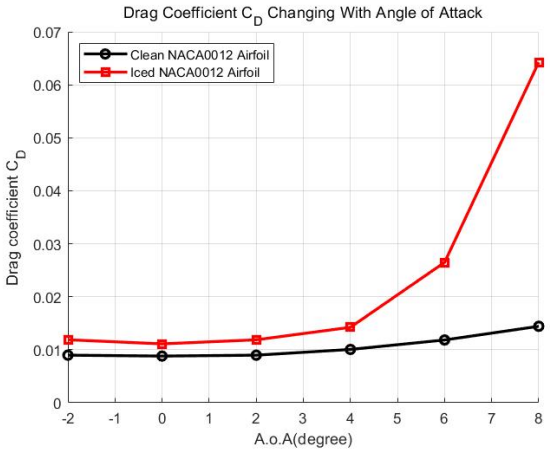

Figure 5.72 $\alpha - C_D$ curve of NACA0012

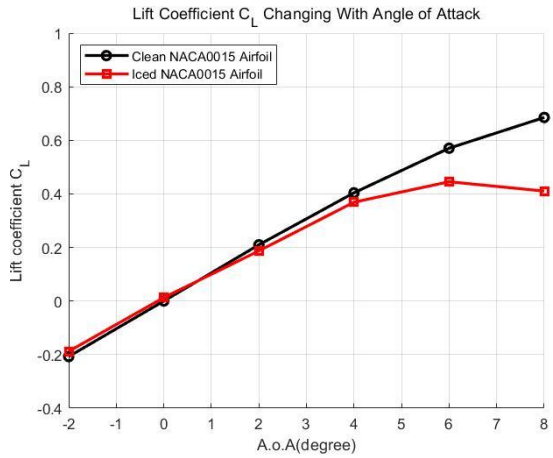

Figure 5.73 $\alpha - C_L$ curve of NACA0015

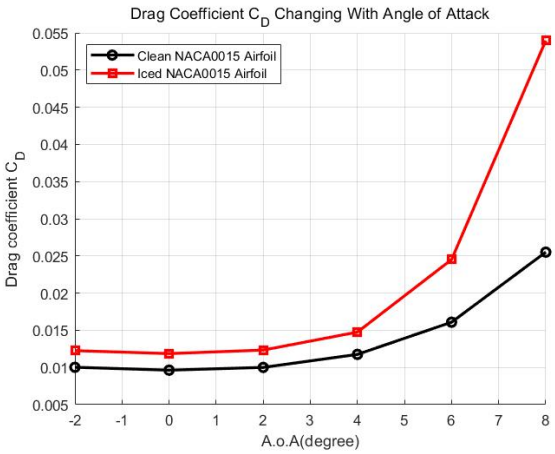

Figure 5.74 $\alpha - C_D$ curve of NACA0015

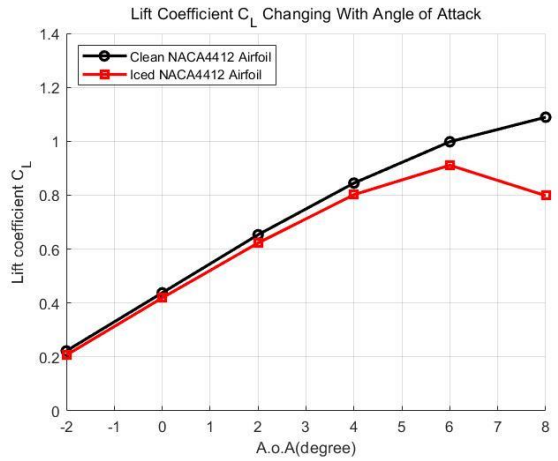

Figure 5.75 $\alpha - C_L$ curve of NACA4412

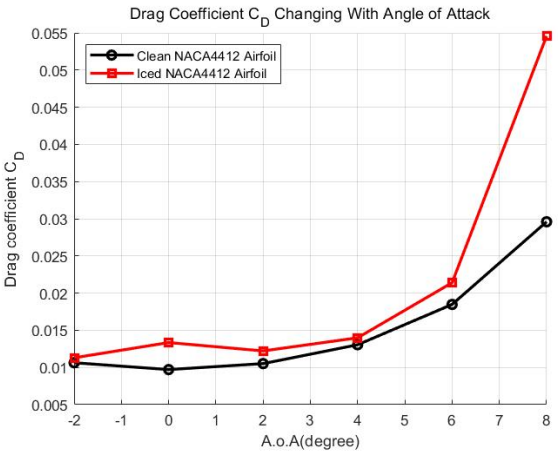

Figure 5.76 $\alpha - C_D$ curve of NACA4412

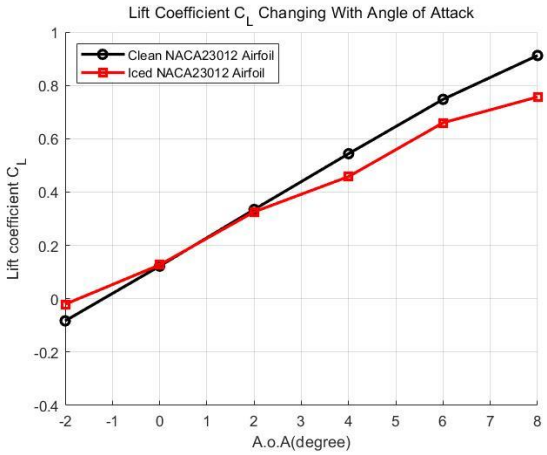

Figure 5.77 $\alpha - C_L$ curve of NACA23012

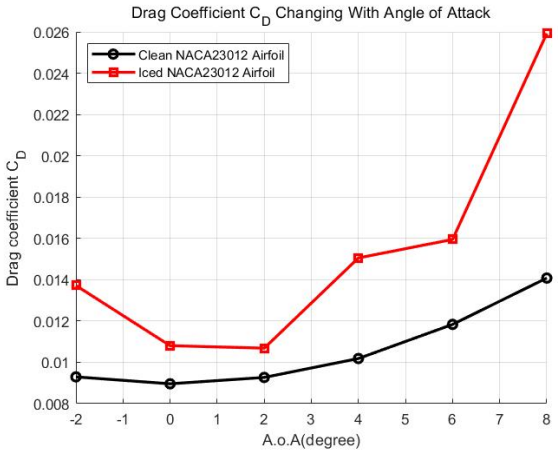

Figure 5.78 $\alpha - C_D$ curve of NACA23012

From the variation of lift and drag coefficients with angles of attack, it can be seen that under the condition of 8° angle of attack, the four airfoils all show serious aerodynamic deterioration, among which NACA0012, NACA0015 and NACA4412 airfoils have already stalled; the drag coefficients also show explosive increase, therefore, it is necessary to be extra vigilant about the airfoil icing behavior under high angle of attack condition. When the flight angle of attack is relatively small, the deterioration of the aerodynamic coefficients is not obvious.

Finally, taking the NACA0012 airfoil under the condition of 8° flight angle of attack as an example, the flow around icing airfoil is enlarged and displayed by the velocity vectors diagram and the trace plot:

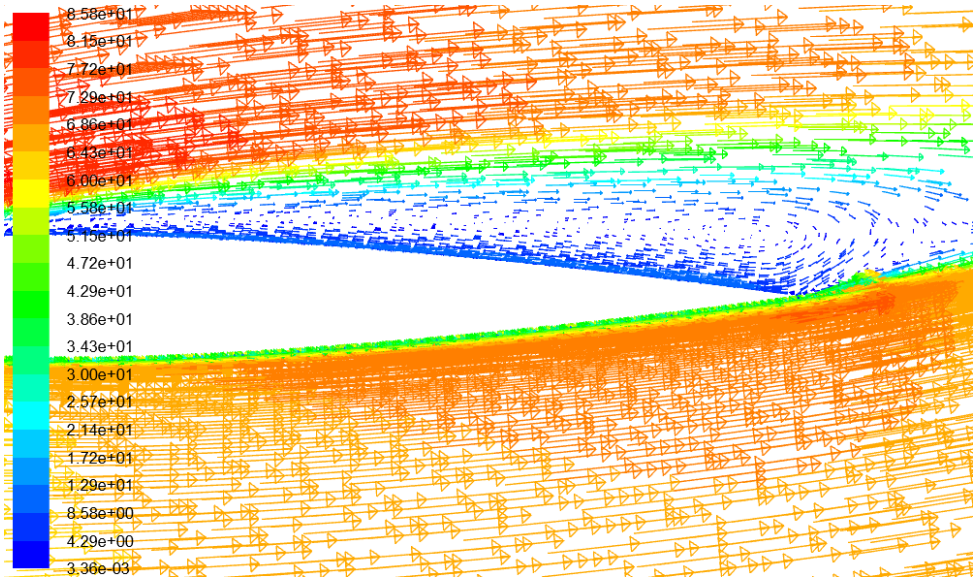

Figure 5.79 Recirculation zone of icing NACA0012 airfoil at 8° angle of attack(Velocity vectors)

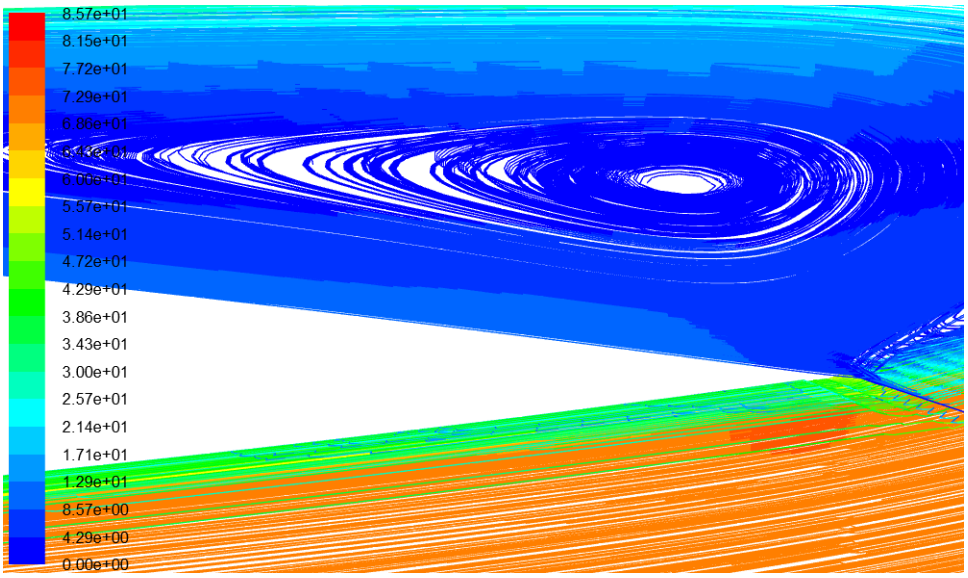

Figure 5.80 Recirculation zone of icing NACA0012 airfoil at 8° angle of attack(Trace plot)

The above figures clearly show that after ice accretion on the NACA0012 airfoil, flow separation has already occurred at the angle of attack of 8°, and a large low-speed recirculation zone has appeared on the upper surface of the icing airfoil, resulting in a large loss of lift and a substantial increase of drag.

5.8 Chapter Summary

This chapter used the numerical simulation platform to design and complete airfoil icing tests under different parameters, and the aerodynamic characteristics of NACA0012, NACA0015, NACA4412 and NACA23012 before and after icing were quantitatively compared to judge the

influence of icing.

The free flow temperature mainly affects the extent and type of ice accretion on the airfoil. The higher free flow temperature prevents the water film from being completely frozen at the impinging point, therefore, it is easy to produce clear ice with ice “horns”, and the aerodynamic characteristics of the airfoils can be greatly damaged; when the temperature of the free flow is relatively low, rime ice with a better streamlined shape can be formed.

The cloud liquid water concentration will not affect the local water droplet collection efficiency, but it is directly related to the mass of the impacting water droplets per unit time. Therefore, the higher the liquid water concentration, the greater the amount of ice accretion in the same time, and the thicker the ice layer. Higher liquid water concentration also causes part of the water to flow on the surface, resulting in irregular ice shapes that further deteriorate the lift and drag coefficients.

The median volume diameter of water droplets directly changes the collection efficiency of water droplets by affecting the impact range and the amount of droplets that can be intercepted at the impact location. Generally speaking, the larger the median volume diameter of water droplets is, the larger the impact range on the airfoil will be, the more water will be intercepted at a specific location, and the collection efficiency distribution will become wider and higher, which will further increase the thickness of ice accretion on the airfoils.

The wider the coverage of the clouds with supercooled water droplets, the longer the airfoil icing time. Long-term ice accretion gradually thickens the ice shape, so that the lift coefficient is gradually decreased and the drag coefficient is gradually increased.

The flight speed of the airfoils not only affects the droplet collection efficiency distribution, but also affects the flow of the water film on the airfoil and changes the size of the icing zone. The increase in flight speed is also prone to produce clear ice, and the aerodynamic characteristics can be severely damaged.

The change of the flight angle of attack makes the distribution range of droplets on the airfoils different. When the angle of attack is negative, the upper airfoil surface can collect more water droplets; when the angle of attack is 0°, the amount of droplets collected by the upper and lower surfaces is equivalent; as the angle of attack continues to increase, more and more droplets are collected on the lower surface. The difference in the distribution of water droplets also leads to the difference in the icing range on the airfoil. The negative flight angle of attack makes greater amount of ice accretion and thicker ice on the upper airfoil surface. As angle of attack increases, the icing zone moves towards lower surface, and finally at the angle of attack of 8°, ice accretion occurs mainly on the lower surface. From the curves of the lift and drag

coefficients against flight angle of attack, it can be seen that under the condition of high angle of attack, the lift loss and drag growth are quite obvious, and it is also accompanied by airfoil stall, which needs to be paid attention to.

In addition to studying the influence of airfoil icing on the aerodynamic characteristics under the above different parameters, the pressure coefficients of the clean airfoils at -2° and 0° were also verified. The simulation results were compared with the reference data points provided by the XFLR5 software, and they were in good agreement, which verified the accuracy of this study.

Chapter 6 Summary and prospect of study

6.1 Summary of Study

This paper mainly used the built ANSYS numerical simulation platform to study the airfoil icing problem under different parameters conditions, and obtained the expected results.

Firstly, starting from the icing phenomenon, the research background and the research progress of airfoil icing problem were introduced. On this basis, the specific research content of this paper was put forward, aiming to use numerical simulation method to study the influence of airfoil icing on aerodynamic characteristics under different conditions.

Then, according to the idea of solving the problem, the theoretical analysis of the flow field around the airfoil, the trajectory of water droplets and the icing behavior on the airfoil were carried out, and the corresponding mathematical models as well as discrete methods were constructed. The flow field around the airfoil was governed by the N-S equations system, and the solution domain and equations were discretized based on the finite volume method; in addition, the $SST\ k{-}\omega$ turbulence model was also considered. The trajectories of the water droplets were described by the Euler method, and the Galerkin finite element method was used to discretize the equations system, in addition to that the streamline upwind term was introduced to consider the directionality of convection. The airfoil icing analysis was based on the improved Messinger model, by establishing the mass and energy conservation equations of the water film, combined with the compatibility conditions, the icing behavior can be determined.

After completing the theoretical analysis and mathematical modeling, the ANSYS numerical simulation platform for airfoil icing was set up. Four NACA airfoils were selected as the research objects, the corresponding computational grids were generated, and the related technologies of grid updating were introduced. According to the technology route, the ANSYS platform was built. In order to ensure the correctness, the related simulations were completed according to the specific icing conditions given in the reference, and the calculation results were compared with the experimental data and the LEWICE numerical results.

Finally, according to the control variable method, a series of tests were carried out for different icing conditions. Through qualitative and quantitative analysis, the effects of the changes of the icing conditions on the local collection efficiency, ice shapes, pressure coefficients and the aerodynamic coefficients were revealed.

The conclusions of the study include the following:

1） The influence of different free flow temperature is mainly reflected in the changes of ice shapes. When the free flow temperature is low, the rime ice with better streamline shape is easy to form; however, when the temperature reaches −7°C, the clear ice appears. Due to the ice horn on the clear ice, the aerodynamic characteristics are greatly damaged. Taking the NACA0012 airfoil as an example, the lift reduced by 27.30% and the drag increased by 96.05% after 6 minutes of icing;

2） Although the cloud liquid water concentration does not affect the local collection efficiency, it will directly affect the rate and amount of ice accretion on the airfoils. High liquid water concentration will cause a thick ice layer on the airfoil, resulting in a sharp deterioration of the aerodynamic characteristics of the airfoil: under the condition of liquid water concentration of 2.0 g/m^3, NACA0012 airfoil had 45.96% lift loss and 186.92% drag growth; NACA0015 airfoil had 57.07% lift loss and 185.85% drag growth; NACA4412 airfoil had 27.94% lift loss and 122.32% drag growth; NACA23012 airfoil had 35.57% lift loss and 164.24% drag growth. Therefore, it is necessary to pay great attention to special meteorological conditions such as cumulonimbus during flight, and turn on the anti-icing system when necessary to avoid accidents;

3） The median volume diameter of water droplets directly affects the local collection efficiency and the icing extent on the airfoils. The larger the median volume diameter is, the higher the peak value and wider distribution of the collection efficiency, the more water impacting on the airfoil, and the larger the ice accumulation range. Taking the NACA0012 airfoil as an example, when the median volume diameter of water droplets is 40μm, after 6 minutes of icing, the lift reduced by 27.07% and the drag increased by 64.36%;

4） As the icing time progresses, the ice layer will gradually thicken. Therefore, when passing through large cloud area with supercooled water droplets, it is necessary to carry out deicing operations in time to avoid long-term icing and ensure the aerodynamic characteristics;

5） The flight speed affects both droplet collection efficiency and icing limits. When the speed is high, the water droplets will collide with the airfoil before they can avoid it, and the local collection efficiency is high; and the mass of icing per unit time on the upper and lower surfaces during high-speed flight will also increase, and the icing limits on the upper and lower surfaces will also widen, which will further aggravate the deterioration of lift and drag: the NACA0012 airfoil lost nearly 50% of its lift, and the drag increased by more than 2 times;

6） The flight angle of attack will change the icing zone on the airfoil surface. The increase of the angle of attack causes the droplets interception and icing zone to shift from the upper surface to the lower surface. In the case of icing, the aerodynamic loss can be small and

flight will be relatively safe if the airfoils maintain a small angle of attack; but when flying with a high angle of attack, the upper airfoil surface after icing is prone to flow separation, resulting in a substantial reduction in lift coefficient and a dramatic increase in drag coefficient: the lift coefficient of the NACA0012 icing airfoil at an angle of attack of 8° is reduced by about 50%; the drag coefficient is increased by about 345%.

6.2 Prospect of Study

At present, there are few studies in China to use ANSYS and FENSAP-ICE solvers to calculate the airfoil icing problem. Therefore, this paper attempts to establish a simulation platform in the ANSYS environment, and complete the tests based on a series of parameter conditions. Although this study has achieved certain research goals, there are still some deficiencies, and further studies are needed:

1） In this study, the motion state of the airfoil was stationary, but there are some cases in which the airfoil will keep moving, such as the rotation of the helicopter rotor. When the rotor blades are moving forward and backward, the geometric angle of attack, flapping angle, etc. will keep changing with the azimuth angle, therefore, it is necessary to consider the influence of the airfoil movements;

2） The assumptions of supercooled water droplets were relatively simple, and the equivalent diameter of water droplets was kept as a certain value, while in reality the equivalent diameters of water droplets in the actual cloud may have a certain distribution range, and the distribution of water droplet diameters can be considered to further improve the solution of the droplets phase flow field ;

3） The selection of supercooled water droplets focused on small water droplets. When the droplets are large, the collision with the airfoils may lead to more complex physical behaviors such as splashing, breaking, and deformation. Therefore, it is still necessary to further study the generation mechanism and mathematical models for these behaviors to more effectively deal with the icing problem of supercooled large water droplets;

4） The airfoil icing used the improved Messinger model, but the problem was still simplified, for example, the heat conduction within the ice layer and the water film layer and the corresponding temperature changes were not considered, and the difference caused by heat conduction to the icing behavior can be analyzed;

5） For the airfoil icing problem, the corresponding deicing system can be designed, and the improvement of aerodynamic characteristics after adding the deicing system can be further analyzed;

6） The selection of airfoils was relatively traditional, and the research still focused on the NACA series airfoils. Therefore, more new airfoils can be selected, and different geometrical

parameters can be used to study in depth the effects of different thicknesses, different cambers, and different chord lengths on airfoil icing problem.

References

[1] Jeck R K. A history and interpretation of aircraft icing intensity definitions and FAA rules for operating in icing conditions[R]. FEDERAL AVIATION ADMINISTRATION ATLANTIC CITY NJ AIRPORT AND AIRCRAFT SAFETY RESEARCH AND DEVELOPMENT, 2001.

[2] Oleskiw M M. A review of 65 years of aircraft in-flight icing research at NRC[J]. Canadian Aeronautics and Space Journal, 2001, 47(3): 259-268.

[3] Langmuir, I., Blodgett, K. B. A mathematical investigation of water droplet trajectories[J]. Army Air Forces Technical Report, No. 5418, 1946.

[4] Messinger, B. L. Equilibrium temperature of an unheated icing surface as a function of airspeed[J]. Aero Sci, 1953, 20(1): 29–42.

[5] Gent, R. W., Dart, N. P., and Cansdale, J. T. Aircraft icing[J]. Philosophical Transactions of the Royal Society A, Vol. 358, 2000: pp. 2873–2911.

[6] Donald Eick. Aircraft Icing Accidents Presentation, NTSB, Washington, DC. 2015.

[7] Lynch, F. T., Khodadoust, A. Effects of ice accretions on aircraft aerodynamics[J]. Progress in Aerospace Sciences, Vol. 37, No. 8, 2001: pp. 669–767.

[8] 余放.飞机防除冰系统技术多元化发展战略与路径[J].民用飞机设计与研究,2020(1):38-43.

[9] Ratvasky T, Van Zante J, Riley J. NASA/FAA tailplane icing program overview[C]. 37th Aerospace Sciences Meeting and Exhibit. 1999: 370.

[10] Deiler C. FLYING WITH ICE-AN OVERVIEW OF DLR RESEARCH IN FLIGHT MECHANICS WITH ICING INFLUENCE DURING THE LAST DECADE[J]. 2021.

[11] Bergrun, Norman R. A Method for Numerically Calculating the Area and Distribution of Water Impingement on the Leading Edge of an Airfoil in a Cloud[J]. NACA Technical Note, No. 1397, 1947.

[12] Mason, B. J. The physics of clouds[M]. Oxford: Oxford Monographs on Meteorology, 2nd edn, 1971: p. 594.

[13] ANSYS Fluent 15.0, Fluent User's Guide.

[14] Economon T.D., Palacios F., Copeland S.R., et al. SU2: An open-source suite for multiphysics simulation and design[J]. AIAA Journal, 54(3):828–846, December 2015.

[15] Hansman, R. J. Droplet size distribution effects on aircraft ice accretion[J]. AIAA paper,

Vol. 22, No. 6, 1985.

[16] Bourgault Y, Habashi W, Dompierre J, et al. An Eulerian approach to supercooled droplets impingement calculations. 35th Aerospace Sciences Meeting and Exhibit, 1997, p. 176.

[17] Kays, W. M., Crawford, M. E. Convective heat and mass transfer[M], New York: McGraw-Hill, 2nd edn, 1981.

[18] Myers, T. G. Extension to the Messinger model for aircraft icing[J]. AIAA Journal, 2001, 39(2): pp. 211-218.

[19] Myers, T.G., Charpin, J.P.F. A mathematical model for atmospheric ice accretion and water flow on a cold surface[J]. International Journal of Heat and Mass Transfer, Vol. 47, 2004: pp. 5483-5500.

[20] ANSYS FENSAP-ICE User Manual, R1. 2021.

[21] Habashi W G, Morency F, Beaugendre H. FENSAP-ICE: a comprehensive 3D Simulation Tool for In-flight Icing[C]. 7th International Congress of Fluid Dynamics and Propulsion, Sharm-El-Sheikh, Egypt. 2001: 1-7.

[22] Croce G, De Candido E, Habashi W G, et al. FENSAP-ICE: Analytical model for spatial and temporal evolution of in-flight icing roughness[J]. Journal of Aircraft, 2010, 47(4): 1283-1289.

[23] Gori G., Zocca M., Garabelli M., et al. PoliMIce: A simulation framework for three-dimensional ice accretion[J]. Applied Mathematics and Computation, 267:96–107, 2015.

[24] Gori Giulio, Parma Gianluca, Zocca Marta, et al. Local solution to the unsteady Stefan problem for in-flight ice accretion modeling[J]. Journal of Aircraft, Vol. 55, No.1, 2018: pp. 251-262.

[25] M. Morelli, T. Bellosta, A. Guardone. Lagrangian Particle Tracking in Sliding Mesh Applicable for Rotorcraft Icing Applications[C]. 45th European Rotorcraft Forum, Warsaw, Poland, 17-20 Sept. 2019.

[26] B.Y. Zhou, N.R. Gauger, M. Morelli, et al. Development of a Real-Time In-Flight Ice Detection System via Computational Aeroacoustics and Bayesian Neural Networks[C]. AIAA Scitech 2020 Forum, Orlando, FL, USA, 6-10 Jan. 2020.

[27] 裘燮纲, 韩凤华. 飞机防冰系统[M]. 北京:航空专业教材编审组, 1985.

[28] 韩凤华, 常士楠, 王长和, 王安良. 某型飞机天线罩防冰装置的性能验证[J]. 航空学报, Vol. 20, 1999: 20(S1): 88-90.

[29] 杨胜华, 林贵平, 申晓斌. 三维复杂表面水滴撞击特性计算[J]. 航空动力学报,

2010(02): 284-290.

[30] 杨胜华, 林贵平. 机翼结冰过程的数值模拟[J]. 航空动力学报, 2011, 26(2): 323-330.

[31] 李鑫, 白俊强, 王昆, 史亚云. 欧拉两相流法在翼型积冰中的应用[J]. 中国科学: 物理学 力学 天文学, 2014, 第 44 卷, 第 3 期: 258-266.

[32] 雷梦龙, 常士楠, 杨波. 基于 Myers 模型的三维结冰数值仿真[J]. 航空学报，2018, 39(9)：121952.

[33] 葛杨俊. 飞机结冰数值模拟中的网格重构及多物理场耦合方法研究[D]. 合肥:合肥工业大学, 2019.

[34] 王超, 常士楠, 杨波, 黎明中. 机翼防冰过程中冰脊问题的数值分析[J]. 北京航空航天大学学报, 2013, 39(06): 776-781.

[35] 胡琪, 黄安平, 孙涛等. 机翼防/除冰技术研究进展[J]. 科技导报, 2015, 33(07): 114-119.

[36] Cao Yihua, Tan Wenyuan, Wu, Zhenlong. Aircraft icing: An ongoing threat to aviation safety[J]. Aerospace Science and Technology. 2018, 75(10): 353-385.

[37] 易贤, 桂业伟, 朱国林. 飞机三维结冰模型及其数值求解方法[J]. 航空学报,2010,31(11):2152-2158.

[38] 郭龙, 刘森云, 易贤等. 水滴变形及其对阻力特性影响的实验研究[J]. 实验流体力学, 2020, 34(05): 44-49.

[39] 朱东宇. 翼型结冰过程的数值模拟[D]. 南京:南京航空航天大学, 2009.

[40] 王福军. 计算流体力学分析—CFD 软件原理与应用[M]. 北京: 清华大学出版社, 2004.

[41] 朱红钧, 林元华, 谢龙汉. Fluent 流体分析及仿真实用教程[M]. 北京:人民邮电出版社, 2010.

[42] 陈晓圆. 飞机结冰多参数影响研究[D]. 南京:南京航空航天大学, 2015.

[43] Beaugendre H., Morency F., Habashi W.G. FENSAP-ICE's Three-Dimensional In-Flight Ice Accretion Module: ICE3D. Journal of Aircraft, 2003, 40, 239-247.

[44] S. Fornasier, Ice accretion simulation over 2D airfoils by means of a methodology embedded in a CFD solver, M.Sc. thesis, Università degli Studi di Padova, 2015.

[45] Shin J, BOND T. Results of an icing test on a NACA 0012 airfoil in the NASA Lewis icing research tunnel[C]. 30th Aerospace Sciences Meeting and Exhibit. 1992: 647.

Acknowledgement

Time flies, four years have passed in the blink of an eye. I vaguely remember the green years when I came to Beihang University to check in, everything seemed like yesterday. Right now, I am still studying for the double master degree at the Politecnico di Milano, Italy. In the past four years, I have gained a lot, including not only professional knowledge and practice, but also personal character training, independent living ability training, and spiritual and willpower shaping. It has been more than three and a half years since I came to Italy from Beijing. There are many people and things that I miss in my heart. However, I have to continue to persevere because of the fetters of my studies. When studying abroad, people who go out know best what setbacks and tests they have experienced, and they also know how to grasp the moment and cherish the present. The hardships and bitterness are just the past, the important thing is to know what I want in my study journey, and never give up the ideal in my mind. Just like Luffy in "One Piece", he wants to across the ocean and find the legendary One Piece. Difficulties can always be overcome. In the anime, Luffy has the support and help of his partners, but in reality, I have the encouragement and assistance of my family, teachers, classmates, and friends. At the end of this paper, I would like to express my sincere thanks to them:

First of all, I am very grateful to my advisor at Politecnico di Milano: Professor Federico Piscaglia. He is academically rigorous and responsible, and he is also very kind, I always look forward to interviewing or emailing him. I can even remember every email related to the academic questions, Professor Federico Piscaglia always replied to them in time and helped me a lot. When I was stuck and frustrated with annoying problems, he always gave me guidance and encouragement, so that I can see hope for the future.

I also would like to show my appreciation to my advisor at Beihang University, Professor Akira Rinoshika. He is not only knowledgeable, but also very kind and approachable, always giving people a sense of peace of mind. I remember that during the summer vacation of 2018, I met Mr. Li for the first time at Northwestern Polytechnical University. Although I was a little nervous at the time, the communication between Mr. Li and me was pleasant and memorable; I also remember that when I post processed PIV measurements data of flow around cylinder, due to the short data processing time, I got an incorrect speed cloud map. Fortunately, Mr. Li pointed out my mistake in time, so that I could learn from experience and summarize the problem.

My parents have been with me during my postgraduate studies. In the previous time I still had time to visit and accompany them during the winter and summer vacations in China; but now I have to keep in touch with them through WeChat when I am abroad. They have always been my spiritual support and guide on the road of life, and they have also brought me up, the kindness of parenting is greater than God; they taught me a lot of knowledge and principles of life, and also made me understand the value of life, gratitude is rightful. When I return from my studies, I will spend more time with my parents and show my filial piety.

In addition, I would also like to thank the department leaders of Politecnico di Milano and Beihang University, as well as Ms. Li Shan, Ms. Shi Jingling, Mr. Du Benxin from the Academic Affairs Office. I would like to thank them for taking care of my application again and again. I also thank them for answering my questions and letting me have a clearer understanding of the degree application process; I also thank Mr. Lan Shilong, who is in charge of arranging the thesis-opening defense; Mr. Xu Yang, who is responsible for arranging the mid-term inspection; the teachers of the question-opening and defense team, and the teachers of the mid-term inspection team. Their help and comments are also something I need to thank.

My relatives and friends in China, my roommates from Beihang University, my classmates in the research group, and other teachers and classmates are also concerned about my progress in completing my studies. I would also like to say thank you to them. It is your company that allows me to recall so many happy times when I am studying abroad.

My colleague Ruggiero Signoriello worked with me for several months, he is smart and has enough experience with pyclaw and python, I learned a lot from him and I am very happy to know him through the Professor Federico Piscaglia and discuss many interesting academic issues together. I thank him for accompanying me before graduating from Politecnico di Milano.

At the same time, I am very grateful to my current roommates: Jiang Jixiang, Dong Tao and Xia Zehui. When I am in trouble, they can help me share my anxiety in time, so that I can focus on the problem at hand; whenever I see their bedroom light on late at night, I always feel relieved, since I am not alone in the dark thinking, but with them.

Finally, I would like to thank all the people who encouraged, supported and helped me. It is because of you that my life is so colorful.